Active and Semi-Active Bushing Design for Variable Displacement Engine

by

Siamak Arzanpour

A thesis
presented to the University of Waterloo
in fulfillment of the
thesis requirement for the degree of
Doctor of Philosophy
in
Mechanical Engineering

Waterloo, Ontario, Canada, 2006

I hereby declare that I am the sole author of this thesis. This is a true copy of the thesis, including any required final revisions, as accepted by my examiners.

I understand that my thesis may be made electronically available to the public.

Abstract

The Variable Displacement Engine (VDE) is a new generation of engines that are designed to decrease the fuel consumption at the cruise speed of a vehicle. The isolation of the VDE's new vibration pattern is beyond the capabilities of conventional mounts and bushings. Consequently, in this thesis, novel active and semi-active solutions are proposed to develop various semi-active and active hydraulic bushing proof-of-concept systems that may solve the isolation problem in a VDE system.

The dynamic stiffness response, which is the transfer function that relates the engine displacement to the transmitted force, is normally used as the key design criterion for engine mounts and bushings. In this thesis, a linear mathematical model of a conventional hydraulic bushing is purposed. The validity of the mathematical model is confirmed by an experimental analysis, and the various parameters in the dynamic stiffness equation are evaluated.

The experimental results indicate that the dynamic stiffness frequency response of the conventional hydraulic bushing has both soft and stiff regions. The soft region is limited to low frequencies. For the VDE isolation, the goal is to provide a soft bushing for a wider range of frequencies than a conventional bushing can accommodate. Addition of a short inertia track, similar to a decoupler used in conventional hydraulic engine mounts, may be used to extend the soft region of a conventional hydraulic bushing, and the experimental results validate it.

Since the short inertia track provides no additional damping, a supplementary Magnetorheological (MR) valve is also devised. The MR valve has the advantage to minimize the amount of MR fluid used, which significantly reduces the cost of the overall

system. The novel valve allows the damping coefficient of the bushing assembly to be controlled by varying the electrical current input to a solenoid coil. A mathematical model is derived for the MR bushing, and is validated experimentally.

In addition, an active bushing to solve the VDE isolation problem is purposed in this thesis. In this bushing, a magnetic actuator, composed of a permanent magnet and a solenoid coil, is included in the active bushing. This active chamber affects the dynamic stiffness response of the bushing by altering the bushing's internal pressure. The nonlinear equation of motion of the permanent magnet is linearized and is incorporated into the new mathematical model of the system. The new purposed model for the active bushing is in good agreement with the experimental results. This active chamber is also proved capable of producing complex dynamic stiffness frequency response.

The conclusion is that the proposals in this thesis can contribute to the isolation of the vibration pattern, imposed by the application of a VDE system.

Acknowledgements

I would like to sincerely express my gratitude to my supervisor Professor M.F. Golnaraghi for his support and guidance. He gave me the courage and self confidence to explore and experiment. His confidence on me was a great source of motivation during the years I worked with him.

I would like to thank General Motors and Cooper Standard Co. corporations for their contributions to this project. A great deal of this research is inspired and made possible through the teamwork of past and present students of Professor Golnaraghi, Arash Narimani, Yu Shen, Anthony Kim, Ken Ying Kun Peng , Brad Schubert, Shahab Hasanzadeh Ghafari, Nima Eslaminasab, Hamidreza Bolandhemat, Babak Ebrahimi, Neda Parnian and Orang Vahid. I should specially thank Brad Schubert who worked closely with me and taught me practical skils. Many thanks go to Robert Wagner and Andy Barber and Sandra Buss, the technical staff of the department, for their conscientious effort.

Over the years, I have benefited greatly from the support of my friends, Amir, Hamid and Leila Chinaei, Sara Behjat, Farshid Sheikhi, Meharan and Zarin Rad, Nahal Doroodian, Amin Kamalzadeh, Majid Bahrami, Ehsan Shameli, Peyman and Naghmeh Servati, Mohamad Ansari, Keyvan Nowruzi, Hamid and Minoo Bolandhemat, Maryam Azish, and specially my best friend who was always there for me Kiarash Narimani. Also I would like to appreciate Shahab and Bahar Ghafari and their families, who treated me as a family member. I never forget you and I hope someday I could return part of your favour.

Also, I would like to thank Professor Golnaraghi as a friend who never let me alone in the tough moments. He and his kind wife, Mitra, provided me such a pleasant atmosphere that I never felt a distance. I always used their advice in my life and I never forget their hospitality.

Last but not least I want to thank my family, Elnaz, Sahar, Soheil and specially my mom Zahra. If there is any honour in this degree it belongs to her. My Dad, I never forget you. Your blessings and your soul were always with me.

Table of Contents

List of Tables

List of Figures

Nomenclature

$a = \left\| \ddot{X} / Y \right\|$	acceleration with respect to base excitation amplitude [1/s]
A_i	inertia track cross-sectional area [m^2]
A_p	effective pumping area [m^2]
B_r	rubber linear damping [N-s/m]
c	linear damping coefficient [N-s/m]
$C = 1/C_1 + 1/C_2$	lumped compliance [N/mm^5]
C_1, C_2	lower and upper chamber compliance, respectively [mm^5/N]
c_{MR}	constant of magnitude 2-3 depending on the controllability
d_h	inertia track hydraulic diameter
D_i	inner diameter of the MR valve coil
D_o	outer diameter of the MR valve coil
e	eccentricity of unbalance mass [m]
$f_n = \omega_n / 2\pi$	natural frequency [Hz]
f_o	harmonic force excitation amplitude per unit mass [N/kg]
$F(t)$	engine dynamic loading [N]
F_T	transmitted force [N]
FT	transmitted force per unit mass [N/kg]
g	height of the MR valve fluid channel
H_f	field intensity [At/m]
I	MR valve input current [A]
$i = \sqrt{-1}$	imaginary unit
k	linear stiffness coefficient [N/m]
K_r	rubber linear stiffness [N/m]
l	total length of the of the MR valve fluid path in the flux (inertia track)
L	inertia track fluid inductance [$Pa\text{-}s^2/m^3$]
MR	magnetorheological
MRF	magnetorheological fluid
m	mass of engine [kg]
m_o	engine unbalance mass [kg]
P_1, P_2	upper and lower chamber pressures [Psi]
Q	inertia track flowrate
Q_{in}	flow from pumping chamber to the MR valve
Q_{out}	flow from MR valve to the compliance chamber
$r = \omega / \omega_n$	excitation frequency ratio
R	base excitation RMS absolute acceleration

R_f	hydraulic resistance to flow [Pa-s/m^3]
V_{in}	input voltage [V]
x	engine (mass) displacement [m]
X	displacement amplitude [m]
X_{st}	static displacement amplitude due to step loading [m]
y	chassis or base displacement [m]
Y	base harmonic displacement excitation amplitude [m]
$z = x - y$	mass-base relative displacement [m]
Z	relative displacement amplitude [m]
z^*	perturbation solution non-dimensional displacement
$\zeta = c/2\sqrt{km}$	linear damping ratio
Δp_μ	viscous fluid pressure drop
Δp_τ	pressure drop due to MRF yielding
η	base excitation RMS relative displacement
$\lambda = \lvert(X - Y)/Y \rvert$	relative displacement transmissibility
γ	harmonic force excitation RMS displacement [(m-kg/N)^2]
ϕ	harmonic force excitation RMS force transmissibility
μ_f	MRF viscosity [Pa-s]
μ_{MR}	magnetic permeability of the MRF [H/m]
ω	frequency of oscillation [rad/s]
ω_{dr}	forcing input frequency of oscillation [rad/s]
$\omega_n = \sqrt{k/m}$	natural frequency [rad/s]
ρ_f	MRF density
τ_y	MRF yield stress as a function of the field intensity
$\Phi = \lvert F_T/F \rvert$	harmonic force excitation force transmissibility
$\Lambda = \lvert X/f_o \rvert$	harmonic force excitation displacement with respect to input force [m-kg/N]
$\psi = \lvert F_T/m_o e\omega_n^2 \rvert$	unbalance excitation non-dimensional force transmitted
$\Omega = \lvert Xm/m_o e \rvert$	unbalance excitation non-dimensional displacement
χ	unbalance excitation RMS non-dimensional force transmitted
Γ	unbalance excitation RMS non-dimensional displacement
φ	magnetic flux [Wb]

Chapter 1: Introduction

One of the characteristics that define the quality of a vehicle is the amount of noise-vibration-harshness (NVH) in the cabin. An automobile's engine, body, and chassis system are susceptible to undesirable vibrations, due to two sources of excitation: the inherent unbalance of the reciprocating engine, and the disturbances transmitted through the suspension system from the road. Muller, Weltin, Law, Roberts, and Siebler (1994) have agreed that decreasing the mass of vehicles increases the probability that the energy sources will be easily transferred through the structure as the vibration amplitudes increase. Therefore, the increase in fuel economy and decrease in price of the automobile comes at a price: more NVH and less comfort.

The frequency of unbalanced engine disturbances is related to the engine speed, the number of cylinders, and the stroke number (Makhult, 1977; Geck and Patton, 1984). Typically, the frequency of these vibrations is in the range of 1-200 Hz (Oueini *et al.* 1999). Usually, at idle or low speeds the engine conveys high amplitude vibrations, whereas at high speeds, low vibrations amplitude occurs. The amplitude of the engine vibrations, in most vehicles, is less than 0.3 *mm* at high frequencies (50-200 *Hz*) and more than 0.3 *mm* at low frequencies (1-50 *Hz*) (Jazzar and Golnaraghi 2001). At the same time, the transmitted forces from the engine to the chassis are proportional to the square of the engine vibration frequency that increases with speed. Generally, it is desirable to restrain the relative motion of the engine to satisfy the mechanical constraints, although the criterion is to minimize the force transmitted to and from the

engine itself (Singh, Kim, Ravindra, 1992). Minimizing the transferred force reduces the impact of the dynamics of the engine for a base (chassis or body) excitation, improving the ride, and minimizing the potentially damaging inertia forces on the engine. Also, minimizing the transfer of unbalanced forces through the engine to the chassis reduces cabin noise, and thus, improves rider comfort. These two different situations pose a challenge for designers in selecting the mount parameters for the best isolation performance.

Engine mounts are vibration isolators which are used to minimize the effect of such disturbances. In the automotive industry, the two main functions of an ideal engine mount are to isolate the vibration caused by the disturbance force in an engine, and to prevent engine bounce from the vehicle frame excitation (Esmailzadeh, 1978; Clough and Walter, 1968). Crede (1951) has reappraised and reproduced all the studies on vibration isolation and engine mount optimization. Taking advantage of what he learned, he has devised viable techniques to protect machinery from shock and vibration. Vibration reduction entails the use of mounts which are as soft as possible. On the other hand, the displacement constraints on engine deflection, due to physical limitations, prevent the mount stiffness from being too soft. Thus, engine mount design presents a demanding optimization problem because of the conflicting criteria involved. Today, a handbook by Beranek and Ver (1992) is one of the most consulted references for engine vibration. The principal functions of an engine mount can be summarized as,

- Support the weight of the engine.
- Prevent fatigue failure of the engine and gearbox support points which can occur if they are rigidly attached to the chassis or body structure.
- Isolate the unbalanced engine disturbance force from the structure of the vehicle.

- Reduce the amplitude of the engine vibrations that are transmitted to the body structure.
- Reduce the noise amplification that occurs if engine vibrations are transferred directly to the body structure.
- Reduce human discomfort and fatigue by partially isolating the engine vibrations from the body by means of an elastic medium.
- Accommodate engine block misalignment and reduce the residual stresses imposed on the engine block and mounting brackets due to chassis or body frame distortion.
- Prevent road-wheel-shocks that impart excessive movement to the engine.
- Prevent large engine-to-body relative movement due to torque reaction force, particularly in low gear, which can cause excessive misalignment and strain on such components as exhaust pipes and silencer system.
- Restrict the engine movement in the fore and aft direction of the vehicle due to the inertia of the engine in opposition to the accelerating and braking forces.

Because of the two dynamic disturbances of internal combustion engines, that is, the firing pulse due to the combustion of the fuel in the cylinder, and the inertia force and torque caused by the rotating and reciprocating parts, the firing pulses cause disturbance torques that act on the engine block. The disturbance inertia force has two components: the first component is parallel, and the second is perpendicular to the crankshaft axis. The second engine disturbance the inertia torque, is also parallel to the crankshaft axis (Yu *et al*. 2001). For multi-cylinder engines, the components of an unbalanced engine disturbance depend on the number and arrangement of the cylinders in the engine. For a four-cylinder, four-stroke engine, the frequency of fundamental disturbances is at the second order of the engine speed (Yu, Naganathan, and Dukkipati, 2001).The frequency range is 20-200 *Hz* for an engine speed range of 600 to 6000 *rpm*.

1.1 Hydraulic Engine Mounts and Bushings

In the 1980s, hydraulic engine mounts were devised to attain better frequency and amplitude response characteristics compared to those of conventional elastomeric and rubber-metal engine mounts. Typically, a hydraulic bushing consists of a cast rubber press fitted inside an aluminum bracket. The rubber has three chambers, two on the top and one on the bottom. The chambers are filled with a mixture of water and ethylene glycol. The two top chambers are regarded as compliance chambers, since they are flexible for the volume changes. These two compliance chambers are connected with a relatively wide track which does not contribute to the dynamic performance of the compliance chambers. Therefore, for modeling purposes, the two top chambers are considered a lumped compliance chamber. The chamber on the bottom exhibits a small amount of compliance, since it supports most of the static engine load and as a result, it is manufactured thick. This chamber is connected to the compliance chambers by a long narrow track, called the inertia track. Since engine vibrations cause the lower chamber to pump the fluid to the compliance chambers, that chamber is called a pumping chamber.

Hydraulic bushings are very similar in performance and functionality to hydraulic mounts. The common feature of all hydraulic mounts is that they cause high damping at high amplitudes, and low damping at low amplitudes. Hydraulic mounts and bushings can meet two conflicting design criteria, by exhibiting nonlinear dynamic properties which vary with both the deflection amplitude and the excitation frequency (Flower, 1985). First, the resonance control in the rigid body vibration region of the engine mounting system ranges from 5 to 30 *Hz*. Such control is achieved through high damping and stiffness for high deflection amplitudes. Secondly, the vibration isolation

characteristics are exhibited beyond this frequency region with low damping and stiffness, when the deflection amplitude is low (typically, below 0.2 mm). The precise mechanisms producing such spectrally varying and amplitude-sensitive behavior do not exist in nonlinear fluid damping devices.

Cavanaugh (1996), Bernuchon (1984), and Corcoran and Ticks (1984) have written most of the original papers in this field. In addition, they have introduced the principal nonlinear characteristics of hydraulic engine mounts. Also, Clark (1985) has identified the basic principles for optimizing the dynamic performance of mounts. Various types of hydraulic mounts and bushings have been developed for vehicle mount systems by Golnaraghi, Nakhaie, and Geisberger (2002). All the hydraulic mounts reported in the literature are conceptually identical. Their differences are mainly in their detailed structural designs.

Singh *et al*. (1992) have confirmed experimentally that a simple model of a hydraulic mount can be used to model the system at low frequencies, since the contribution of the higher modes of vibration are negligible. Singh *et al*. (1992) have also pointed out that the compliance of the mount is dominated by the rubber, and the effects of fluid compressibility are insignificant. In addition, Kim and Singh (1993) have studied the nonlinearity in the various components of a hydraulic mount without a decoupler, behaving similarly to a hydraulic bushing. From this study, it is found that the inertia track produces quadratic fluid damping and that the nonlinearity of the rubber compliance can be neglected.

Colgate, Chang, Chiou, Liu, and Keer (1995) have examined the dynamic stiffness response of a hydraulic engine mount to composite sine inputs, roughly simulating

simultaneous engine and chassis vibrations. However, this is not an accurate model, since the engine input is force, not displacement, indicating the benefits of a base excitation experiment.

Using experimental methods pioneered in the early 1990s by Kim and Singh (1993); Geisberger, Khajepour, and Golnaraghi (2002) have developed an excellent experimental apparatus to extract the dynamic response of all engine mount subsystems. From this investigation, Geisberger *et al*. (2002) have created an extensive model, including several accurate nonlinearities such as decoupler flow resistance to yield accurate results over a wide range of frequency and amplitudes.

Also, Golnaraghi and Jazar (2001, 2002) have devised a simple model of a hydraulic mount with only a decoupler, and demonstrated the validity of the model experimentally for both low and high frequencies, as well as a nonlinear study of decoupler dynamics using perturbation methods.

1.2 Mount Parameter Optimization

It is well known that conventional vehicle engine isolation is achieved by passive elements. For a passive system, the system parameters are invariable after they are selected. Therefore, the isolator parameters must be carefully selected during the design period. However, this choice involves a number of compromises, arising from the desire that a isolator must be soft to minimize the acceleration levels and simultaneously it must be stiff enough to control the changes of the engine vibration amplitude.

For a long time, efforts have been made to have the passive isolation system work in an optimal manner by optimizing the parameters of the isolator system. However,

because of the intrinsic limitation of a passive isolation system, the improvement is effective only in a certain frequency range. Also, the optimal results are dependent on the cost function of the system. Until now, there has been no uniformly accepted cost function for isolation systems, even for a simple linear one degree of freedom (1 DoF) vibration suspension system.

Pintado and Benitez (1990) have optimized a four-wheel independent suspension model in the time domain by minimizing the acceleration of the suspension system at a design point, when the system parameters such as mass, damping and stiffness are bounded. Baumal *et al*. (1998) applied Genetic Algorithms to optimize a 2 DoF quarter-car model, based on ride quality. Tamboli and Joshi (1999) have optimized a passive suspension system when it is subjected to random vibrations. Sun (2002) has optimized the walking-beam suspension system by minimizing the probability of the peak value of the tire load exceeding a given value, when the system is subjected to rough pavement road surfaces. To optimize the damping ratio and stiffness in a linear vibration isolator, the root mean square (RMS) of the absolute acceleration and displacement are used in the frequency domain (Chalasani, 1986). Jazar *et al*. (2003) have attained an optimal curve representing the minimum of the RMS acceleration of the sprung mass with respect to the RMS relative displacement. The resultant curve is used to select the optimal damping coefficient and stiffness, when the suspension system endures a road excitation in the range of zero to 20 *Hz*.

Different methods, applicable in the optimization of this system have been proposed by Kamper *et al* (1971). The optimization techniques are concentrated in the frequency domain (Royston, and Singh 1996; Narimani, Golnaraghi, and Jazar 2003,

2004). The complexities of describing the phenomena and neglecting the response of the system in the time domain are the two shortcomings of these approaches.

The art of optimization can be taken to any level. Modern computing power permits optimization on an unimaginable computational scale. Lin, Luo, and Zhang (1990) have developed an optimization strategy for an n DoF system. The method, presented by Lin *et al*. (1990), uses a relatively complex cost function and produces good response results, but at the cost of being computationally intensive and highly sophisticated.

In addition to the standard linear analysis of isolators, it is very common to conduct nonlinear studies. This area of research is of great interest because of the potential to discover bizarre stability behaviour such as bifurcations in the case of cubic systems, as shown by Oueini, Chin, and Nayfeh, (1999). Golnaraghi and Jazar (2002) have found that the nonlinearity in engine mount decouplers can cause high frequency instabilities. Narimani, Golnaraghi, and Jazar (2004) have also analytically investigated the frequency response of the piecewise linear isolator and showed the occurrence of frequency islands; these phenomena have been confirmed with numerical simulations. However, a vigorous stability study is not the main focus of this nonlinear research. Instead, the potential to use nonlinearity to manipulate steady state vibration is examined, with the intent to optimize a simple passive isolator. Nayfeh, Emaci, and Vakakis (1997) have used various orders of damping and stiffness nonlinearity in a 3 DoF vibration isolator. Nayfeh *et al*. (1997) essentially have transferred the vibration energy to a bounded nonlinear mode of vibration, known as nonlinear normal modes (NNMs). More recently, Vakakis, McFarland, Bergman, Manevitch, and Gendelman (2003) have

implemented NNMs in a technique called energy pumping, using cubic nonlinearity. Vakakis *et al*. (2003) have claimed that over 80% of the input energy can be absorbed by the NNMs.

1.3 Active Mounts and Bushings

The idea of designing a passive linear isolator which can minimize the force transmitted and simultaneously minimize the relative displacement is unrealistic. Isolation from force cannot be achieved without the cost of deflection (Andrews, 2002).The need for active or semi-active systems comes from the increasing demands to minimize the transfer of the engine vibration energy to cabin noise, as well as the continuing decrease in the mass of the vehicle leading to more engine vibrations and less rigidity. Due to this and the hydraulic bushing application limitations, the development of cost effective semi-active or active isolation solutions is the next frontier in engine isolation problems. Moreover, the introduction of Variable Displacement Engines[1] (VDE) has intensified the pursuit for a controllable isolator.

Producing a reliable active mount is difficult since it requires an actuator, adequate sealing, moving parts, and possibly large amounts of energy for the actuator, not to mention other design issues. In an active isolating system, generating a proper control signal to change the characteristics of the isolator effectively is essential; basically the damping and stiffness of an active isolator must be adjusted for the optimum values (Inman, 2001). Active suspensions, which are currently the subject of intense studies, are

[1] DaimlerChrysler's Multi-Displacement System (MDS) Mercedes-Benz's Active Cylinder Control (ACC), General Motors' Active Fuel Management (AFM), and Honda's Variable Cylinder Management (VCM)

intended to overcome the problem of maintaining an optimal suspension performance for a wide range of speeds and road conditions (Hall and Tang, 1990).

In the absence of proper passive and semi-active isolators, active controllers have been adopted for numerous industrial applications, including helicopter rotor isolation (Smollen, Marshall, and Gabel, 1962; Crede and Cavanaugh, 1985), aerospace (Smith and Lum, 1968; Leatherwood and Dixon 1968), military fighters (Calcaterra and Schubert; Schubert and Ruzicka, 1969), isolation in aircraft (Swanson and Miller, 1993), automobiles (McDonald, Elliott, and Stokes, 1991), wafer production (Anderson and Houghton, 2001), Naval systems (Winberg, Johansson, and Lago, 2000), and aircraft cabin noise reduction (Stothers, 2002).

There are various controlling techniques to achieve optimal parameter values in active isolators (Serrand and Elliot, 2000; Stein 1995). In the past decade, researchers have investigated nonlinear vibration absorbers with internal resonance and energy transfer approaches. Golnaraghi (1991) has introduced the concept of using a nonlinear absorber based on the internal resonance phenomenon, and Tuer *et al*. (1994) has extended the theory to active systems.

Some of the related work in active isolator design is reported in marine isolation. Here, the vibration that propagates from propulsion and auxiliary machinery can cause significant problems associated with passenger and crew comfort. Moreover, there is the generation of acoustic noise from the hull, creating a severe detection hazard in a naval vessel and for civil vessels such as those used by fishery research organizations (Daley, 1998; Darbyshire and Kerry, 1997; Johnson and Swinbanks, 1996). At early stages, the isolation depended on the electromagnetic levitation of the machinery propeller; however,

the original concept required large numbers of actuators, and therefore, represented an expensive solution. Later, the local mount controller was based on a modal LQG solution that had a feedforward and high-gain feedback component (Daley, Hatonen, and Owens, 2006). Recently, BAE Systems have been developing an active isolation technology known as the *smart spring* mounting system (Daley, Johnson, Pearson, and Dixon, 2004). This is a hybrid active/passive solution that is a more practical and lower cost development of fully active technology.

There are several active control engine mounts reported in the literature. Kosuke and Tatsuhida (2006) have placed an actuator in the lower section of the hydraulic bushing (Kosuke, 2006). Their actuator controls the engine mount characteristics by means of the fluid in the pumping (main) chamber. Hillis *et al.* (2005) have used a magnetic actuator, similar to a voice coil actuators, to design an active engine mount (Hillis, Harrison, and Stoten, 2005). The passive section of the mount is designed to have characteristics similar to a standard passive hydraulic mount. The actuator controls the diaphragm and changes the pressure in the main fluid chamber. A similar actuator has been earlier designed by Yoshiharu *et al.* (1999) and Nakaji, Satoh, Kimura, Hamabe, Akatsu, and Kawazoe (1999) to control the active engine mount characteristics by controlling the main chamber fluid pressure. Hartono *et al*. (1994) have utilized piezoelectric actuators in their active engine mount. This active mount is placed between the jet engine and the fuselage of an airplane.

1.4 Semi-Active Mounts and Bushings

Similar to design of active isolators, the design of semi-active isolators requires an actuator and moving parts resulting in the poor traits of an active mount with limited

incremental performance. Semi-active isolators offer a significant improvement in performance over passive isolators (Schubert, 1969; Shoureshi, 1986; Karnopp, 1974; Duclos, 1987; Ushijima, 1988). These systems benefit from the advantages of active systems with the reliability of passive systems. If the control system fails, the semi-active isolator can still work in the passive mode. In addition, the power consumption of these systems is very low; that is, they can change their characteristics to make different levels of resisting forces according to a low power-commanding signal. These characteristics render the semi-active devices attractive in applications where reliability is the main issue.

Although there are many different semi-active mount designs, a new manufacturing trend is to use Electrorheological (ER) and Magnetorehological (MR) fluids. These smart fluids, ER and MR fluids, have similar properties. Their resistance to flow and their energy dissipation characteristics can be modulated through an applied electric field or electro-magnetic field.

ER fluids are comprised of a mixture of semi-conducting particles in a dielectric carrier liquid, and were first discovered by Winslow (1949). ER fluids are activated by a high electric field in the range of $8\,kV/mm$ (Peel *et al*., 1996). The application of the electric field to the fluids enhances the shear stress development. However, the relatively low shear force and high working voltage prevent the use of ER fluids in many industrial applications.

MR fluids are composed of magnetically polarizable particles suspended in a low viscous fluid media. When the external magnetic field is changed, the viscosity of an MR fluid reversibly changes in microseconds. This effect was first observed by Rabinnow

(1948). Without a magnetic field, an MR fluid has the properties of a Newtonian fluid; however, with a magnetic field, the particles align themselves with respect to the field, and form chains or columns. As a result, the viscosity of the fluid varies. The yield stress of the MR fluid depends on the type of magnetic particles in the fluid, the viscous fluid, the particle volume density, and the strength of the magnetic field. The yield strength of MR fluid is 50~100 *kPa* (Dyke *et al*., 1996).

Although MR devices are displayed in different forms, they can be classified into three working modes: flow mode, shear mode, and squeeze mode (Jolly *et al*., 1999). For the flow mode, the fluid is forced to flow through a fixed pole magnetic field. Examples of flow mode devices are servo-valves, dampers, and shock absorbers. For the shear mode, the fluid is moving magnetic field. Shear mode devices include dampers, clutches, brakes, and chucking devices. In the squeeze mode, the MR fluid is subjected to a tensile and compressive load by oscillating a plate. Since the fluid tends to be squeezed out of the electrode, there is also a shear force that is generated, in addition to the imposed tension or compression. The squeeze mode has been appropriate in low motion, high force applications (Jolly and Carlson, 1996). A comparison of the three working modes in Figure 1-1, indicate that the shear mode can produce a wider range of variable damping forces with a large relative motion. Moreover, in the shear mode damper, the zero–field damper force is smaller than that in other modes. The provision of a small damping force is a key characteristic for a damper working in the vehicle suspension system because when a vehicle runs on a road with a low roughness, a low damping force results in a better ride comfort.

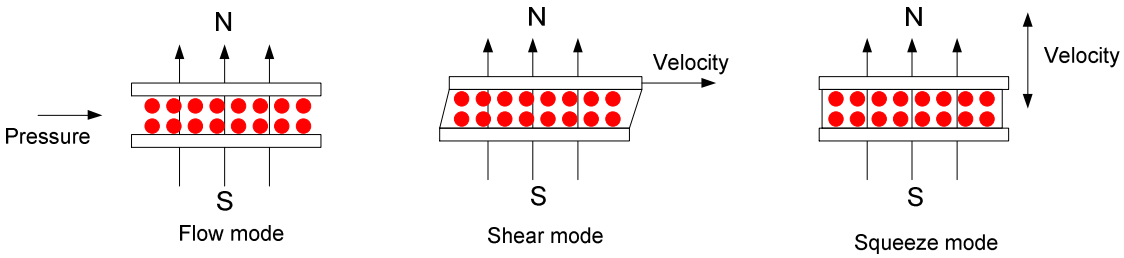

Figure 1-1: MR fluid working mode

The yield stress of MR fluids is dependent on the magnetic interaction of the particles in the MR fluid. Until now, most static shear stress models of MR fluids have been based on the magnetic dipole interactions between two adjacent particles within a particle chain. These inter-particle interactions are then averaged over an entire sample to yield a model of the bulk magnetorheological effect (Harpavat, 1974; Spasojevic *et al.*, 1974).

Jolly *et al*. (1996) have proposed a quasi-static, one-dimensional model with the same assumptions as Harpavat (1974). Jolly's model suggests that the MR material stress is quadratically related to particle magnetization. Borcea (2001) has created a model that takes into account the fully coupled magneto-elastic interactions. The distribution of the magnetization in the material is calculated by the minimum energy principle of magneto-elasticity. By simplifying the dipole interactions in the same direction as the external field, Shiga *et al*. (1995) have analyzed the modulus change of the material. Also, Shiga's model takes into account only the magnetic interaction between the two nearby dipoles, indicating that the increasing shear modulus is quadratically dependent on the magnetic field intensity. Ginder (2000) and Davis (1999) have employed the finite element analysis method to determine the values of the modulus with a varied magnetic field. In summary, for the available dipole interaction models only the static yield stress is considered, but

they provide an elementary physical model that represents the relationship between the magnetic strength and shear stress.

The applicability of MR fluid in vibration isolation was first demonstrated by Peel *et al*. The industry adopted the application in the 1980s. As a follow up, Jolly *et al.* (1999) and Davis (1999) have designed and introduced a mathematical and mechanical model using MR fluids. MR semi-active systems represent low cost, low energy consumption, and potentially, a very effective isolation solution with no moving parts. Over the next 20 years, vibration isolators based on MR fluids should thrive.

Recently, there have been several applications of electrorheological (ER) fluids to mounts and isolators and, but not nearly as many, some similar applications of MR fluids. Williams, Rigby, Sproston, and Stanway (1993) have built a simple model of an automotive engine mount. They were able to mathematically simulate the steady state behavior, and experimentally generate promising results with their scaled model. This design utilizes the squeeze flow mode properties of the engine mount. A full scale prototype of a flow mode ER engine mount have been proposed by Hong, Choi, Jung, Ham, and Kim (2001), demonstrating that the fluid can reduce the transmissibility of acceleration and displacement using skyhook controllers. In essence, a MR hydraulic bushing is a vibration isolator which is controlled by a microchip. The microchip, in conjunction with sensors to quantify the vibrations and provide feedback, controls an input electric current to the hydraulic bushing. This current creates a magnetic field in the inertia track connected to the chambers of the bushing filled with MR fluid. As the hydraulic bushing begins to vibrate, it pumps MR fluid through the inertia track from one chamber to the other and vice versa. Thus, the magnetic field, induced by the microchip

controller can be used to control the flow of fluid, (by increasing the yield stress of the fluid via the magnetic field), through the inertia track, changing the characteristics of the hydraulic bushing.

There exists very little prior work on MR engine isolators. Of the very few documented experiments, Choi, Lee, Song, and Park (2002), and Choi, Song, Lee, Lim, and Kim (2003) have designed and manufactured a mixed mode MR engine mount and conducted base excitation experiments to complete a hardware-in-the-loop full car model to demonstrate the effectiveness of their design. Also, with a skyhook controller, Shtarkmen (1993) has patented a similar design.

However, to date, there exists little evidence that there has been a great deal of research conducted on the application of MR fluid engine mounts, operating in the flow mode or valve mode. One patent does exist, for implementing MR fluid in an engine mount with a decoupler (Baudendistel *et al*., 2002). Also, MR damper designs exist which utilize the flow mode characteristics and many of them are patented by Carlson, Chrzan, and James (1994). It has been shown by Kuzhir, Bossis, and Bashtovoi (2003), as well as Kuzhir, Bossis, Bashtovoi, and Volkova (2003), that MR fluids perform best in a pressure driven flow where the orientation of the magnetic field is perpendicular to the direction of the flow. A more efficient design has been presented by Gorodkin, Lukianovich, and Kordonski (1998) and patented by Kordonski *et al*. (1995).

A theoretical study of the effectiveness of an MR bushing has been conducted by Ahn, Ahmadian, and Morishita (1999), and Ahmadian and Ahn (1999); however, the bushing presented by Ahn *et al*. (1999) has a slightly different model than the mount referred to in this particular study. Moreover, Ahn *et al*. (1999) and Ahmadian and Ahn

(1999) have only considered increasing the damping, not the fact that the MR fluid can be useful in allowing the damping in an otherwise ordinary mount to be very small, and increasing it significantly via MR effects around the resonance.

1.5 Variable Displacement Engine Isolation

The real need for a new isolator spawns from the need to minimize fuel consumption, leading to the implementation of VDEs, also known as cylinder deactivation. A VDE system supports different load conditions, thus, it is too difficult to maintain the NVH performance of the vehicle with the current isolator design. There are various mechanisms to influence the force produced by an isolator; in particular a hydraulic engine bushing and mount. For every mechanism, there are several proposed designs for active and semi-active mounts. With the exception of the design proposed by Matsuoka *et al*. (2004) for the 2005 Honda Odyssey, none of the previous designs appear to be in production for the automotive market.

Improvement in the fuel economy has led automotive manufacturers to design engines which automatically switch between modes of operation. Each mode is characterized by the number of cylinders firing, depending on the requirements of the driver. For example, for accelerating, all six cylinders in a V6 engine should be firing to provide the maximum amount of power; however, once the target cruising speed is reached and the load on the engine decreases, the Engine Management Unit (EMU) can remove any three cylinders from the firing sequence (Hardie *et al*., 2002). More than 25 years ago, Jackson and Jones (1976) have discovered that this technique requires 25% less gas in a V16 cylinder engine by using deactivation of the cylinders. Also, the authors have reported torsional vibrations during the switching to the VDE mode, requiring a

special torsional analysis. High energy savings are achievable largely due to the fact that a steady state speed requires only a minimal amount of power (less than 30 HP) with respect to the maximum power of modern vehicles which can exceed 300 HP (Ashely, 2004).

The change in the number of firing cylinders presents a vibration loading beyond the isolating capabilities of a conventional hydraulic bushing. Although the mechanical unbalanced vibrations, occurring at the frequency of rotation of the crankshaft, remain the same (first order vibrations), the other orders are halved (with half of the cylinders deactivated). For example, the frequency of the combustion force, produced by a four-stroke engine with P cylinders, is

$$f_n = N_{crankshaft}\left(\frac{1\ \min}{60\ s}\right)\left(\frac{1\ cycle}{2\ rev}\right)P,$$

where $N_{crankshaft}$ is the RPM of the crankshaft (or engine), fn is the nth order of vibration, n is the multiple of the crankshaft rotational frequency which is P/2 in this case, and the cylinder fires once every two rotations of the crankshaft. Consequently, for a six cylinder engine, a third order torsional vibration is induced by the combustion and firing of the engine (Rao, 2004). When the engine switches to three cylinders, the torque produced by the firing occurs in an order of 1.5, in agreement with the studies by Matsuoka, Mikasa, Nemoto, and Gehm (2004).

As mentioned by Matsuoka *et al*. (2004), since the net amount of the crankshaft torque produced must be constant between the two modes, the three cylinder combustion pressure must double. There are half as many cylinders, and therefore, the forces which induce the torsional vibration double in magnitude. The realization is that the appropriate isolator should be half as stiff in the operating frequency range of the three cylinder mode

of the engine. This is approximately 1000-2200 RPM ($f_{1.5} = 25 - 55Hz$). In addition, the isolator must maintain its performance in the six cylinder mode as well as the current products do. The realization is that *the appropriate isolator should be half as stiff in the operating frequency range of the three cylinder mode of the engine*: approximately between 1000-2200 RPM ($f_{1.5} = 25 - 55Hz$). In addition, *in the six cylinder mode the isolator must maintain the performance levels comparable to* (*or better than*) *those of existing conventional products.*

1.6 Thesis Overview

The need for a semi-active or an active isolator for automobile applications is established in Chapter 1. Besides the high demand for versatile isolators to improve ride quality, the introduction of the VDE engine is the principal motivation for this research activity. The objective is to design and manufacture a semi-active and an active engine bushing to solve the VDE isolation problem.

Passive mount parameter optimization is the subject of Chapter 2. The passive components such as the stiffness and damping of the rubber bulk of a conventional hydraulic bushing are optimized in both the time and frequency domains. Although designing a passive bushing is not an objectives of this research, the RMS optimization of these parameters is essential due to the fact that the static load of the engine should be supported the passive components, even in semi-active and active bushings. The base and forced excitations are studied separately. The RMS of the absolute acceleration and relative displacement are adopted for the base excitation optimization, whereas the RMS of force transmissibility and absolute displacement are used for the forced excitation optimization.

In Chapter 3, a simplified linear model, corresponding to a hydraulic bushing, is proposed. The various components of a conventional hydraulic bushing are represented by a lumped equivalent module. A mathematical demonstration of the lumped model is then derived. An experiment is performed to validate the proposed mathematical model. Various parameters of the conventional hydraulic bushing are identified by a curve fitting process. The dual dynamic performance of the hydraulic bushing is discussed in detail, in both time and frequency domains. The essential features of a conventional hydraulic bushing and the effect of the key components of the hydraulic bushing on the dynamic response are detailed.

Chapter 4 deals with the inertia track effect on the dynamic stiffness response of conventional hydraulic bushings. It is shown numerically that the soft region of the dynamic stiffness response in a conventional hydraulic bushing can be extended to high frequencies by a suitable selection of the inertia track size (reducing the length and increasing the cross-sectional area). In addition, although this is experimentally confirmed, not enough damping is produced by the short inertia track.

To overcome the damping problem an MR chamber is designed and tested, as described in Chapter 5. The chamber's MR valve is energized by a solenoid coil. This valve can be classified as a flow mode MR device. The design of the valve allows the iron particles inside the MR fluid to align perpendicular to the flow motion and produce the maximum shear stress. Not only does the MR chamber effectively controls the damping level, but also is economical in its consumption of MR fluid.

The design of an active compliance chamber is discussed in Chapters 6 to 8. it is comprised of a permanent magnet attached to a compliant diaphragm. A solenoid coil is

adopted to attract and repel the permanent magnet to produce mechanical pulses. The lumped and mathematical model of the active chamber is projected in Chapter 6. It is found that the magnetic force produced between the solenoid coil and permanent magnet, is a nonlinear function of the distance and the applied electrical current. A linearization technique is implemented to simplify the analysis. The experimental results validate the linearity of the active chamber in the desired frequency region.

The novel active chamber is connected to the conventional hydraulic bushing. Different inputs are applied to activate the permanent magnet. More complex signals produce sophisticated responses. The effect of the active chamber on the pumping chamber pressure response and the bushing dynamic response are studied in Chapter 7 and Chapter 8 respectively.

Chapter 9 pertains to the difficulties encountered during the research, as well as some remedies. Lastly, the conclusion and recommendations for future work are found in Chapter 10.

1.7 Contributions Made in this Thesis

This thesis has contributed to advancement of knowledge in many areas. The key contributions herein have resulted in the following Journal and Conference submissions:

1. Arzanpour, S., Schubert, B., and Golnaraghi, M.F., 2006,"Dynamic Stiffness Control in Hydraulic Bushings for Vehicle Engines with Cylinder Deactivation System", Submitted to *Journal of Vibration Control*
2. Arzanpour, S. and Golnaraghi, M.F., 2006, "A Novel Semi-Active Bushing Design for Variable Displacement Engines", Submitted to *Journal of Intelligent Material Systems and Structure*
3. Arzanpour, S. and Golnaraghi, M.F., 2006, "Development of a Bushing with an Active Compliance Chamber for Variable Displacement Engines", Submitted to *Journal of Vehicle System Dynamics*

4. Arzanpour, S. and Golnaraghi, M.F., 2006, "Development of an Active Compliance Chamber to Enhance Performance of Hydraulic Bushings for Variable Displacement Engines", Submitted to *Journal of Sound and Vibration*

5. Arzanpour, S., Eslaminasab, N., Narimani, A., Schubert, B. and Golnaraghi, M.F., 2006, "A Novel Technique for Frequency and Time Optimization of Automotive Engine Mount Parameters" *Proceedings of IMECE2006, ASME International Mechanical Engineering Congress and Exposition November 5-10, 2006, Chicago, Illinois, USA*

6. Arzanpour, S. and Golnaraghi, M.F., 2006, "Developing of an Active Hydraulic Bushing for Multi-Displacement Engines", *Proceedings of IMECE2006, ASME International Mechanical Engineering Congress and Exposition November 5-10, 2006, Chicago, Illinois, USA*

In addition this thesis has result in an invention that has been filed as a US provisional patent

P1. Electronic Control Magnetorheological Engine Vibration Isolator (Co-inventors: Arzanpour, S., Schubert, B. and Golnaraghi**,** M. F.; Applicant: University of Waterloo), *TTLO #8810-7209, US Provisional Patent Application No. 60/750056 Filed December 14, 2005*.

Chapter 2: Passive Mount's Parameter Optimization

In this chapter a linear 1 DoF engine mount is examined to obtain the optimum mount parameters in a passive configuration. As explained before, an engine mount is a device that is used to isolate the vehicle body from the engine vibrations, forced excitation, and the effects of road-induced disturbances on the engine, base excitation, are minimized. In this study, it is assumed that the system is linear. This allows a simplified analysis of the frequency and time response characteristics in both excitation cases (base and force).

The optimal damping and stiffness values for the isolator are obtained by minimizing certain cost functions in the frequency and the time domains. The cost function is based on RMS of the absolute acceleration and relative displacement in the frequency domain, and on the transmitted acceleration and absolute displacement in time domain. The time and frequency responses of the isolator are optimized by varying the stiffness and damping ratios for both the base and forced excitation cases. After the optimal values are obtained, the results are verified numerically. It is interesting that, although the mathematical model is linear, the time and frequency optimal values are not the same. As a result, this exercise shows that no passive-mount is adequate to deal with all the application specifications and isolation criteria. Here, a novel approach is suggested to select the mount parameters for various passive or active configurations.

2.1 BACKGROUND

2.1.1 Linear Passive Engine Mount Model

To study the passive 1 DoF engine bushing, a simple model is constructed. It is composed of a linear spring and damper, as illustrated in Figure 2-1. In the literature, this model is known as the Kelvin (Voigt) model of rubber. The equation of motion of this model is

$$m\ddot{x} + c(\dot{x} - \dot{y}) + k(x - y) = m_o e\omega_{dr} \cos(\omega_{dr} t) \qquad (2.1)$$

which can be rearranged to the following form:

$$m\ddot{x} + c\dot{x} + kx = m_o e\omega_{dr}^{\,2} \cos(\omega_{dr} t) + c\dot{y} + ky\,, \qquad (2.2)$$

where m is the effective mass of the engine, c is the damping coefficient, k is the stiffness, and m_o is the mass of the engine unbalance of eccentricity e and rotational frequency ω_{dr}. The absolute displacement of the engine and base are represented by x and y, respectively, and the relative displacement is denoted x_r. The force transferred through the mount is

$$F_T(t) = m\ddot{x} - m_o e\omega_{dr}^{\,2} \cos(\omega_{dr} t) = c(\dot{y} - \dot{x}) + k(y - x)\,. \qquad (2.3)$$

The design objectives can now be restated in terms of the above system parameters, the challenge is to find the optimal linear stiffness (k) and damping (c) which constrain the displacement of the mass m, measured by the coordinate x_r or x, yet minimize the transferred force $F_T(t)$ criteria due to either a base excitation measured by the coordinate y, or an input force $F(t)$ generated by the engine. With this linear model, the principle of superposition permits the study of the two disturbances; base excitation and unbalanced forcing, independently.

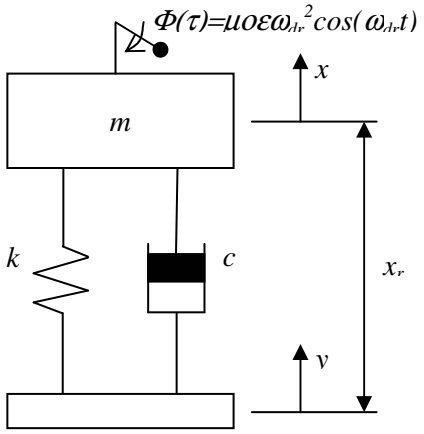

Figure 2-1: Schematic of a linear 1 DoF isolator representing an engine mount

2.1.2 Base Excitation

Machines or their parts are sometimes excited trough their elastic mounts. For the base excitation disturbance, (2.2) can be nondimensionalized and rearranged to yield

$$\ddot{x}_r + 2\xi\omega_n\dot{x}_r + \omega_n^2 x_r = -\ddot{y}, \qquad (2.4)$$

where the parameters are

$$\xi = \frac{c}{2\sqrt{km}} \qquad \omega_n = \sqrt{\frac{k}{m}} = 2\pi f_n \qquad x_r(t)=x(t)-y(t). \qquad (2.5)$$

Note that in the absence of force on the mass, the transferred force becomes

$$F_T(t) = m\ddot{x} = c(\dot{y}-\dot{x}) + k(y-x). \qquad (2.6)$$

Thus, $F_T(t)$ is directly proportional to the absolute acceleration of the mass. From(2.4), the transfer function of the system, relating the absolute acceleration and relative displacement to the input, are (where $r=\omega/\omega_n$)

$$a = \left|\frac{\ddot{X}}{Y}\right| = \frac{\omega^2\sqrt{1+(2\xi r)^2}}{\sqrt{(1-r^2)^2+(2\xi r)^2}}. \qquad (2.7)$$

and

$$\lambda = \left| \frac{X - Y}{Y} \right| = \frac{r^2}{\sqrt{(1 - r^2)^2 + (2\xi r)^2}} . \qquad (2.8)$$

The absolute acceleration and the relative displacement curves are illustrated in Figure 2-2.

2.1.3 Force Excitation

The force excitation is a general name for the vibration caused by an external force in a mass, isolated from a base. Given a forced disturbance in the form of engine unbalance, (2.2) is nondimensionalized to the following form:

$$\ddot{x} + 2\xi\omega_n \dot{x} + \omega_n^2 x = f_o(t), \qquad (2.9)$$

where the disturbance force is

$$f_o(t) = \frac{F(t)}{m} = \frac{m_o e}{m} \omega_{dr}^2 \cos(\omega_{dr} t) . \qquad (2.10)$$

The transferred force is

$$FT(t) = \frac{F_T(t)}{m} = 2\xi\omega_n \dot{x} + \omega_n^2 x . \qquad (2.11)$$

If the magnitude of the force is assumed to be constant, the following transfer functions can be written, relating the transferred force F_T and the displacement of the mass X to the input magnitude, respectively, as

$$\Phi = \left| \frac{FT}{f_o} \right| = \left| \frac{F_T}{F} \right| = \sqrt{\frac{1 + (2\xi r)^2}{(1 - r^2)^2 + (2\xi r)^2}} \qquad (2.12)$$

$$\Lambda = \left| \frac{X}{f_o} \right| = \frac{1}{\omega_n^2 \sqrt{(1 - r^2)^2 + (2\xi r)^2}}, \qquad (2.13)$$

where $r = \omega_{dr}/\omega_n$. Eq (2.12) is a linearly scaled version of the motion transmissibility illustrated in Figure 2-2. Eq (2.13) is depicted in Figure 2-3.

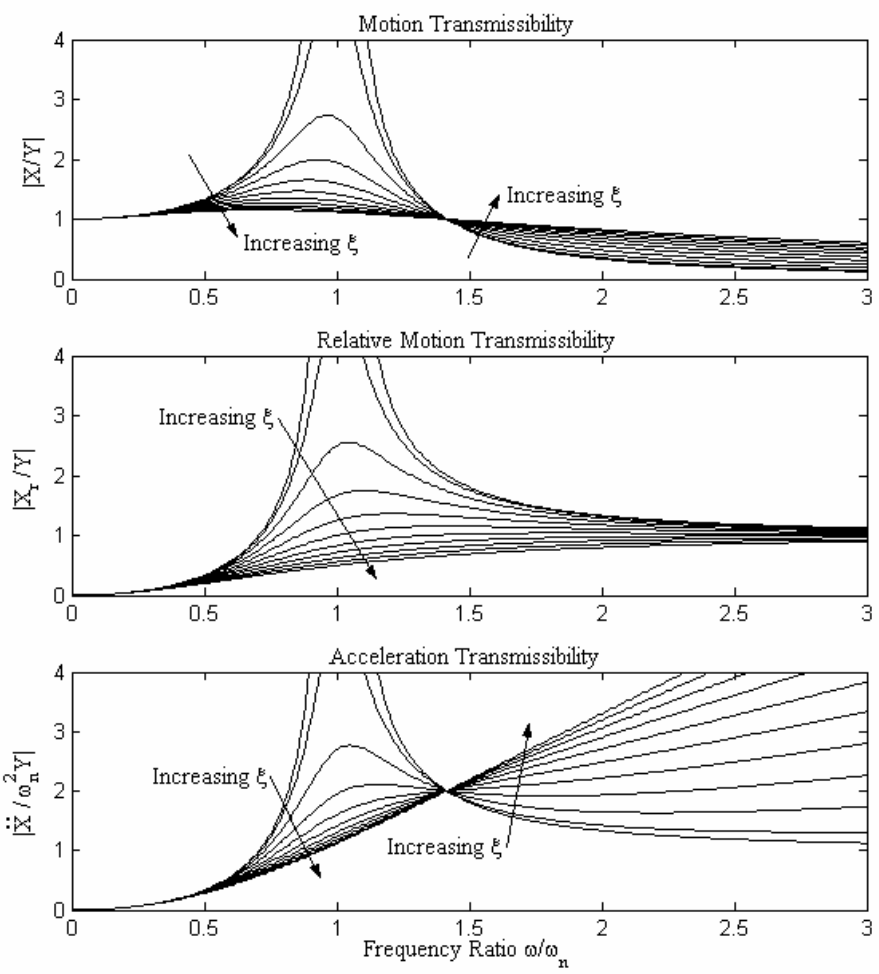

Figure 2-2: The frequency response functions of the base excitation linear passive isolator.

Furthermore, if the amplitude is assumed to vary with the frequency as follows:

$$\left|F\right| = m_o e \omega_{dr}^{\ 2}, \tag{2.14}$$

The transfer functions Ψ and Ω, similar to (2.7) and(2.8), represent the force and the displacement transmissibility, respectively, as

$$\psi = \left|\frac{F_T}{m_o e \omega_n^{\ 2}}\right| = r^2 \sqrt{\frac{1+(2\xi r)^2}{(1-r^2)^2+(2\xi r)^2}} \tag{2.15}$$

and

$$\Omega = \left|\frac{Xm}{m_o e}\right| = \frac{r^2}{\sqrt{(1-r^2)^2+(2\xi r)^2}}. \tag{2.16}$$

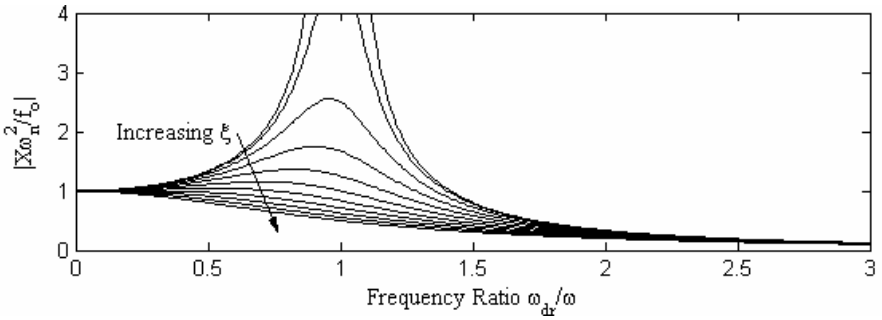

Figure 2-3: Amplitude with respect to static displacement under a harmonic force

2.2 FREQUENCY OPTIMIZATION

The optimum stiffness and damping ratio values of the mount are obtained by using a simple cost function in the frequency domain. In this case, the cost function is defined by using the RMS to average the acceleration and displacement over the frequency range of *0-20 Hz*. The definition of the RMS of function $h(\omega)$ from ω=*0-20 Hz* is as follows:

$$RMS(h(\omega)) = \sqrt{\frac{1}{40\pi}\int_0^{40\pi} h(\omega)^2 d\omega}\,. \qquad (2.17)$$

Hence,

Base excitation	$R = RMS(a)$, absolute acceleration RMS $\eta = RMS(\lambda)$, relative displacement RMS
Harmonic Forced excitation	$\phi = RMS(\Phi)$, force transmissibility RMS $\gamma = RMS(\Lambda)$, absolute displacement RMS
Unbalanced excitation	$\chi = RMS(\psi)$, force transmitted RMS $\Gamma = RMS(\Omega)$, absolute displacement RMS

2.2.1 Base Excitation Optimization

According to the base excitation defined criteria, the following procedure is used to optimize the design parameters in the linear engine mount problem. The RMS acceleration *R* is defined as a function of η by using ξ and ω_n as parameters. It can be

seen from Figure 2-4 that function $R(\eta)$ has a minimum for the constant values of ω_n and a maximum for the constant values of ξ. The line of minima in the R-η plane forms an optimum curve for the linear isolator. Then if the limit value of the RMS of either the acceleration or displacement is known, the optimum values of the damping ratio and natural frequency are easily found by examining Figure 2-4.

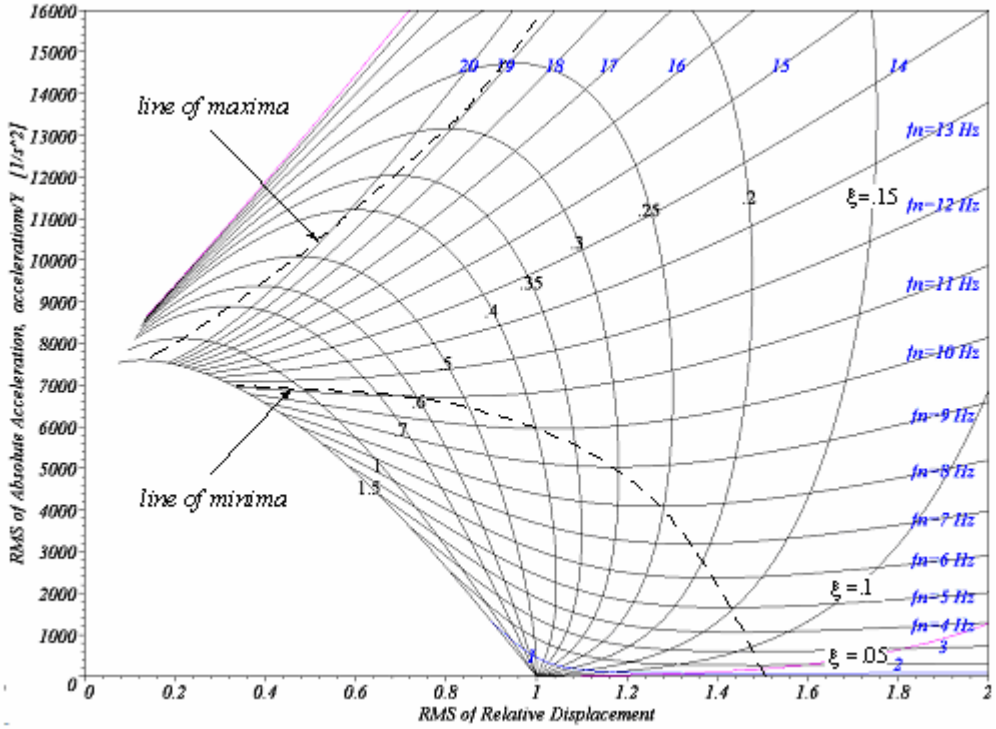

Figure 2-4: Contour curves for the function R=R(η)

2.2.2 Forced Excitation Optimization

2.2.2.1 Constant Amplitude Harmonic Force

As previously shown for the base excitation optimization, the RMS of force transmissibility (ϕ) and displacement (γ) are both functions of ξ and ω_n; thus, for a unique pair of ξ and ω_n, a related value of ϕ and γ can be found to illustrate the preceding results in the $\phi - \gamma$ plane in Figure 2-5. Here, the line of minima represents the optimal damping

ratio which yields the minimum force transmissibility for a given stiffness or natural frequency.

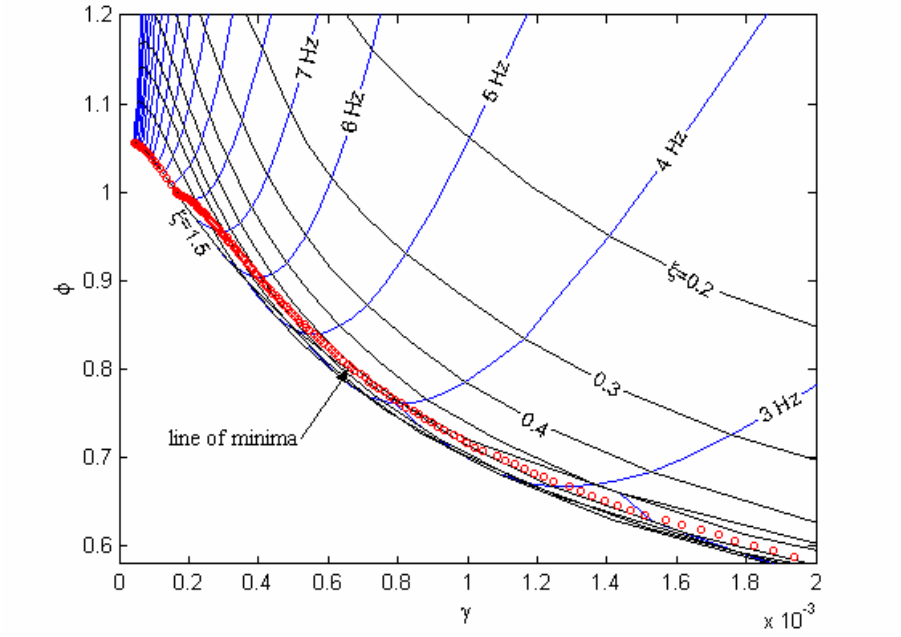

Figure 2-5: The RMS force transmissibility versus the RMS absolute displacement

2.2.2.2 Unbalanced Force ($|F(t)|=m_0 E\,\omega_{dr}^2$)

Similar to Figure 2-4, representing the $R-\eta$ plane discussed in Section 2-2-1, the results of the unbalanced force case are summarized in the $\chi-\Gamma$ plane, Figure 2-6, where a line of minima represents the optimal damping which yields the minimum RMS force transmitted given a certain natural frequency.

2.3 TIME OPTIMIZATION

For time optimization, the main interest is the transient response of the system. Similar to the frequency optimization, the cost functions are the acceleration (force) transmitted, and relative or absolute displacement. The variation of these two functions with the natural frequency (the frequency ratio for the sinusoidal inputs) and damping ratio for the different inputs defines the optimum curve in each case. Since the solution

of the equation of motion depends on the input, a different analysis may be required. To show the optimum curves a unit step, a unit pulse, and sinusoidal inputs are employed.

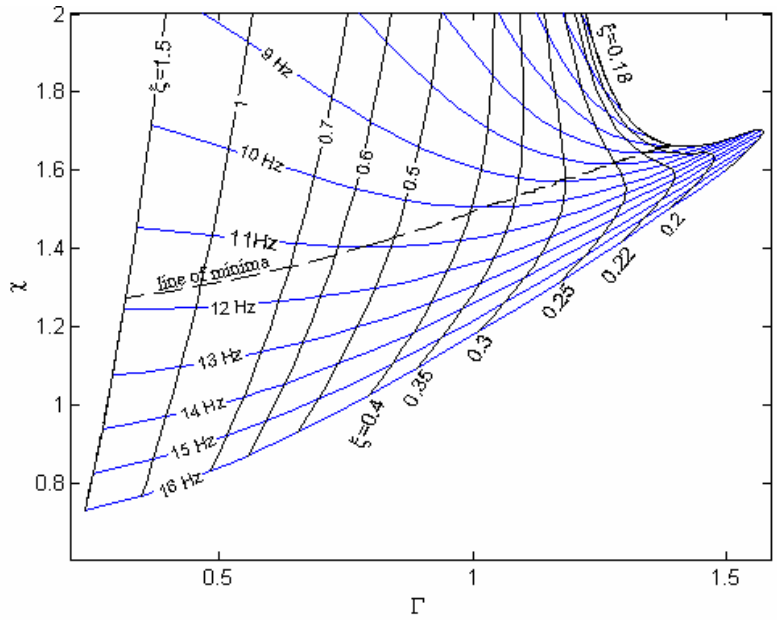

Figure 2-6: The RMS force transmitted versus the RMS absolute displacement

2.3.1 Base Excitation

A simple spring-mass-damper model is used for the base excitation problem, as shown in Figure 2-1. The forcing term can be eliminated from (2.2) such that,

$$m\ddot{x} + c(\dot{x} - \dot{y}) + k(x - y) = 0 . \qquad (2.18)$$

This is the equation of motion in the absolute coordinates. By rearranging (2.18) and expressing it in terms of the relative displacement, (2.4) is derived. These equations are solved for the different inputs. The optimization process for each input is described in the following sections.

2.3.1.1 Unit Step Input

By solving (2.4) for x_r, the response of the system to unit step is,

$$x_{rel}(t) = -\left(\frac{\xi}{\sqrt{1-\xi^2}} \sin(\omega_d t) - \cos(\omega_d t)\right) e^{-\xi\omega_n t} . \qquad (2.19)$$

Since the second derivative of y is zero, the second derivative of (2.19) yields to the absolute acceleration,

$$a(t) = ((1-4\xi^2)\cos(\omega_d t) + \frac{-3\xi + 4\xi^3}{\sqrt{1-\xi^2}}\sin(\omega_d t))\omega^2 e^{-\xi\omega_n t}. \quad (2.20)$$

The peak of relative displacement x_p occurs at

$$t_1 = \frac{\cos^{-1}(2\xi^2 - 1)}{\omega_n\sqrt{1-\xi^2}}. \quad (2.21)$$

The relative displacement peak can be found by substituting (2.21) in (2.19),

$$x_p = \exp(-\frac{\xi\cos^{-1}(2\xi^2 - 1)}{\sqrt{1-\xi^2}}). \quad (2.22)$$

The peak of the absolute acceleration a_p occurs at a different time and it is calculated by

$$t_2 = \frac{2\cos^{-1}(2\xi^2 - 1) - \pi}{\omega_n\sqrt{1-\xi^2}}. \quad (2.23)$$

By substituting (2.23) in (2.20) the absolute acceleration peak is represented by,

$$a_p = \omega_n^2 \exp(-\xi\frac{2\cos^{-1}(2\xi^2 - 1) - \pi}{\sqrt{1-\xi^2}}). \quad (2.24)$$

The curves of the peak absolute acceleration versus the peak relative displacement are drawn in Figure 2-7 for the various damping ratios and natural frequencies. As (2.24) predicts, the dependency of the peak acceleration on natural frequency is boundary limited, and therefore, the lower stiffness results in lower a_p values. Figure 2-7 demonstrates the minimum peak value of the absolute acceleration occurring at $\xi = 0.36$, illustrated by a thick vertical line.

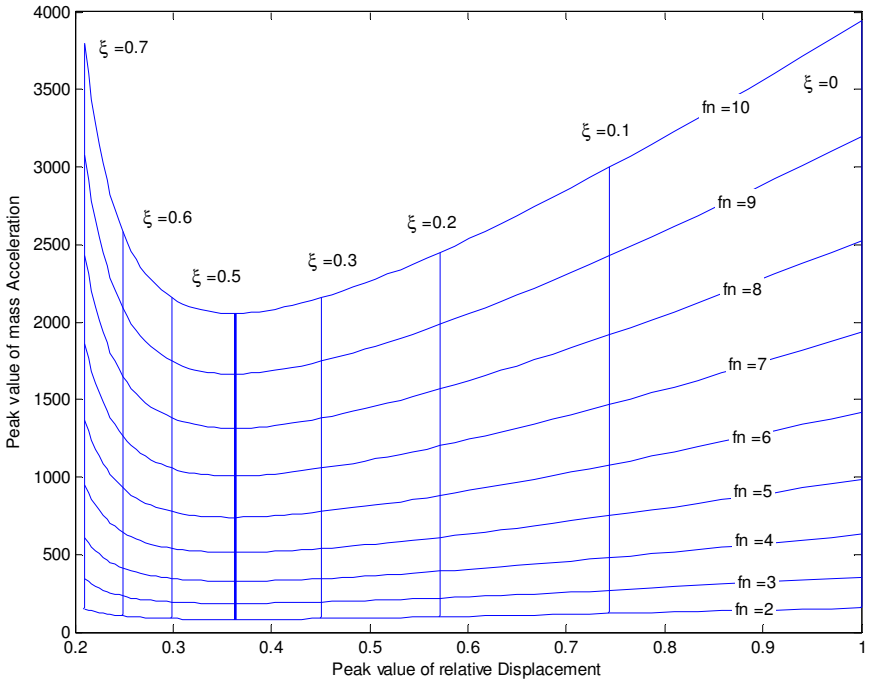

Figure 2-7: Peak value of mass acceleration versus peak value of relative displacement

2.3.1.2 Pulse Input

The superposition of the two step inputs, with equal and opposite amplitudes happening at different starting times, is used to create a pulse response. The duration of the pulse, which is the delay between the two pulses, has a significant effect on the transient response of the system. In reality, if the pulse duration is selected to be long, the system has enough time to settle before the next pulse starts. However, a short duration causes the transient responses to affect each other. Here, the pulse duration is set at 50 *msec* (that is, the negative step input starts 50 *msec* after the positive step). The relative displacement and absolute acceleration equations for this system, when the time is less than 50 *msec*, are the same as (2.19) and (2.20). However, a new set of equations should be derived so that the initial conditions are considered at the instant the negative step input is initiated. The equation of relative motion and absolute acceleration are derived as

$$x_{rel} = (\frac{v_0 + \xi\omega_n x_0 - 2\xi\omega_n}{\omega_n\sqrt{1-\xi^2}} sin(\omega_d t) + x_0 cos(\omega_d t))e^{-\xi\omega_n t}, \qquad (2.25)$$

and

$$a(t) = (\frac{\omega_n((2\xi\omega_n - v_0)\sqrt{1-\xi^2} + x_0\omega_n\xi + v_0\xi^2 - 2\xi^3\omega_n)}{\sqrt{1-\xi^2}} sin(\omega_d t) + \frac{\omega_n((2\xi^2\omega_n - \xi v_0 - x_0\omega_n)\sqrt{1-\xi^2} - v_0\xi + 2\xi^2\omega_n)}{\sqrt{1-\xi^2}} cos(\omega_d t))e^{-\xi\omega_n t}, \qquad (2.26)$$

where x_0 and v_0 are the displacement and velocity of the mass at the time the negative step begins. For such a system, the peak of relative displacement occurs at

$$t_1 = \frac{tan^{-1}\frac{2\xi\omega_n - v_0}{x_0\omega_n + \xi v_0 - 2\xi^2\omega_n}}{\omega_n\sqrt{1-\xi^2}} + \tau, \qquad (2.27)$$

whereas the peak of absolute acceleration occurs when $t = \tau$ or

$$t_2 = \frac{tan^{-1}\frac{\sqrt{1-\xi^2}(8\xi^3\omega_n - 2\xi\omega_n x_0 + v_0 - 4v_0\xi^2 - 2\xi\omega_n x_0)}{-x_0\omega_n - 3\xi v_0 + 2\omega_n\xi^2 x_0 + 4\xi^3 v_0 + 6\xi^2\omega_n - 8\xi^4\omega_n}}{\omega_n\sqrt{1-\xi^2}} + \tau. \qquad (2.28)$$

Figure 2-8 shows the curves of the peak of absolute acceleration with respect to the peak of the relative displacement for different damping ratios and natural frequencies. The simulation results demonstrate the existence of an optimal damping ratio for each natural frequency. The line of minimum is highlighted by a bold line in the graph.

2.3.1.3 Sinusoidal Input

The transient response of the system can also be studied under the sinusoidal base excitation. This kind of input well represents bumpy roads. The sine input is given in (2.29) where Y and ω_b denote the amplitude and the frequency of excitation respectively.

$$y(t) = Y sin\,\omega_b t. \qquad (2.29)$$

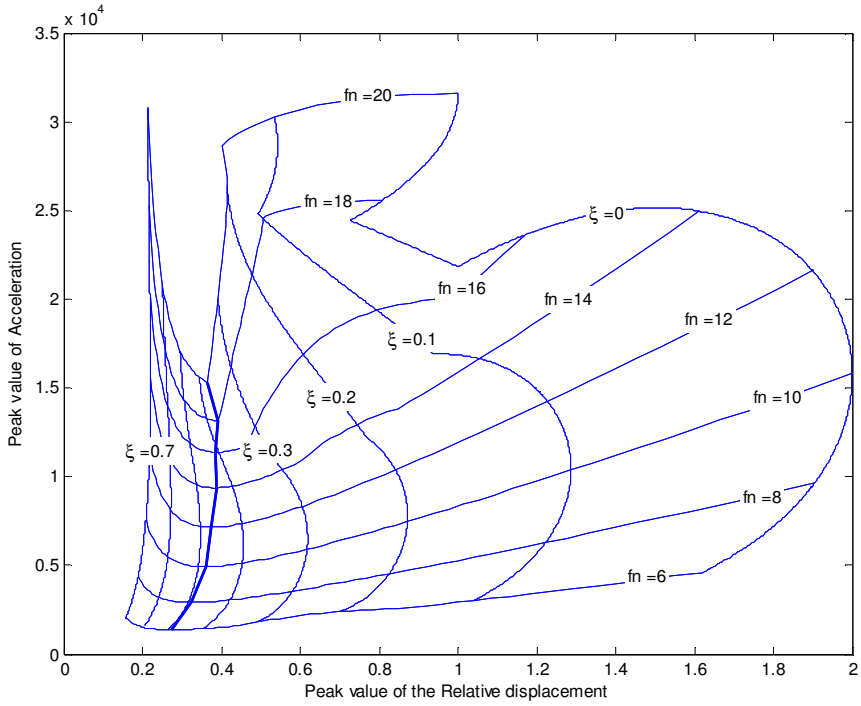

Figure 2-8: Peak value of mass acceleration versus peak value of the relative displacement when the pulse duration is 50 *msec*

To find the relative displacement and absolute acceleration, (2.29) should be substituted in (2.4). The particular solution of the equations of motion for such input is

$$x_{rel} = \frac{\omega_b^2 Y}{\sqrt{(\omega_n^2 - \omega_b^2)^2 + (2\xi\omega_n\omega_b)^2}} sin(\omega_b t - \theta), \qquad (2.30)$$

and

$$a = -Y\omega_n\omega_b^2 \left[\frac{\omega_n^2 + (2\xi\omega_b)^2}{(\omega_n^2 - \omega_b^2)^2 + (2\xi\omega_n\omega_b)^2}\right]^{1/2} cos(\omega_b t - \theta_1 - \theta_2), \qquad (2.31)$$

where $\theta = \tan^{-1}(2\xi\omega_n\omega_b / \omega_n^2 - \omega_b^2)$. The ratio of the maximum response amplitude versus the amplitude of excitation is given by (2.8). The force transmitted to the mass from the base can also be calculated by

$$F(t) = -m\ddot{x}. \qquad (2.32)$$

By substituting (2.30) in (2.32), the force transmitted ratio is,

$$\frac{F_T}{Y\omega_n} = r^2\left[\frac{1+(2\xi r)^2}{(1-r^2)^2+(2\xi r)^2}\right]^{1/2}. \qquad (2.33)$$

As shown in Figure 2-9, the peak values of force, transmitted to the mass, have no minimax with respect to the peak of the relative displacement for the different damping ratios and natural frequencies. However, the relative displacement has a maximum with respect to the peak of the transmitted force. The maximum peak values are represented by the bold line.

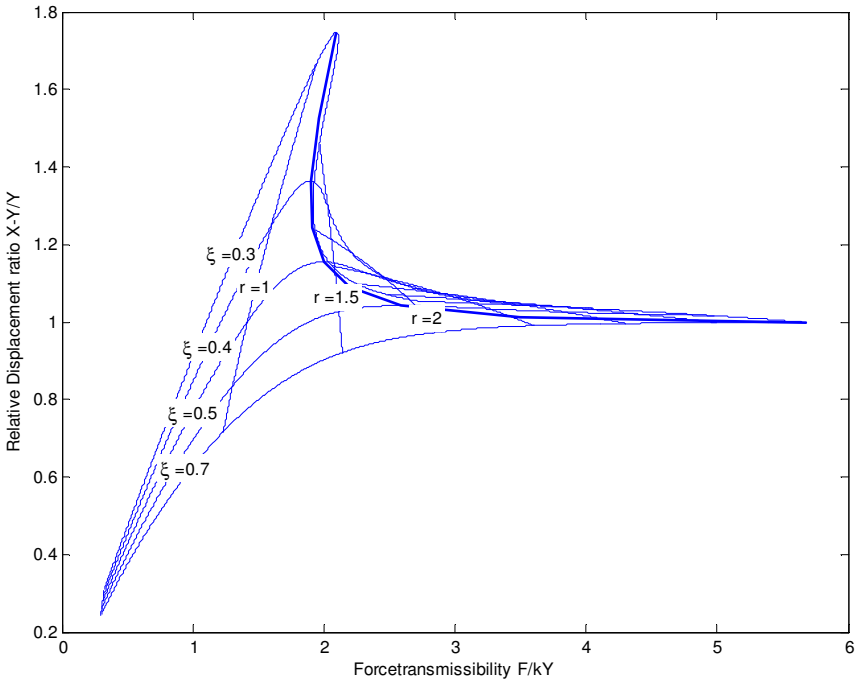

Figure 2-9: Peak value of the relative displacement versus peak value of the mass acceleration.

2.3.2 Forced Excitations

The same spring-mass-damper model can be used for the force excitation case, and (2.9) is used to formulate the optimization criteria.

2.3.2.1 Unbalanced Force

The forcing in this case is written as

$$F = m_o e \omega_{dr}^2 \sin(\omega_{dr} t). \tag{2.34}$$

By substituting (2.34) in (2.9), the particular solution for the normalized differential equation is

$$x_p(t) = X \sin(\omega_{dr} t - \theta), \tag{2.35}$$

where

$$X = \frac{m_o e}{m} \frac{r^2}{\sqrt{(1-r^2)^2 + (2\xi r)^2}} \tag{2.36}$$

and

$$\theta = \tan^{-1} 2\xi r / 1 - r^2. \tag{2.37}$$

The ratios of the maximum force and displacement amplitude, with respect to the frequency ratio, are given by (2.15) and (2.16), respectively. In fact, (2.15) and (2.16) are the same as (2.8) and (2.33) which states that the unbalanced force excitation case has the same optimization results as the base excitation case with the sinusoidal input. Therefore, to avoid duplication, the results are not given here.

2.3.2.2 Step Force

In this case, the displacement equation of the system is derived by solving the differential equation (2.9) for the step input force. The solution is

$$x(t) = \frac{1}{\omega_n^2} - \frac{1}{\omega_n^2 \sqrt{1-\xi^2}} \sin(\omega_n \sqrt{1-\xi^2} t + \theta) e^{-\xi \omega_n t}. \tag{2.38}$$

The acceleration of the system is calculated by differentiating (2.38) twice. Hence,

$$a(t) = -\frac{1}{\sqrt{1-\xi^2}} \sin(\omega_n \sqrt{1-\xi^2} t - \theta) e^{-\xi \omega_n t}. \tag{2.39}$$

It can be concluded from (2.38) and (2.39) that the displacement and acceleration have a linear relationship, reflected in Figure 2-10. Therefore, no minimax point can be identified for this case.

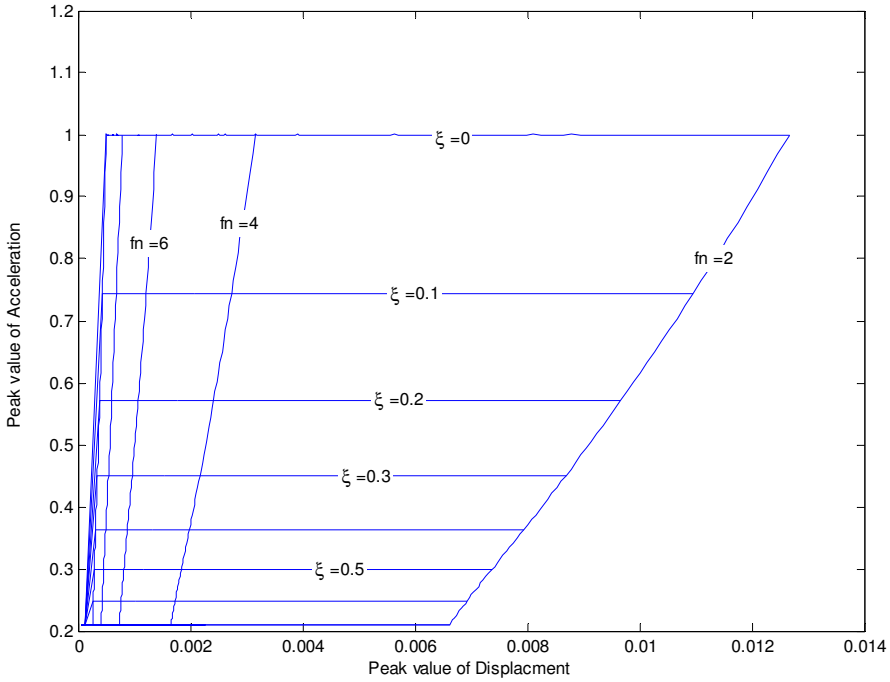

Figure 2-10: Peak value of mass acceleration versus peak value of displacement.

2.3.2.3 Pulse Force

To find the optimum curves for the pulse input, the same procedure as that of the pulse input in the base excitation case is followed. Similar to the base excitation optimization, the pulse duration is set at 50 *msec* again. The equations of the system, when the time is less than 50 *msec* are the same as (2.38) and (2.39). The new sets of equations should be derived and the initial conditions from the positive step should be considered as well. For the negative input, the displacement equation is derived as

$$x(t) = \frac{\sqrt{x_0^2\omega_n^2 + v_0^2}}{\omega_n} sin(\omega_n t + \theta), \qquad (2.40)$$

where

$$\theta = tan^{-1}(x_0 \omega_n / v_0) . \qquad (2.41)$$

The acceleration equation is also obtained by taking the second derivative of the displacement equation in (2.40). Therefore,

$$a(t) = -\omega_n \sqrt{x_0^2 \omega_n^2 + v_0^2} \; sin(\omega_n t + \theta) . \qquad (2.42)$$

Figure 2-11 illustrates the trade off between the peak amplitudes of the acceleration and the displacement. From the graphs for each damping ratio, there is a natural frequency which creates the maximum peak of the acceleration. In general, this frequency is approximately 7 to 10 *Hz*. The line of maxima is represented by the bold line.

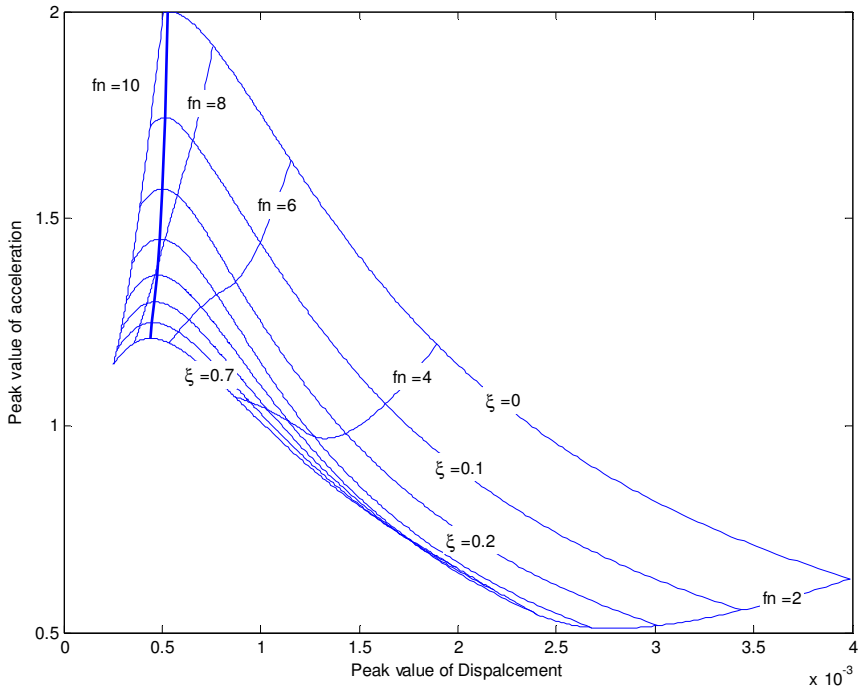

Figure 2-11: Peak value of the mass acceleration versus the peak value of the relative displacement.

2.4 Summary

In this chapter, the time and frequency optimization of a passive mount is discussed for base excitation and force excitation. The peak of the absolute acceleration and the peak value of displacement are chosen as the optimization parameters. The base excitation and force excitation are studied separately. Although, a comparison of the optimization results for the time and frequency cases may not be appropriate, it does indicate that the optimal mount parameters for these approaches are not an exact match. Hence, it is concluded that no passive mount is adequate to deal with all application specifications and isolation criteria. Although, the design of a passive isolator based on the RMS method might not be satisfactory for all cases, typically its application compared to the time optimization results, is recommended. Furthermore, this recommendation is supported by realizing that the RMS method can also be considered as an averaging method.

For the engine mounts and bushings which are usually designed for general isolating applications, a time optimization is not recommended because of inconsistency in the suggested optimum parameters. To design passive parameters in engine mounts, as indicated in Section 2.2, the RMS method can be utilized successfully. This method can be combined with the appropriate weighting factors for the worst cases or the usual ones. To overcome the shortcomings of the RMS method, a good control strategy can be developed according to the time response optimization results.

Chapter 3:Conventional Hydraulic Bushings

In the previous chapter, the optimization of the stiffness and damping parameters for a passive elastomer (rubber) isolator is discussed. Finding optimum parameters is vital for designing an engine mount and bushing, since all sorts of engine isolators (rubber or hydraulic) have passive elastomeric components to support static loads. In this chapter, the structure, components, and dynamic characteristics of a conventional hydraulic bushing are investigated.

3.1 Mathematical Modeling

A hydraulic bushing is a more developed version of the old rubber elastomer engine isolator. Hydraulic bushings and mounts are widely used in the automobile industry to isolate the engine and the chassis vibrations. The simplicity, low cost and dual frequency response of such bushings justify their industrial popularity. Moreover, the utilization of hydraulic bushings in low cost vehicles enhances the ride comfort.

The components of a common hydraulic bushing are described in section 1.3. it is also explained that the rubber stiffness and damping are selected passively to support the engine static load. When a hydraulic bushing system is subjected to a disturbance (from the engine or base), the extra mechanical load causes the fluid pressure inside the pumping chamber to rise. Consequently, the increased pressure in the pumping chamber results in the expansion of this chamber. In addition to this, some of the fluid in the pumping chamber is pumped to the compliance chambers. Since the fluid moves through

the inertia track, there is some loss of energy due to the friction, and, as a result, the mechanical energy dissipates gradually.

A simple lumped model of a hydraulic bushing, similar to the Cooper Standard bushing model 90576090 in Figure 3-1, is illustrated in Figure 3-2. Here, m is the engine unbalance mass, e is the equivalent eccentricity of the unbalance, ω_{dr} is the engine or driving frequency, A_p is the effective pumping area of the bushing, A_i is the inertia track cross-sectional area, C_1 is the pumping chamber compliance, C_2 is the secondary compliance chamber, and K_r and B_r are the rubber stiffness and damping, respectively.

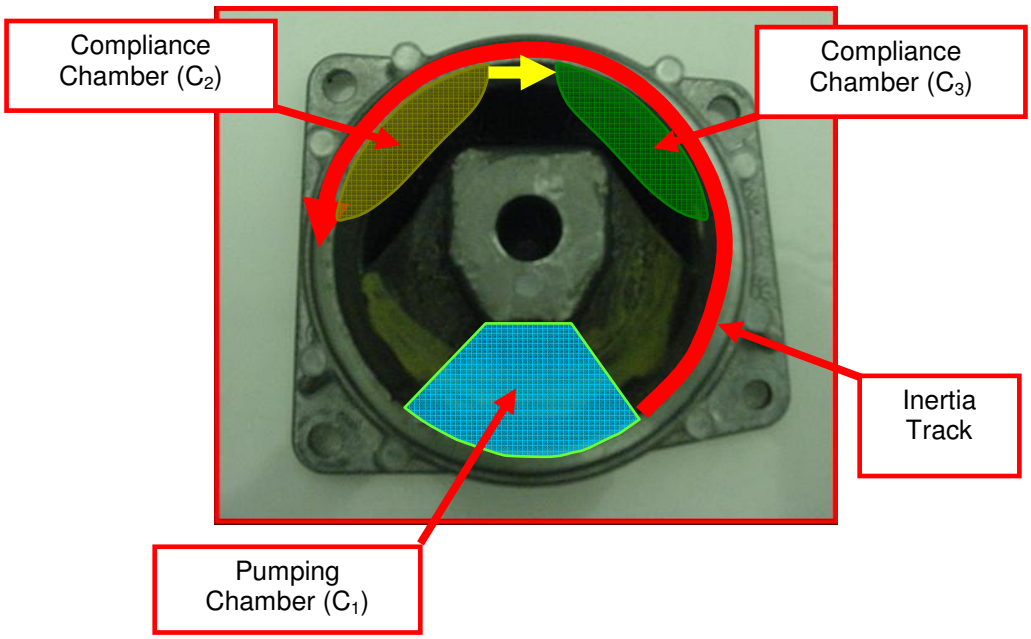

Figure 3-1: Photograph of the hydraulic Cooper Standard bushing P/N 90575028

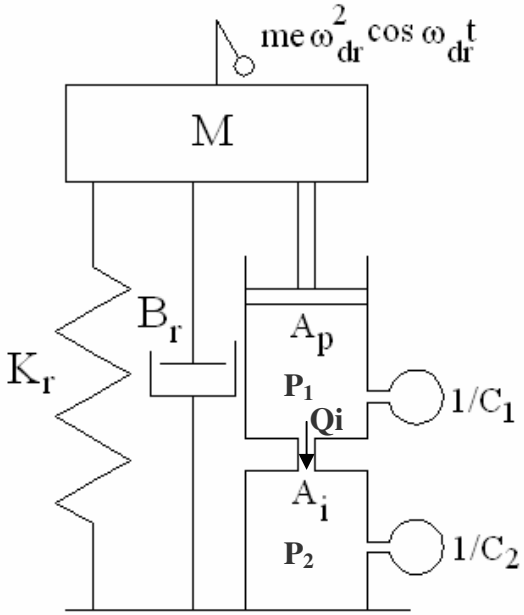

Figure 3-2: Lumped model of a hydraulic bushing

In the proposed lumped model, the damping and stiffness of the rubber entails a physical spring and damper. The internal hydraulic parts of the bushing are modeled as two cylinders with two accumulators, connected to the upper and lower cylinders, representing the pumping and second chamber compliances. The cylinders are connected to each other by a pipe that acts as an inertia track. The bushing continuity conditions are written as

$$C_1\dot{P}_1 = A_p\dot{X} - Q_i\,, \qquad (3.1)$$

$$C_2\dot{P}_2 = Q_i\,, \qquad (3.2)$$

and

$$P_1 - P_2 = I_i\dot{Q}_i + R_iQ_i\,, \qquad (3.3)$$

where

$R_i = \frac{b_i}{A_i^2}$, $C_1 = \frac{A_p^2}{k_1}$, $C_2 = \frac{A_p^2}{k_2}$, $I_i = \frac{M_i}{A_i^2}$, and $Q_i = A_i \dot{x}_i$.

It should be mentioned here that for simplicity, the flow through the inertia track is assumed to be laminar. It is also assumed that the bushing stiffness and damping are linear. One way of solving the three coupled linear differential equations is to convert them to the Laplace domain and solve the resulting three algebraic equations, respectively, as follows:

$$Q(s) = \frac{A_p S X(s)}{C_1 (I_i S^2 + R_i S + C)}, \tag{3.4}$$

$$P_1(s) = \frac{A_p X(s)(I_i C_2 S^2 + R_i C_2 S + 1)}{C_1 C_2 (I_i S^2 + R_i S + C)}, \tag{3.5}$$

and

$$P_2(s) = \frac{A_p X(s)}{C_1 C_2 (I_i S^2 + R_i S + C)}. \tag{3.6}$$

The net force transmitted to the base is

$$F_T = K_r X + B_r \dot{X} + A_p P_1. \tag{3.7}$$

substituting (3.5) in(3.7) ,

$$F_T(s) = (K_r + B_r s + \frac{A_p^2}{C_1} \frac{I_i s^2 + R_i s + 1/C_2}{I_i s^2 + R_i s + 1/C_1 + 1/C_2}) X(s), \tag{3.8}$$

Thus, the dynamic stiffness equation becomes

$$K_{dyn} = \frac{F_T(s)}{X(s)} = K_r + B_r s + \frac{A_p^2}{C_1} \frac{I_i s^2 + R_i s + 1/C_2}{I_i s^2 + R_i s + 1/C_1 + 1/C_2}. \tag{3.9}$$

In a typical hydraulic bushing, the rubber damping is too small, and affects the high frequency response of the hydraulic bushing. Therefore, since only the frequency region between 1-200 *Hz* is studied in this thesis, it is advantageous to ignore the rubber damping in the dynamic stiffness equations. Eq (3.9) conveys that the hydraulic bushing consists of two springs. One of the springs, the rubber passive stiffness K_r, has a constant stiffness. The other spring, the hydraulic term, is a frequency dependent spring. In the hydraulic part of the equation and at low frequencies ($s \to 0$), the stiffness is approximately A_p^2 / C_2, and at high frequencies ($s \to \infty$), the stiffness approaches A_p^2 / C_1. Since $C_1 << C_2$, the low frequency response of the hydraulic term in (3.9) results in a soft spring, whereas the high frequency regions exhibit a stiffer spring. According to (3.9), the switch between the soft and stiff regions occurs at

$$\omega_{r1} \simeq \sqrt{1/I_2 C_2} \qquad (3.10)$$

and

$$\omega_{r2} \simeq \sqrt{1/I_2 C_1}\,. \qquad (3.11)$$

In other words, the hydraulic bushing is a soft spring to ω_{r1}, passes a transient response at frequencies between ω_{r1} - ω_{r2}, and finally, at ω_{r2}, is a hard bushing.

3.2 Experimental Verification

An experimental test bed is developed to verify the mathematical modeling and to study the effect of each parameter variation on the hydraulic bushing's dynamic stiffness response. A magnetic shaker was used to validate the mathematical model on the existing Cooper Standard bushing. To change the bushing parameters such as the inertia track

size and resistance, the rubber component of the bushing is removed from its cast bracket and a new aluminum bracket is designed and fabricated to enable full control of the parameter variations. A schematic view of the bushing and its new bracket is in Figure 3-3 and Figure 3-4. In this setup, the original inertia track of the bushing is blocked from the inside. Pumping chamber C_1 is connected to the compliance chamber C_2 by a long narrow hose that behaves as an external inertia track of the bushing. In addition, a manual flow control valve is placed on the external inertia track to render its resistance controllable. A manifold is fabricated to distribute the fluid flow from the pumping chamber to the compliance chamber, Furthermore, to create an additional compliance chamber to study the effects of changing the compliance, the canal between chambers C_2 and C_3 is blocked from the inside. Since, in practice, chambers C_2 and C_3 are considered as a lumped compliance, this change does not alter the mathematical model and the general form of the solution.

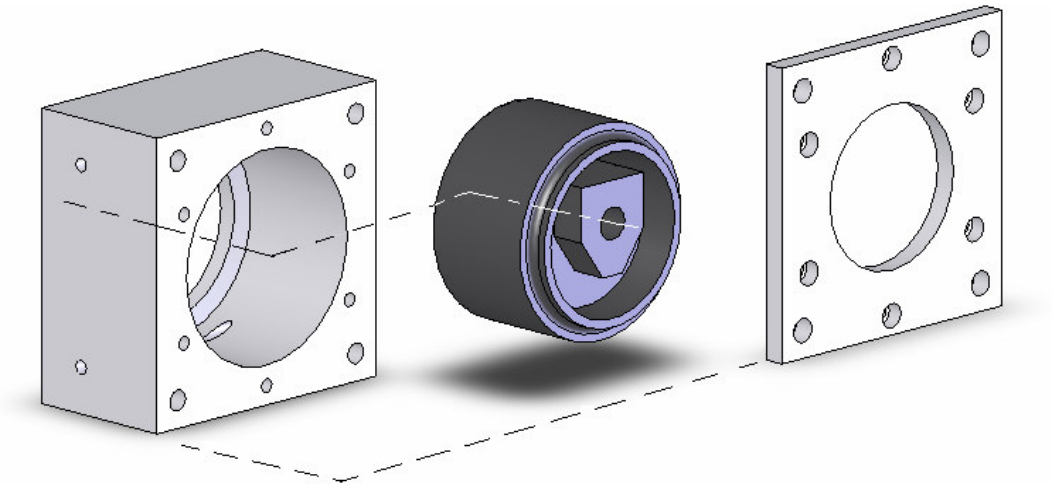

Figure 3-3: Bushing preparation for the experiment

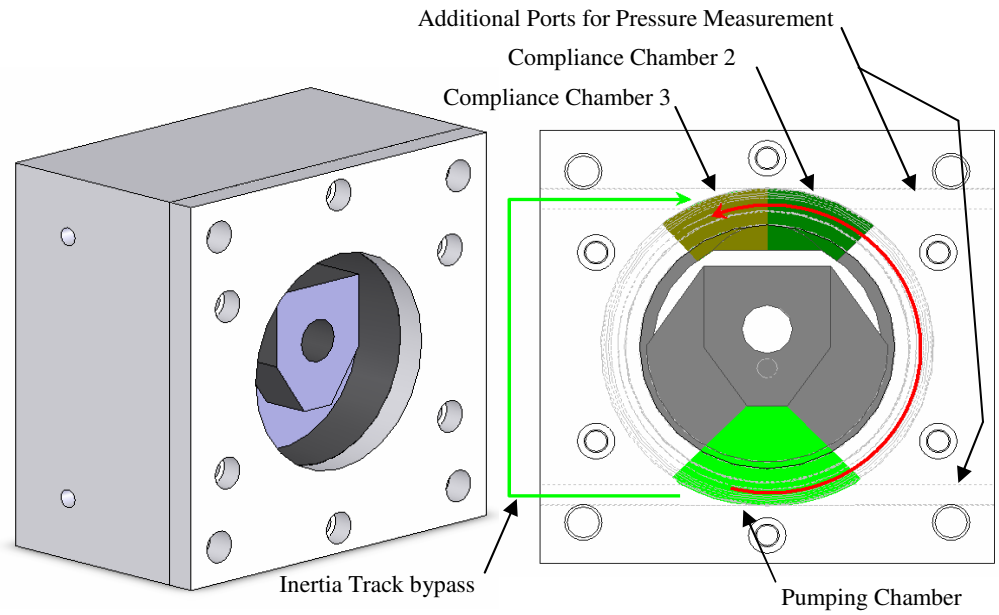

Figure 3-4: Bushing assembly and the schematic view of the chambers connections

Then, the new bracket is then installed on the shaker. A rod passing through the bushing's center hole is used to connect the bushing to a load cell for measuring the force transmitted from the shaker to the fixed frame. Here, the shaker acts as the engine and the fixed frame represents the chassis frame. The force transmitted through the mount is measured by a Sensotec Model 41, 1000 lb precision pancake load cell. The displacement of the bushing, with respect to the fixed frame, is measured by a string potentiometer SpaceAge Control, Model 173. A pressure transducer, model PX4000C6, OMEGADYNE, is adopted to trace the pressure variation inside the chambers. To carry out the experiment, a sweep sine input is applied to the bushing through the magnetic shaker. An LDS V722 shaker is used to generate the vibrations, which is controlled by the acceleration feedback via the Dactron SpectraBook and Dactron Shaker Control software. The shaker is capable of delivering 951 m/s^2 of acceleration from 5 to 4000 Hz. Dytran accelerometers, Model 3145AG LIVM, are also used as a feedback signal

generator to the shaker controller. Figure 3-5 and Figure 3-6 relay the details of the experimental setup.

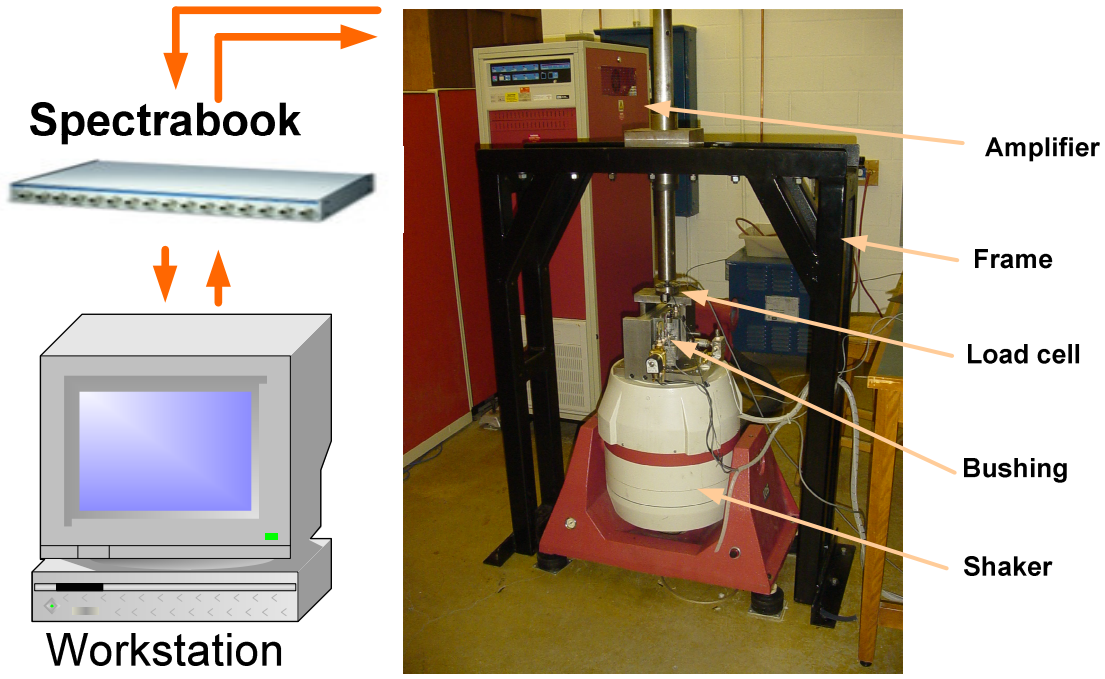

Figure 3-5: Experimental test bed with the data acquisition unit

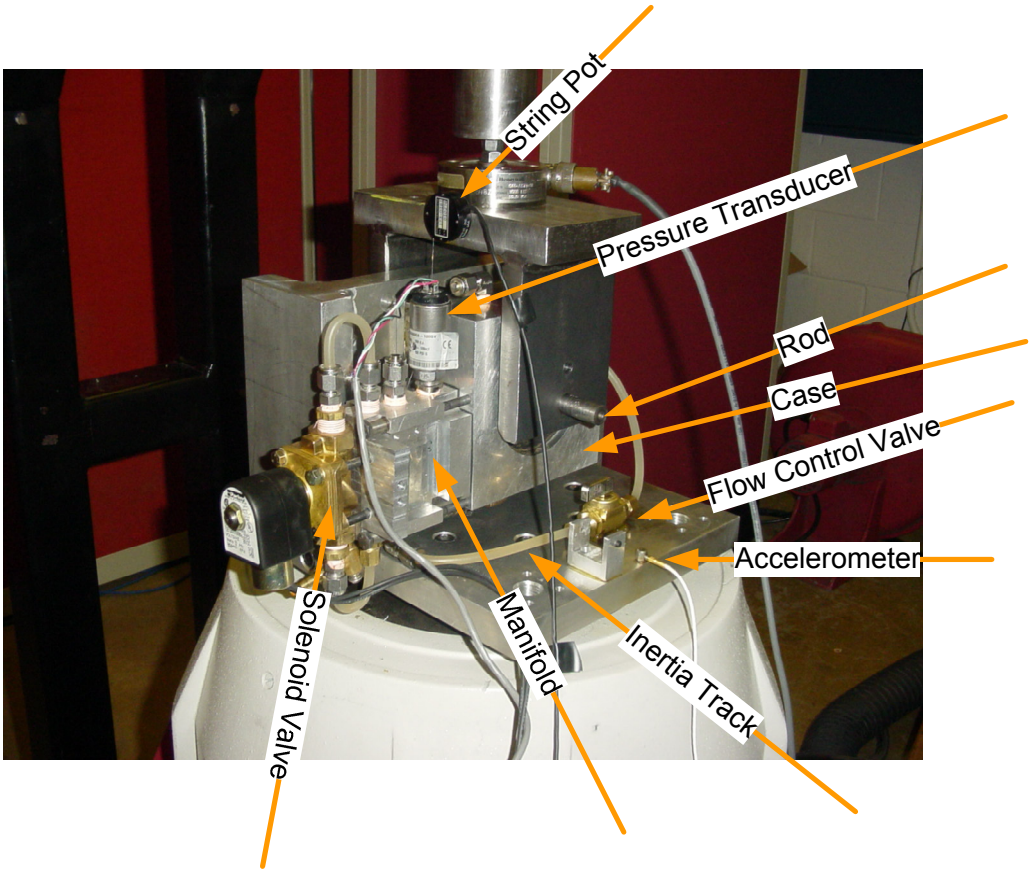

Figure 3-6: Dynamic stiffness fixture and bushing mounted on the LDS V722 shaker

The experimental dynamic stiffness response of the bushing is plotted in Figure 3-7 and Figure 3-8. The shape of the dynamic stiffness experimental results suggests that the hydraulic bushing is a second order system which confirms the mathematical model in (3.9). The dynamic stiffness response begins as a soft isolator at frequencies below 6 *Hz*, the transient response takes place at frequencies between 6-10 *Hz*, and finally the bushing is regarded as a hard isolator for the frequencies above 10 *Hz*.

Investigating the phase response of the hydraulic bushing is another way to validate (3.9). The dynamic stiffness equation is composed of two quadratic functions in the numerator and denominator, respectively, each corresponding to a 180° phase shift. The only difference is that the quadratic function in the numerator causes a positive 180°

phase shift whereas the one in the denominator corresponds to a negative 180° phase shift. Since the notch frequency of the numerator is less than the one in the denominator, it is expected that the positive phase shift happens first. However, if the second notch is close enough to the first one, the 180° phase shift is never completed. Thus, the positive and negative phase shifts cancel out and a phase bump is created. The amplitude of the phase shift at the bump depends on the damping factor of the quadratic functions. The phase shift response in Figure 3-8 confirms these statements.

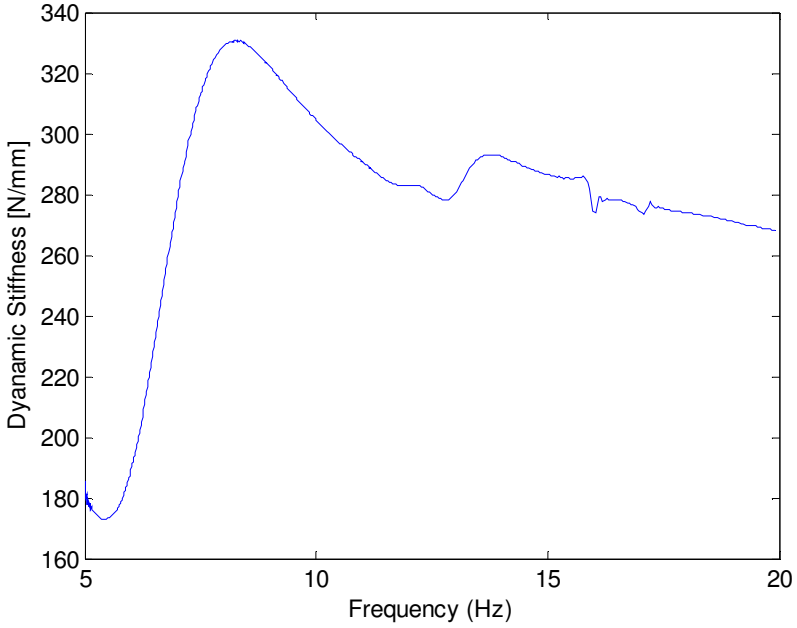

Figure 3-7: Dynamic stiffness response of the hydraulic bushing

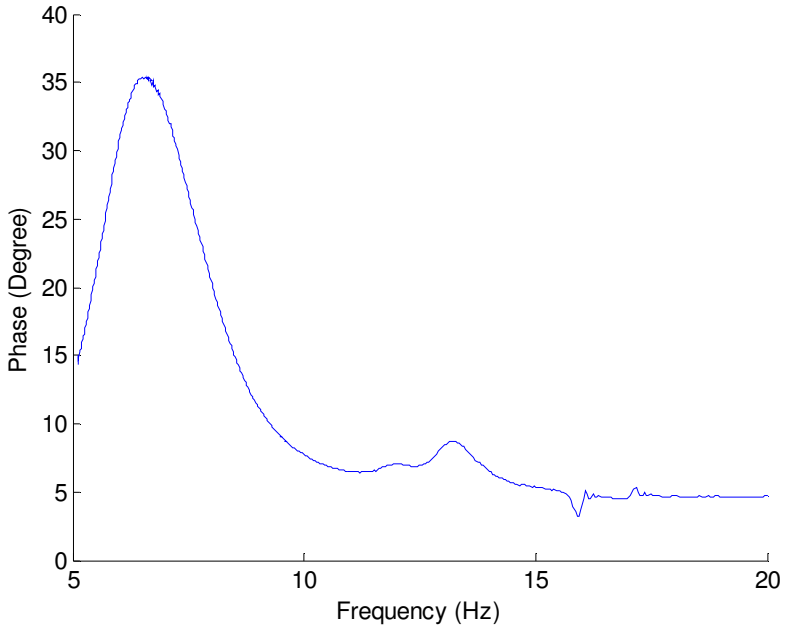

Figure 3-8: Phase change of the hydraulic bushing

3.3 System Identification

For the mathematical model of the bushing, a curve is fitted to the experimental data to find the coefficients of the dynamic stiffness equation. For this purpose, the lsqcurvefit function in Matlab® is used. This Matlab function solves nonlinear curve-fitting (data-fitting) problems by the least-squares method; given input data, and the measured output, the function finds the coefficients that best fit the equation. Obviously, an estimation of the initial value of the coefficients is essential for a better system identification. The length of the external inertia track and the viscosity of the liquid inside the bushing (water) determine a reasonable initial value of the inertia track size. The dependency of the locations of the notch frequencies on the compliances of the chambers is then used to estimate the initial values of the compliances in the dynamic stiffness equation. Figure 3-9 illustrates the experimental curve and the fitted one.

® Matlab is the registered trademark of MathWorks Inc.

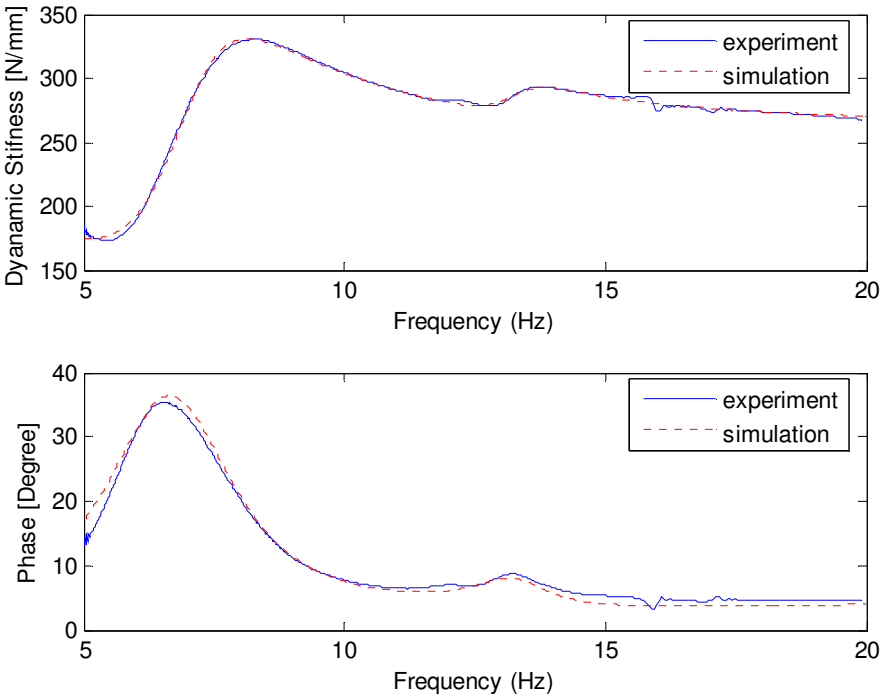

Figure 3-9: Curve fitting the experimental data to identify the bushing parameters

It should be noted that the second peak in the dynamic stiffness curve (at approximately 13 and 13.5 Hz) is the structural vibration response. The peak occurs because the frame which holds the bushing case is not rigid enough and begins to vibrate in the frequency region in Figure 3-9. Since this disturbing response is constant, the response's transfer function is derived by a similar curve fitting method, and added to the dynamic stiffness equation. This facilitates a comparison between the experimental and the simulation results. The values of the different coefficients in the dynamic stiffness in (3.9) are tabulated in Table 3-1.

Table 3-1: Nominal hydraulic bushing parameter values

Symbol	Value	Unit
A_p	15.27	mm^2
B_r	0.1398	N-s/mm

K_r	195.14	N/mm
C_1	3.8933	N/mm^5
C_2	291.31	N/mm^5
I_2	1.2497e-004	$N\text{-}s^2/mm^5$
R_2	0.0022	$N\text{-}s/mm^5$

It is evident that the principal characteristic of the hydraulic bushing is its dynamic stiffness curve which starts with a small value at low frequencies and gradually increases as the frequencies increase. According to (3.7), the transmitted force has a relation with the stiffness and damping of the rubber bushing, as well as the pressure in the pumping chamber. The stiffness and damping of the bushing are supposedly constants and are designed passively. The only frequency dependent part of the equation is the pressure in the pumping chamber which from (3.1) is a function of the compliance and the amount of the fluid accumulated in the chamber. Although the rubber compliance is not a linear parameter, for very small deflections (0.1 mm), it is assumed to be constant. As a result the dependency of the accumulated fluid in the pumping chamber on the frequency makes the pressure in that chamber a function of the frequency. Therefore, to further investigate on the dependency of the pressure on the excitation frequency, the volumetric flow (the amount of fluid in the chamber) in the pumping chamber is simulated.

For the lumped model in Figure 3-2 , the amount of fluid accumulating in the pumping chamber is equal to the difference between the pumping rate and the fluid volume moving to the compliance chamber. Since the compliance of the compliance

chamber is higher than that of the pumping chamber, the fluid tends to travel into the compliance chambers. Although this is a fact in static situations, it is not always correct for frequency dependent problems. In fact, for the fluid to accumulate in the compliance chambers, it should move through the inertia track. Depending on the size of the inertia track and the compliance of the compliance chambers, it takes some time for the fluid to move through the inertia track and accumulate in the compliance chambers. Thus, the migration of the fluid to the compliance chambers can only occur for the excitations that are happening slow enough (low frequencies) to give the fluid time to travel along the inertia track, That is, for the excitations to happen faster than the time constant (high frequencies), the compliance chambers became ineffective, and as a result, all the pressurized fluid accumulates in the pumping chamber.

The application of these statements to the dynamic stiffness response, it indicates why the dual frequency response characteristic occurs. In reality, the high flexibility of the compliance chambers causes the fluid to accumulate in them at low frequencies. Consequently, the pressure in the pumping chamber drops, reducing the force transmitted to the frame. Contrarily, at high frequencies, the compliance chambers are ineffective. Therefore, as the excitation frequency increases, the pressure inside the pumping chamber increases and the bushing becomes stiffer.

If the values in Table 3-1 are substituted into (3.10), ω_{r1} is 0.8 Hz. This frequency defines the excitation frequency at which the compliance chambers have the maximum effect regarding the amount of the fluid in the pumping chamber, causing the pressure drop in that chamber. Figure 3-10 plots the fluid accumulated in both the pumping and compliance chambers at 1 *Hz*. Here, the net pumped fluid is represented by *Q*. The

volume of the fluid accumulated in the pumping and compliance chambers is Q_1 and Q_2, respectively. Since it takes time for the compliance chamber to fill with fluid, at the beginning, most of the pumped fluid is pressurized in the pumping chamber. However, as time goes on, the connection between the compliance chamber and pumping chamber is established and only a small amount of the fluid accumulates in the pumping chamber. From the simulations, it is observed that, at this frequency, the phase of the pumped fluid is very close to the phase of the accumulated fluid in the compliance chamber. Since the pumping chamber pressure is reduced, it is expected that, at this frequency, the bushing exhibits its lowest dynamic stiffness. The experimental results in Figure 3-7 confirm this.

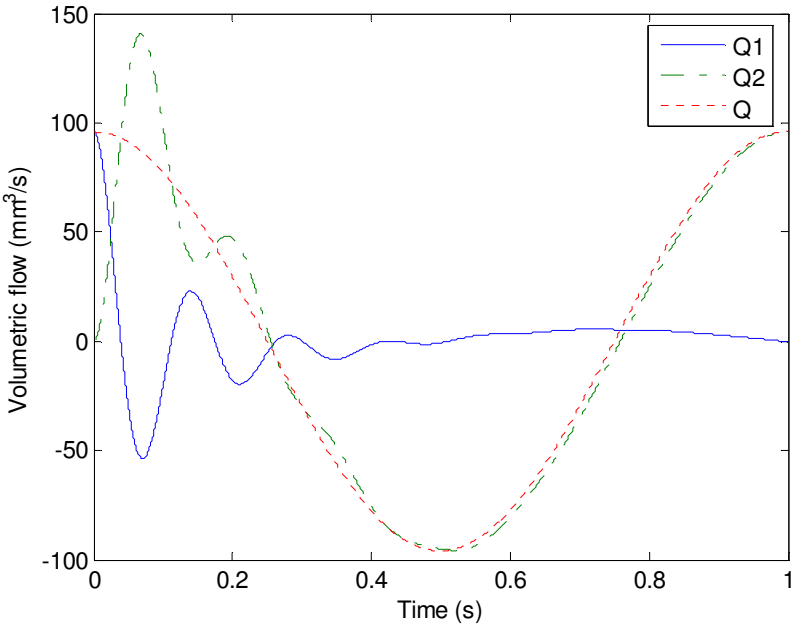

Figure 3-10: Time response of the volumetric flow in the linear model of the hydraulic bushing at 1 *Hz*

As the frequency increases, the bushing behaviour gradually changes. Figure 3-11 represents the fluid volume in the different chambers at 4 *Hz*. At this frequency, the compliance chambers are still effective. However, there is not enough time for all the

fluid to move through the inertia track, more fluid accumulates in the pumping chamber. This increase results an increase in the pressure inside the pumping chamber, and consequently, an increase in the dynamic stiffness response. It is noteworthy that the excitation phase is progressively shifted toward the pumping chamber's accumulated fluid.

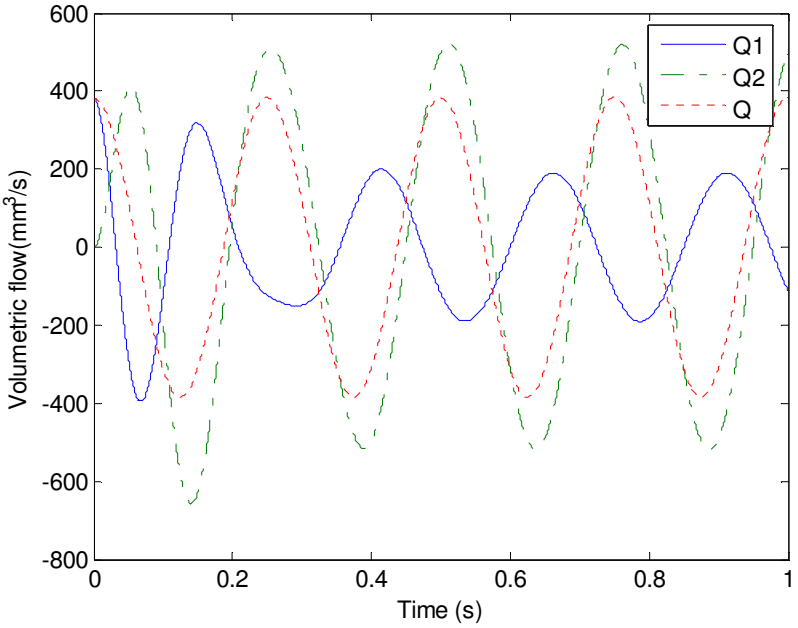

Figure 3-11: Time response of the volumetric flow in the linear model of the hydraulic bushing at 4 *Hz*

At 8 *Hz*, the fluid accumulated in the pumping chamber increases dramatically. This frequency corresponds to ω_{r_2}. Consequently, the pressure inside the pumping chamber indicates a jump. Figure 3-12 denotes the simulation results. The phase of the pumped fluid and that of the accumulated fluid in the pumping chamber are closer at this frequency. It is remarkable that the amplitudes of the fluid accumulated in the compliance and pumping chambers, are higher than the amplitude of the pumped fluid. This is due to the phase difference between the accumulated fluid in the pumping and compliance

chambers. In other words, when the pumping chamber begins to expand, the compliance chambers begin to retract. This causes more fluid to accumulate in the pumping chamber than the amount pumped to it. The same thing occurs during the compliance chamber expansion, causing the amount of the accumulated fluid in that chamber to increase even more than the pumped fluid.

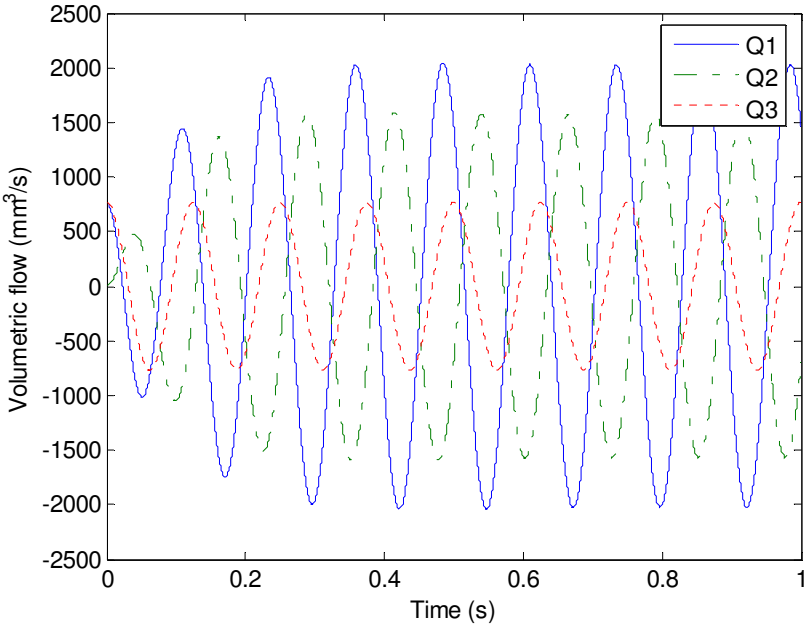

Figure 3-12: Time response of the volumetric flow in the linear model of the hydraulic bushing at 8 *Hz*

Figure 3-13 reflects the simulation results at 15 Hz. At high frequencies, as predicted, the compliance chambers become ineffective. All of the pumped fluid is accumulates in the pumping chamber. Thus, the pressure inside the pumping chamber is changed only linearly by the excitation frequency.

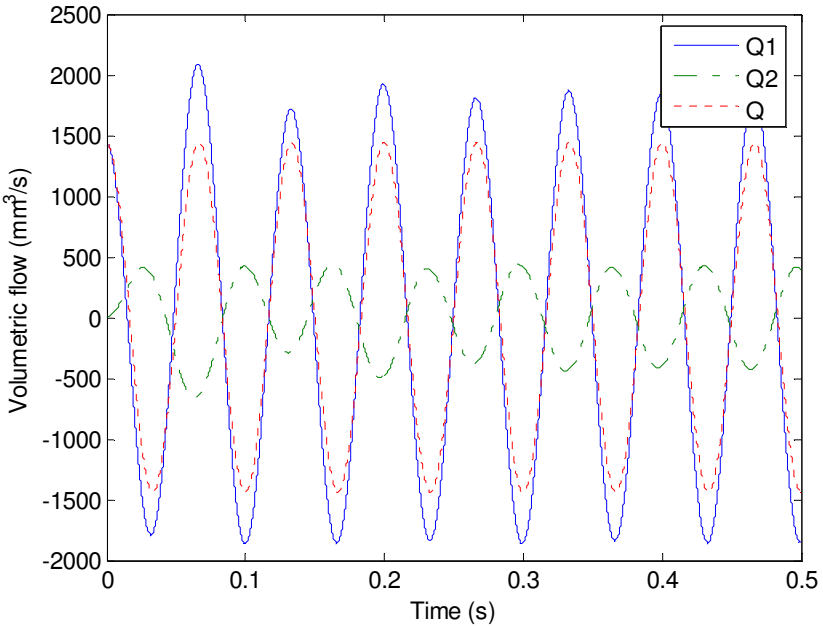

Figure 3-13: Time response of the volumetric flow in the linear model of the hydraulic bushing at 15 *Hz*

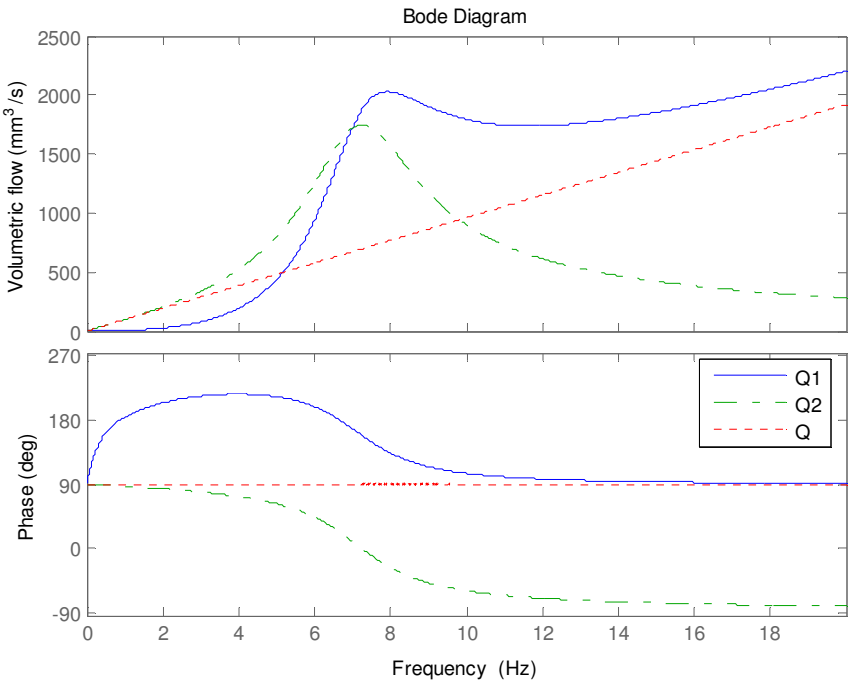

Figure 3-14: Frequency response of the volumetric flow in the linear model of the hydraulic bushing

Figure 3-14 portrays the frequency response of the volumetric flow in the pumping and compliance chambers. At low frequencies, most of the pumped fluid is

moving to the compliance chambers. Gradually, due to the frequency increase and the phase difference, both the pumping and compliance chambers contribute to the amount of accumulated fluid of the other chamber; That is, each chamber is an additional fluid source for the other. 8 *Hz* is the resonance frequency of the combination of the compliances and the inertia track. Beyond this frequency, due to the high excitation speed (high frequency), the inertia track loses its effectiveness. Thus, all the pumped fluid accumulates in the pumping chamber. The pressure frequency responses of both the pumping and compliance chambers are displayed in Figure 3-15. The dependency of the pressure on the volumetric flow can be observed by comparing Figure 3-14 to Figure 3-15.

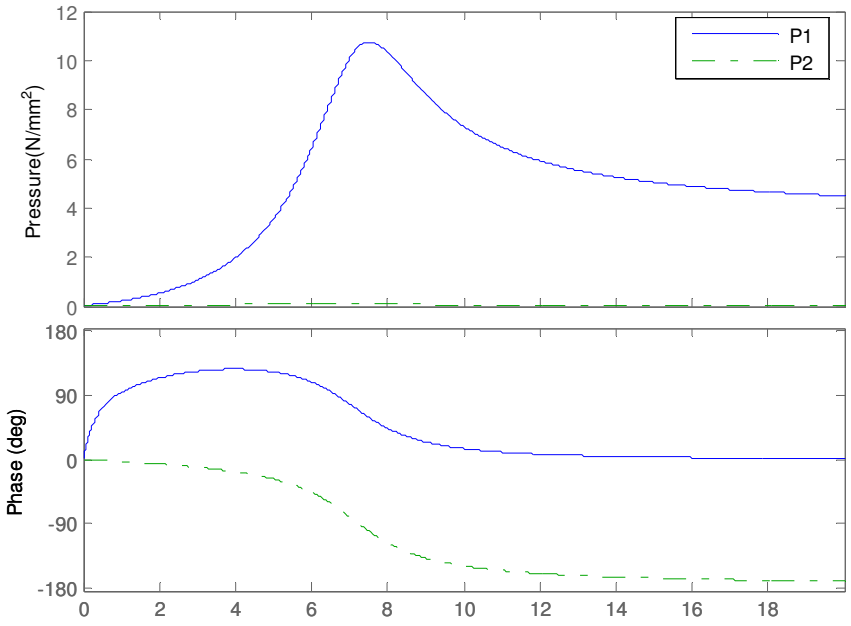

Figure 3-15: Frequency response of the pressure in the linear model of the hydraulic bushing

3.4 Summary

The structure and components of conventional hydraulic bushings are now identified to facilitate the development of a new, simple mathematical model. This model is proposed based on the behavior of the hydraulic bushing components (for instance; the compliance chamber expansion and inertia track energy dissipation) and structural relations. After Experimental validation of the linear model, various coefficient of the model are evaluated by curve fitting.

Chapter 4: Inertia Track Effect

As explained in the previous chapter, the inertia track is one of the parameters which define the soft and stiff frequency region of the hydraulic bushing according to the mathematical model developed in this thesis. In this chapter the effect of the inertia track on the dynamic stiffness response is discussed, paving the way to find a solution to the VDE isolation problem. From the various parameters, the inertia track is selected. Compared to the rubber compliance, effective pumping area and other effective factors in the dynamic stiffness equation, the inertia track is the easiest parameter to control, and is also based on the purposed mathematical model, the most effective one.

4.1 Inertia Track Resistance Effect

The energy dissipative parts (resistors) in mechanical vibrating systems behave as dampers in the simulations. In hydraulic bushings, the energy dissipation occurs in the inertia track. According to (3.9), inertia track resistant R appears as the coefficient of "s". According to the quadratic function frequency responses, the effect of the inertia track resistance on the peak location is negligible. However, similar to the quadratic function frequency responses, the inertia track resistance determines the amplitude of the peaks at the resonances.

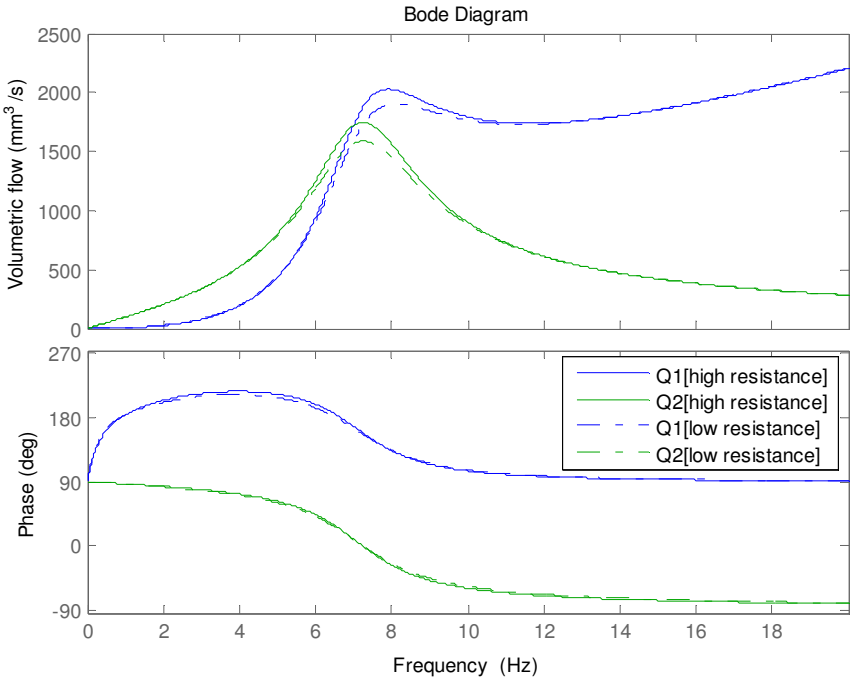

Figure 4-1: Effect of the inertia track resistance on the volumetric flow frequency response

The effect of the resistance on the dynamic stiffness can be stated differently. It is noted that the resistance of the inertia track is not high enough to block the track or obstruct the fluid passing through it at low frequencies and in the presence of an inertia track resistance, the fluid has enough time and energy to travel between the two chambers. Moreover, the volume of the fluid traveling between the pumping and the compliance chamber is not high enough for the inertia track to exhibit a major effect. Nevertheless, at the resonance frequency of 8 *Hz*, the volume of the fluid moveing through the inertia track increases considerably. As a result, the resistance demonstrates its effect. One interpretation of the effect of increasing the resistance in the inertia track is the increased pressure inside the pumping chamber. However, this interpretation is incorrect, since much of the flow to the pumping chamber at the resonance frequencies (which is the frequency that the resistance is most effective) is from the compliance

chambers. As a result, the high resistance reduces the amount of fluid traveling from the compliance chamber to the pumping chamber. Thus, as it is observed in Figure 4-2, the pressure drops in the pumping chamber at 8 *Hz*, by increasing the inertia track resistance.

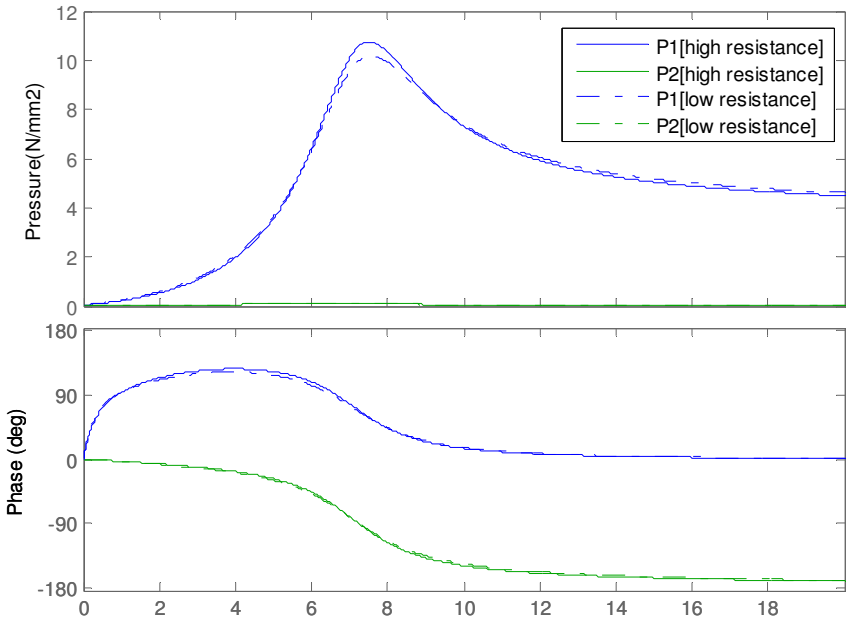

Figure 4-2: Effect of the inertia track resistance on the pressure frequency response

The dynamic stiffness simulation results for the different inertia track resistances, at R_2 = 0.0022 and 0.0025, are denoted in Figure 4-3 and Figure 4-4. Also, the structural vibration response is included in this simulation. As it is expected, the higher resistance results in lower peaks in the dynamic stiffness curve. Therefore, controlling the resistance of the inertia track does helps to change the damping and avoid the high amplitude peaks at the resonance frequencies.

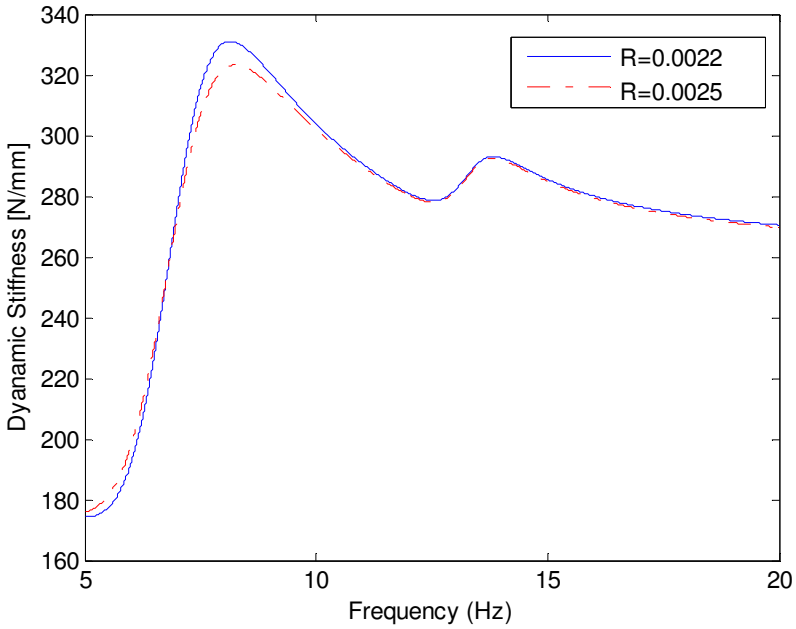

Figure 4-3: Dynamic stiffness frequency response amplitude for different inertia track resistances (simulation)

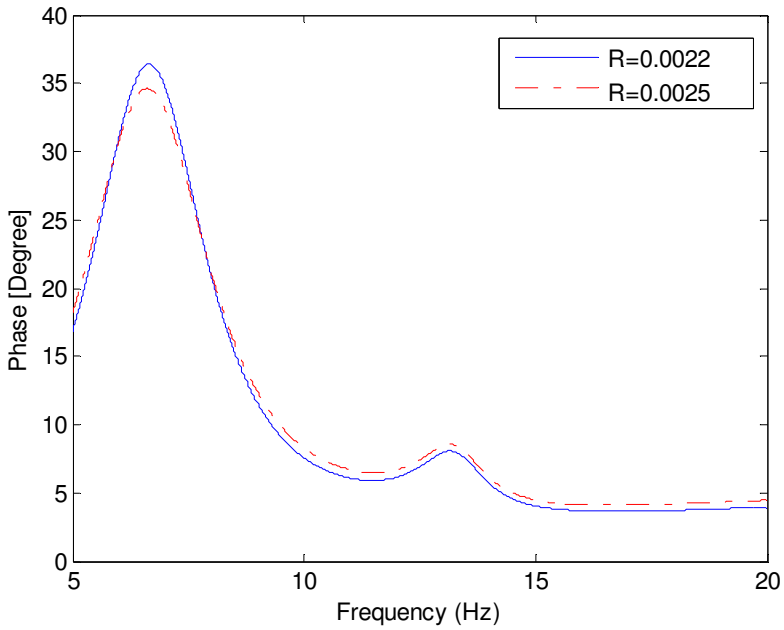

Figure 4-4: Dynamic stiffness frequency response phase for different inertia track resistances (simulation)

To investigate the effect of the resistance on the bushing response, an experiment is also performed. For changing the resistance of the inertia track, a butterfly valve is placed on the external inertia track. In the first experiment, the valve is fully open. Therefore, the inertia track demonstrates minimum resistance, and a high peak is expected in the response at the notch frequency. In the next experiment, the valve is half open. This matches the simulation results, when R=0.0025. As a result, a lower peak is observed at the notch frequencies of the bushing. The results of the experiment are exhibited in Figure 4-5 and Figure 4-6 .

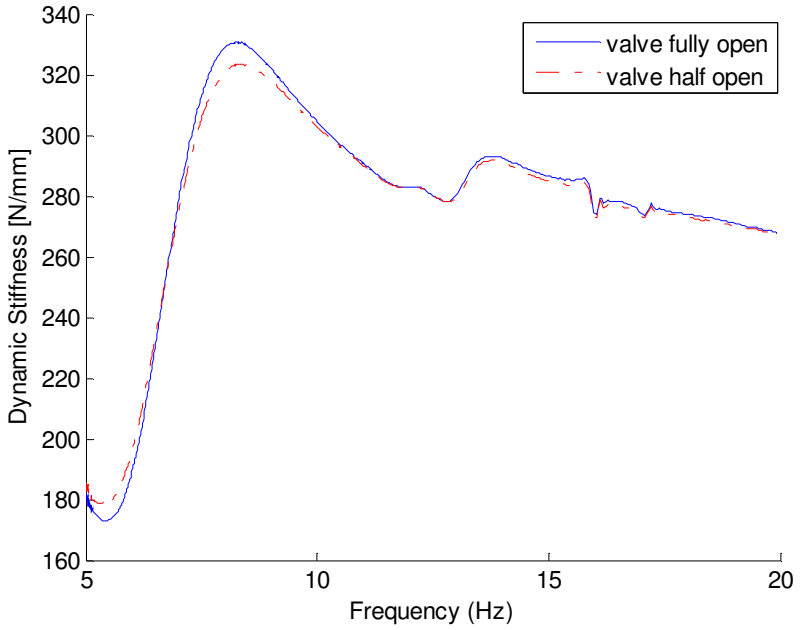

Figure 4-5: Dynamic stiffness frequency response amplitude for different inertia track resistances (experiment)

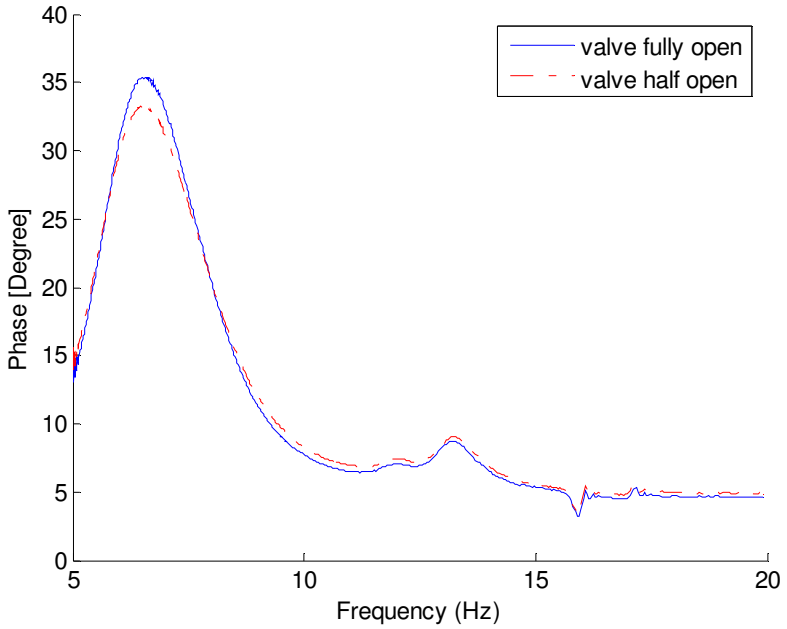

Figure 4-6: Dynamic stiffness frequency response phase for different inertia track resistances (experiment)

4.2 Inertia Track Size Effect

To study the effect of the inertia track size on the dynamic stiffness response, (3.10) and (3.11) are the two relations that should be investigated. From these equations, it is evident that the notch frequencies are proportional to $\sqrt{1/I_2}$. Thus, the inertia track can shift the notch frequencies to the left or right. In addition, the damping ratio of the system is proportional to I_2. As a result, any change of the inertia track size is reflected on the actual damping of the isolator.

Figure 4-7 illustrates the flow volume in the pumping and compliance chambers for two different cases. The solid curve is based on the values of Table 3-1, and the dashed curves belong to the same bushing with a larger inertia track. It can be seen from the simulations that the larger inertia track causes the peak of the flow volume to shift to

the left. This occurs because, in a long inertia track, it takes more time for the fluid to reach the compliance chamber than for a short inertia track. As a result, the response time increases. In other words, and the track can be effective only at slower excitations (lower frequencies). Moreover, the longer inertia track exhibits a higher resistance to the fluid which passes through it. Thus, as expected, the lower resonance peaks in the volumetric curves belong to the longer inertia track.

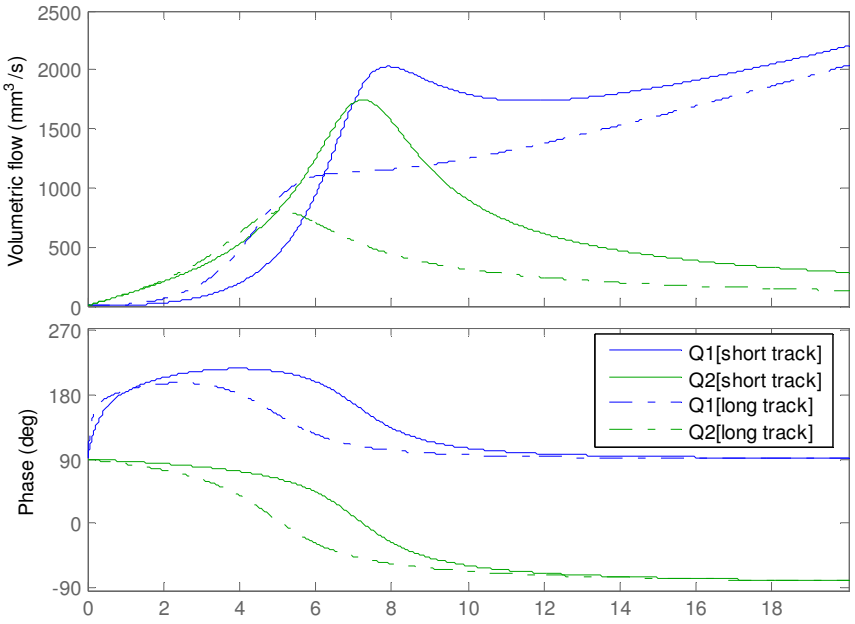

Figure 4-7: Effect of the inertia track size on the volumetric flow frequency response

The relation between the fluid volume accumulated in the chambers and their pressures is discussed in details in the previous chapter. Based on this knowledge, it can be concluded that any shift in the resonance frequencies of the transferred fluid volume in the chambers is reflected by the pressure curves, and consequently, the dynamic stiffness response of the bushing. Figure 4-8 plots the pressure curves in the pumping and compliance chambers. The dash lines denote the long inertia track simulation results, and

the solid curves represent the short inertia track case. As expected, the peak frequency in the long inertia track case moves to the left, in agreement with the volumetric flow curves.

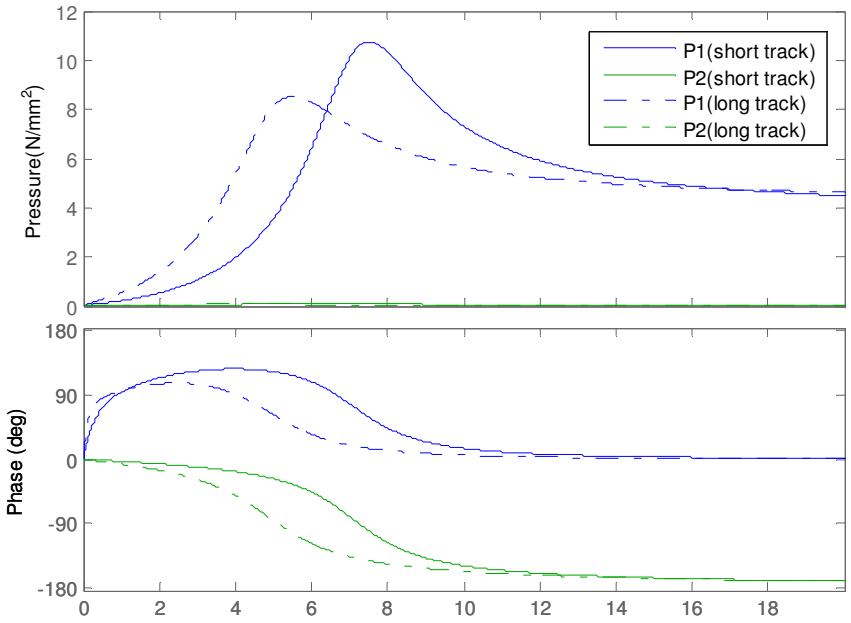

Figure 4-8: Effect of the inertia track size on the pressure frequency response

Figure 4-9 and Figure 4-10 exhibit the simulation results of the effect of the inertia size on the dynamic stiffness response. The first simulation is conducted with the values obtained from the curve fitting and system identification (solid curves). According to Table 3-1, the inertia track size of the bushing is $1.2497e^{-4}$ N-s^2/mm^5. The notch frequencies of the dynamic stiffness simulation of the whole system (not the hydraulic part alone) are 6 and 8 *Hz*. Increasing the inertia track size to $2.7828e^{-4}$ N-s^2/mm^5 should shift the notch frequencies to the left. Based on the mathematical model, the notch frequencies of the new system should now occur at 2 and 6 *Hz*.

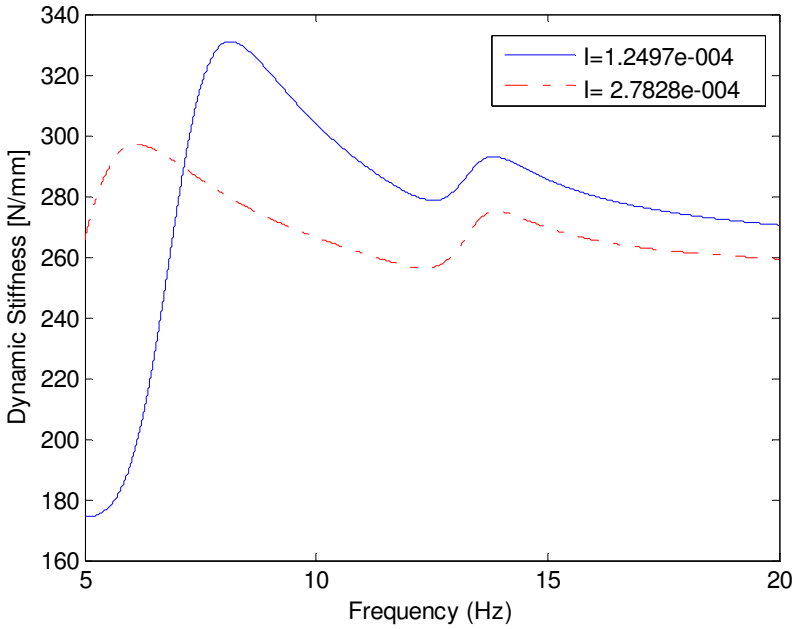

Figure 4-9: Dynamic stiffness frequency response amplitude for the different inertia track sizes (simulation)

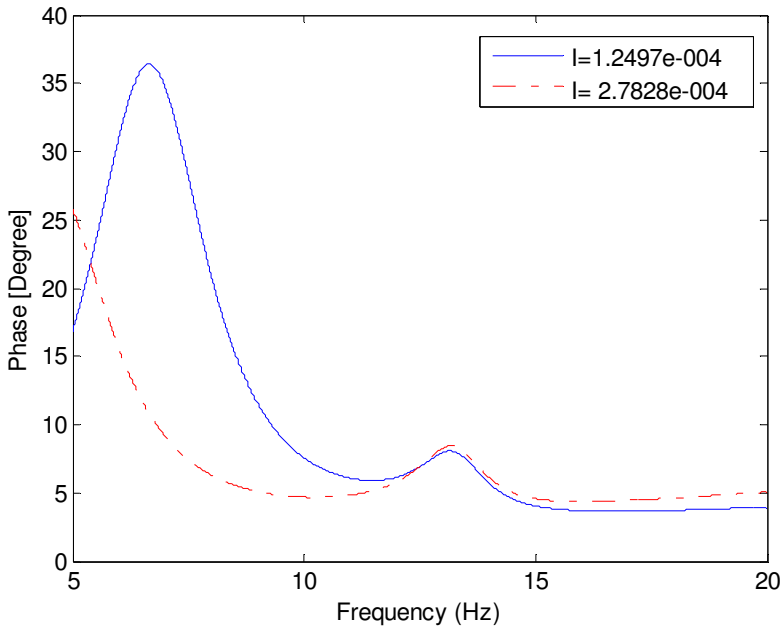

Figure 4-10: Dynamic stiffness frequency response phase for the different inertia track sizes (simulation)

To perform the experiment and investigate the effect of the inertia track on the dynamic stiffness response, the original external inertia track is replaced by a longer one. The sweep sine excitation is used in the experiments, and the results are signified in Figure 4-11 and Figure 4-12.

The experimental results show that the notch frequencies of the longer inertia track are moved to lower frequencies. Although the first notch frequency location can not be identified in this experiment (The shaker can not work for frequencies below 5 Hz), the trend of the curve suggests that it moved to the left. The second notch frequency location obviously shifts from 8 *Hz* to 6 *Hz*.

It should be noted that in addition to the shift in the notch frequencies, a lower peak amplitude can be identified in the dynamic stiffness response of the bushing with the longer inertia track. The peak of the long inertia track occurs at 300 *N/mm* whereas the short inertia track peak value is 330 *N/mm*.

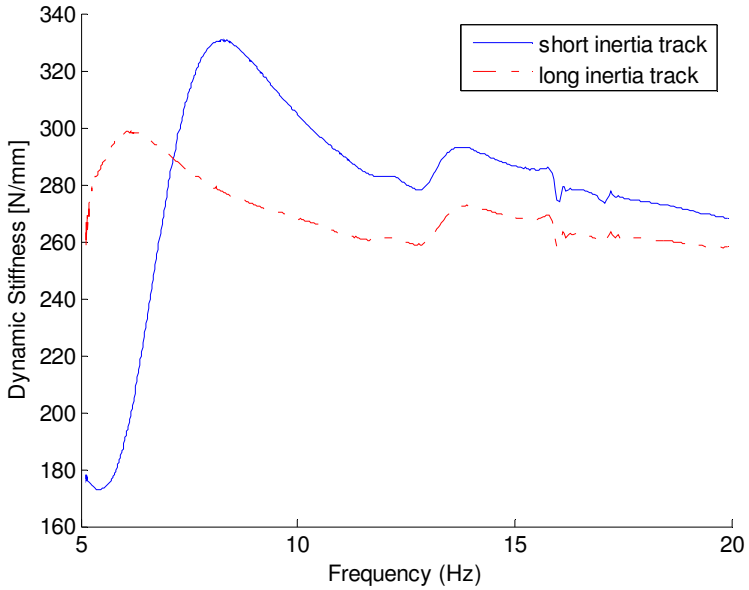

Figure 4-11: Dynamic stiffness frequency response amplitude for different inertia track sizes (experiment)

The phase frequency response can also be used to validate the inertia track size effect on the hydraulic bushing response. The bump in the phase response, due to the phase cancellation of the numerator and denominator in (3.9), moves to the left in Figure 4-11. It means that the notch frequency location moves to the left. The increase in the damping coefficient can also be interpreted from the bump amplitude. It can be easily proved that for the quadratic function phase cancellation in the numerator and denominator below 90°, the higher damping corresponds to the lower bumps in the phase response.

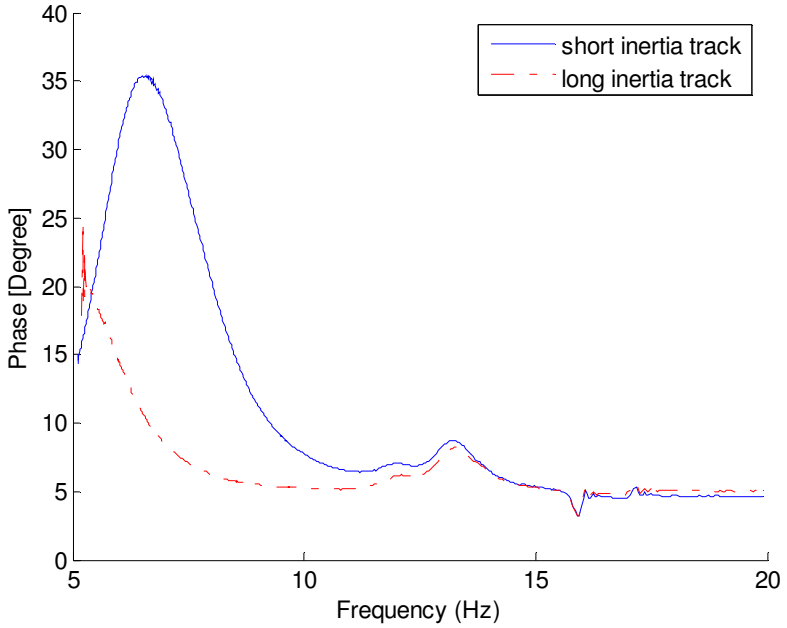

Figure 4-12: Dynamic stiffness frequency response phase for different inertia track sizes (experiment)

In practice, changing the inertia track size is achieved by different methods. The easiest solution might be to use different inertia tracks in the bushing and control them by on/off solenoid valves.

4.3 VDE Isolation Problem Solution

As stated in Chapter 1, an ideal isolator for the VDE isolation problem should be half as stiff in the operating frequency range of the cylinder deactivation mode. Yet in the normal mode the ideal isolator must have a performance similar to that of conventional hydraulic bushings. The challenge is to devise a system which can produce a curve similar to that in Figure 4-13; that is, the notch frequencies are shifted to the right in the engine deactivation mode (solid line) whereas the same dynamic performance of the conventional hydraulic bushings (dash line) is preserved. Such a system requires switching between the existing rubber part and a softer material or some sort of adjustment in the effective pumping area of the pumping chamber. Also, it might be possible to achieve such a curve by switching or activating a more compliant material with the existing pumping chamber compliance in the cylinder deactivation mode. All of these solutions are not applicable since they cost more, require design changes and may not even be feasible.

Regarding the mathematical model and experimental dynamic stiffness results, it is evident that the hydraulic bushing curves show a soft region at low frequencies, which gradually turns into a hard region at higher frequencies. Since the low and high dynamic stiffness values are functions of C_1 and C_2, the difference between the soft and hard bushings level of amplitude can be adjusted by an appropriate selection of the compliances of those chambers. Consequently, shifting the notch frequencies to the right for the cylinder deactivation mode is a solution to the VDE isolation problem. The preliminary simulation and the experimental data suggest that shifting the notch

frequencies to the right is achieved by a smaller inertia track size. In fact, by reducing the size of the inertia track, the compliance chamber's active frequency range increases.

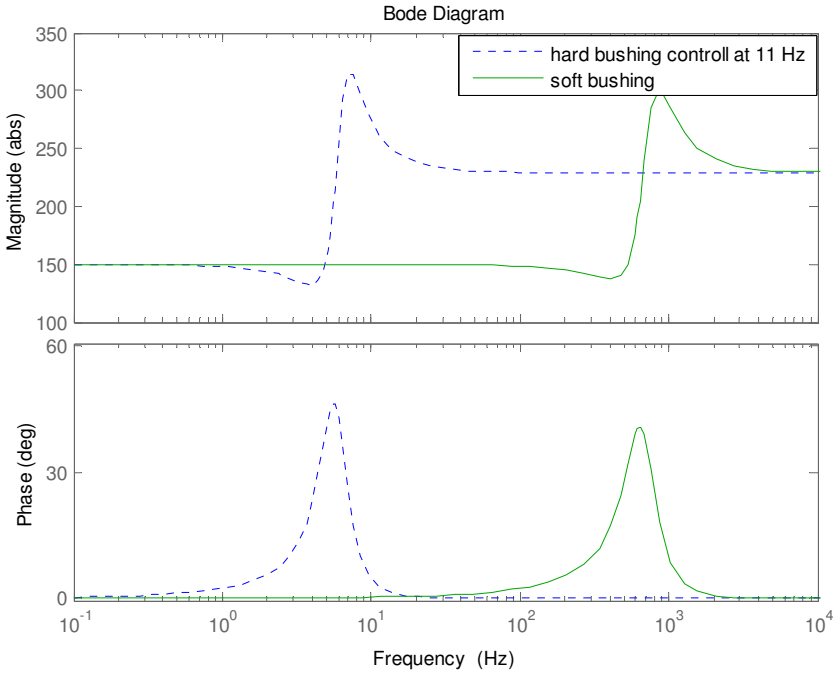

Figure 4-13: Ideal VDE isolator dynamic performance

The schematic view in Figure 4-14 and Figure 4-15 illustrates the experimental test bed which is specifically built to prove the concept of the solution proposed in this thesis for the VDE isolation problem. To achieve the short inertia track requirement, an external compliance chamber is designed. Similar to the internal compliance chambers of the hydraulic bushing, this new compliance chamber has a rubber diaphragm on the side. As a result, the pressurized water can change the volume of this external compliance chamber. To minimize the size of the inertia track, the chamber is designed narrow ($I=7.2158e^{-006}$ N-s^2/mm^5 which is 17 times smaller than the actual inertia track). This compliance chamber is then attached to the bushing. A long hose is used to connect the internal compliance chambers of the hydraulic bushing to the pumping chamber. The only problem with this experimental setup is that the short inertia track needs to be

blocked to obtain the dynamic stiffness curve for the stiff bushing (the normal bushing dynamic performance). The short inertia track inside the bushing aluminum block prevents the use of a valve for this purpose. As a result, an aluminum cap is fabricated to disable the rubber diaphragm, rendering the short inertia track inactive. The location of the cap on the manifold is shown in Figure 4-16.

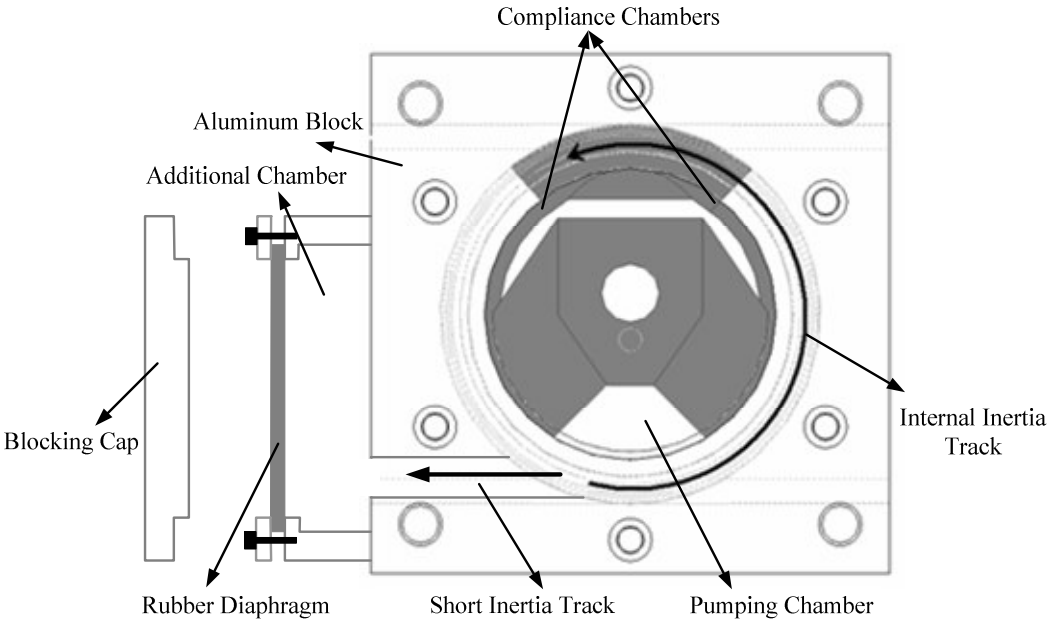

Figure 4-14: Short inertia track proof of the concept schematic view

The dynamic stiffness curves of the VDE are plotted in Figure 4-17. The dashed line curve is the dynamic stiffness curve of the actual bushing (the rubber diaphragm is blocked). In this case, the notch frequencies occur at 5 to 8 *Hz*. The solid line in Figure 4-17 represents the dynamic stiffness of the soft bushing (the rubber diaphragm is active). In fact, the notch frequencies of this new setup are moved from 5 and 8 *Hz* to 37 to 43 *Hz*. Thus, the hydraulic bushing remains soft for a wider frequency range.

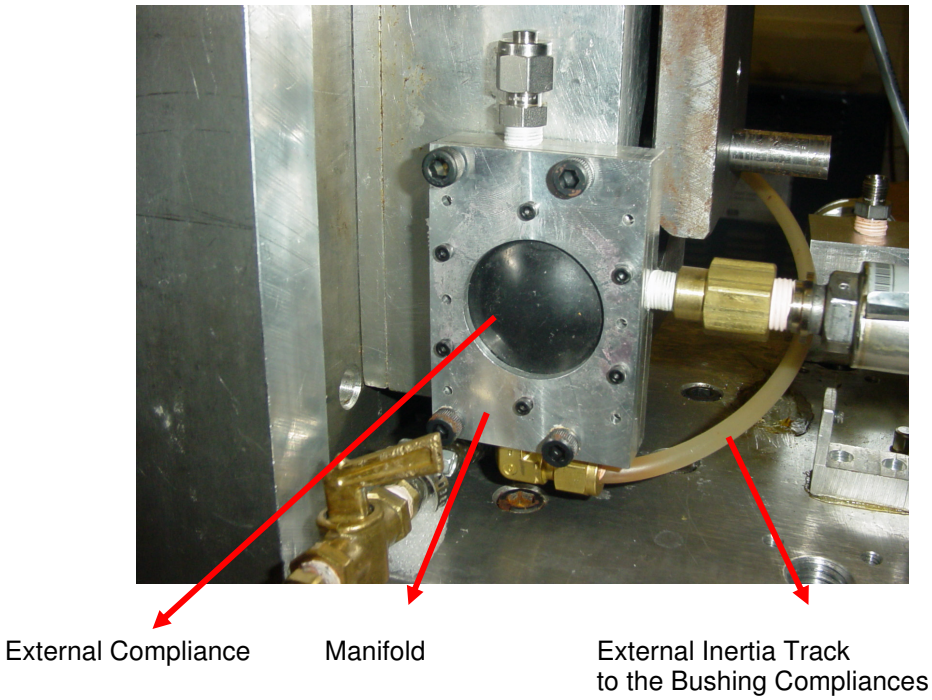

Figure 4-15: Experimental setup for the VDE isolation proof of concept

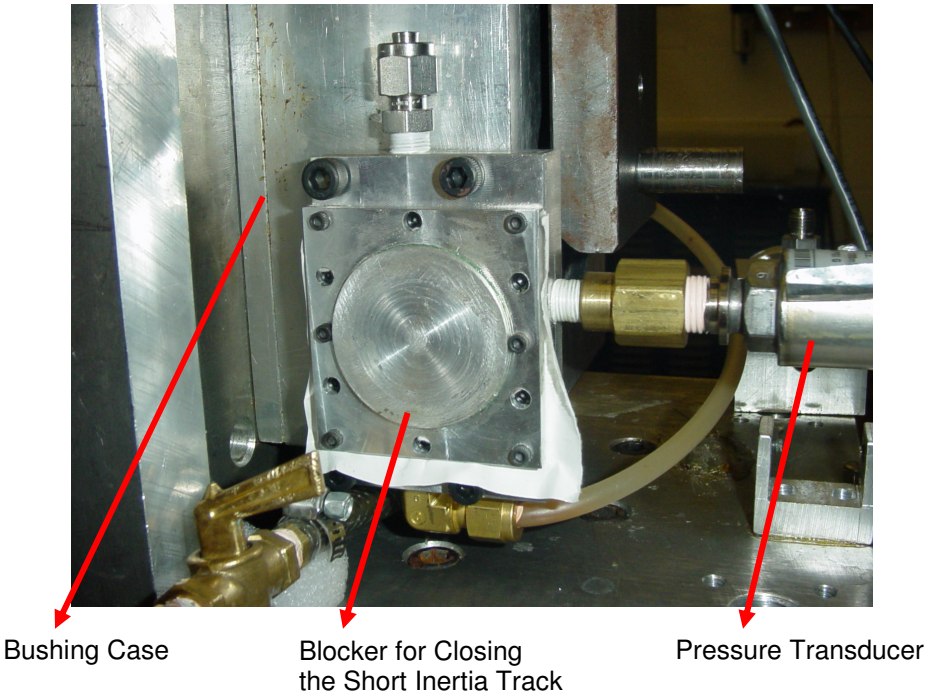

Figure 4-16: Blocking the short inertia track

In practice, this method can be easily implemented, by two simple steps, on the existing hydraulic bushing. The first step is to block the short track that connects the two

compliance chambers on top. As a result, the internal inertia track is connected to only one of the chambers and the other chamber is disabled. Now, to satisfy the short inertia track requirement, a shortcut from the pumping chamber to the disabled compliance chamber is provided. The opening and closing of this short track is easily controlled by a solenoid valve. it can be activated or deactivated by receiving a signal from the engine, when it switches to the VDE mode. The long inertia track inside the bushing, which is always open, generates the normal dynamic performance of the hydraulic bushing.

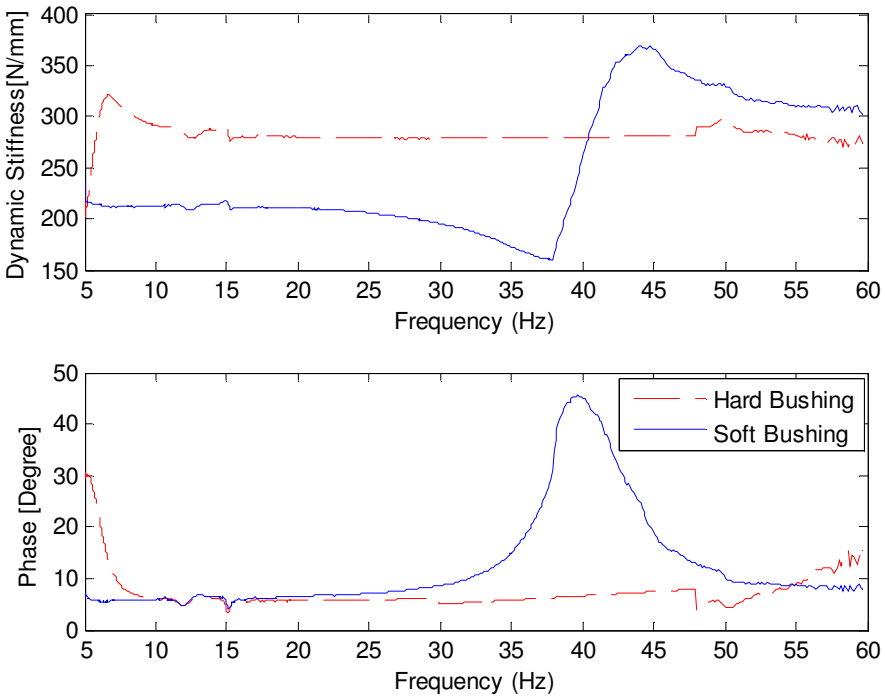

Figure 4-17: Dynamic stiffness results of the DOD isolation experiments

4.4 Summary

In this chapter, the effect of the inertia track resistance on the dynamic stiffness is first predicted by the mathematical model, developed in the previous chapter and verified experimentally. Then, the effect of the inertia track size on the dynamic stiffness is studied. It is proved, numerically and experimentally, that the frequency response of the

hydraulic bushings can be altered by controlling the inertia track coefficients. The experimental results prove that the VDE isolation problem requirements are achieved by adding a short inertia track to the existing hydraulic bushing system, and the internal inertia track is still kept open for the normal engine operations. The frequency range of the soft bushing can be adjusted by designing a proper inertia track size. Indeed, it can be activated or deactivated by a solenoid valve.

Chapter 5: Semi-Active MR Bushing

In the previous chapter, the effect of the inertia track on the hydraulic bushing dynamic stiffness response was discussed. The damping coefficient is controlled by placing a butterfly valve on the external inertia track, and the notch frequencies are located by changing the size of the inertia track. The experimental results indicate a significant shift in the notch frequencies to the left by introducing a short inertia track. It is concluded that the VDE isolation requirements can be achieved with some minor changes in the design of the existing hydraulic bushing.

The only problem with utilizing the short inertia track is its low damping force. In reality, there are frequencies at which high damping is essential (such as the engine's natural frequency). The low damping characteristic of the short inertia track can be well observed by looking at the phase response in Figure 4-17. In fact, the amplitude of the phase response at the notch frequencies exhibits a higher peak. In reality, the short inertia track alone can not apply much resistance to the fluid flow. As a result, an additional system is needed to obtain the damping requirements. In this chapter, the design of an MR valve is explained. This valve is eventually used as an attachment to the external compliance chamber, designed in the previous chapter, to eliminate the inefficient low damping.

5.1 MR Fluid Behavior and Modeling (Background)

MR fluids are micronized size solid particles suspended in a fluid. Applying a magnetic field aligns the particles in the field direction and enhances of the shear stress. This property can be well utilized in isolators to control the damping.

Most of the devices that use MR fluid have either fixed magnetic poles or moveable magnetic poles (there is a third mode called squeeze-film). The fixed magnetic pole devices are classified under the pressure driven flow mode, whereas the movable magnet cases are categorized as a shear mode. The servo valves, dampers, and shock absorbers are examples of the flow mode class, and the shear mode includes clutches, brakes, and locking devices.

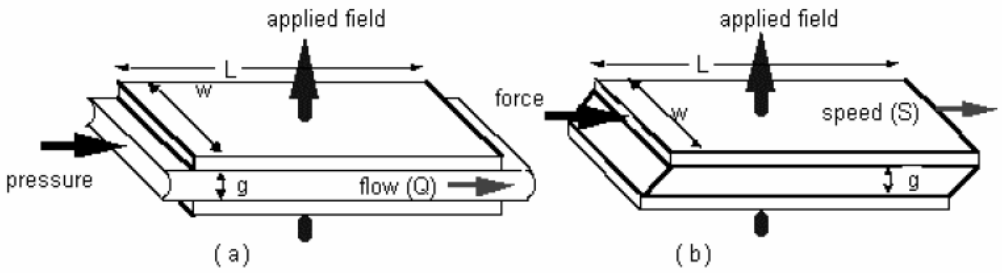

Figure 5-1: pressure driven flow mode (a), direct-shear mode (b) (photo from the Lord Corporation)

In this thesis, only the flow mode is used. The pressure drop in the flow mode is the sum of viscous component ΔP_η and field dependent component ΔP_τ, and is expressed by

$$\Delta P = \Delta P_\eta + \Delta P_\tau = \frac{12\eta QL}{g^3 w} + \frac{c\tau_y L}{g}, \qquad (5.1)$$

where *L,g,* and *w* are the length, gap ,and width of the flow channel, Q is the volumetric flow rate, η is the fluid viscosity with no applied field, and τ_y is the yield stress developed

in response to an applied field. Parameter c has a value ranging from 2 for $\Delta P_\tau / \Delta P_\eta < 1$ and 3 for $\Delta P_\tau / \Delta P_\eta > 100$.

The MR fluid used is formulation developed by General Motors Corporation, and referred to as 13MAG098. The approximate magnetic properties of this fluid are summarized in Figure 5-2 and Table 5-1.

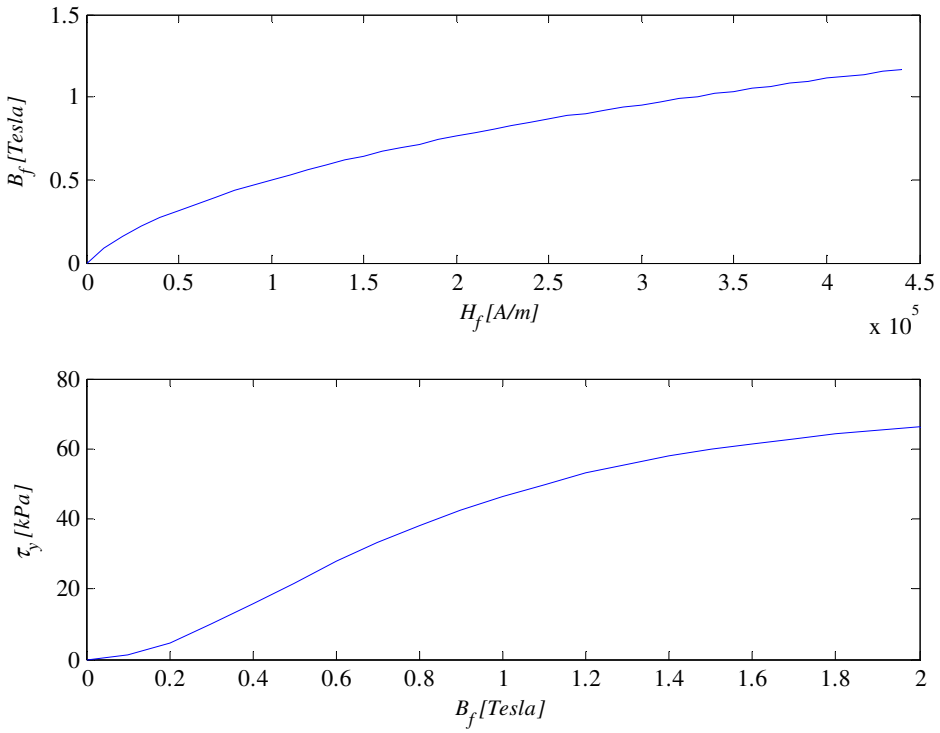

Figure 5-2: Magnetic properties of GM Corp. formulated MR Fluid 13MAG098.

Table 5-1: Properties of GM Corp. formulated MRF 13MAG098.

Fluid Parameter	**Value**
Percent Solids (by volume)	30 %
μ_f	0.173 Pa·s
ρ_f	2910 kg/m^3

5.2 MR Chamber

There are various methods for applying resistance to the fluid motion. At first glance, adopting a proportional valve seems to work. However, due to the small size of the inertia track, placing a proportional valve largely affects the frequency shift which is produced initially by the short track. In other words, the level of the opening of the proportional valve drastically changes the size of the short inertia track.

The required damping for this semi-active hydraulic bushing is achieved by incorporating the MR fluid in the hydraulic bushing. Then, an MR valve can be adopted to control the semi-active bushing damping. The good thing about the MR valve is that, it changes the damping of the system with a minimum violation of the dynamic response of the original system. An MR valve creates damping by changing the shear stress of the MR fluid. This process is accomplished by aligning the suspended iron particles in the fluid. As a result, in the inertia track size, none of the key factors that participate such as viscosity and the dimensions of the track are altered. For the MR valves, the best performance is obtained when the iron particles alignment take place in a direction perpendicular to the flow direction. This is the ultimate goal of designing such valves.

Although MR fluid is a suitable material to create variable damping, economic concerns have restricted its usage, especially in the automotive industry where a semi-active engine mount/bushing should not exceed $20 (one liter of MR fluid is approximately $1,000 US). To overcome this, an innovative MR compliance chamber is purposed. The idea is to minimize the amount of MR fluid required in the conventional bushing. To do so, the MR valve, which is the only component that needs the MR fluid, is

separated from the rest of the hydraulic operating components by a rubber diaphragm. A schematic view of the MR compliance chamber is shown in Figure 5-3.

The MR compliance chamber is shown in Figure 5-4. In this design the MR valve system is separated from the rest of the hydraulic bushing. This chamber operates due to the fact that the interconnections among the different components in the hydraulic bushing take place because of the fluid pressure. Now, if the pressure is transmitted by other means than the use of a fluid as an agent, different parts can be separated and then filled with different fluid. This works in this application, because the MR valve is the only component in the entire system that depends on MR fluid for operation. To transfer the pressure to the MR valve, a flexible diaphragm is used. It behaves as a separator, and forces the MR fluid to travel through the MR valve back and fourth.

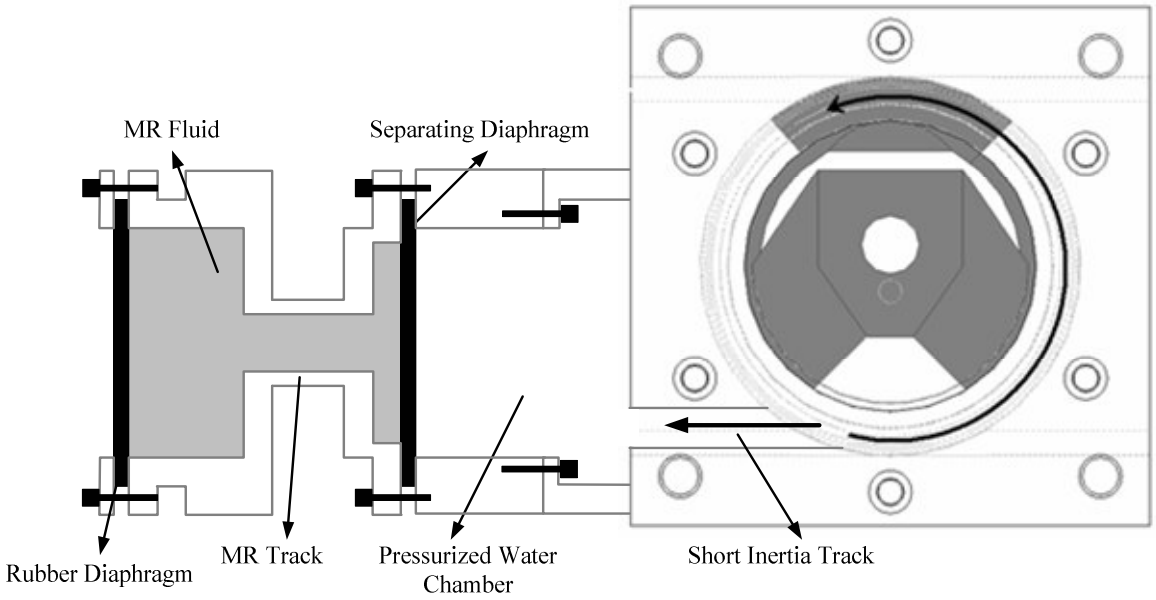

Figure 5-3: MR compliance chamber schematic view

In practice, the pressurized water from the pumping chamber accumulates in the pressurized water chamber (a small inertia track connects the pumping chamber to this chamber). This pressure excites the separating diaphragm which then acts as a pump. The

excitations are then transmitted to the MR fluid which is kept inside the MR chamber and separated from the pressurized water chamber by the diaphragm. As a result, the MR fluid moves back and fourth in the MR track. The other rubber diaphragm at the end of the MR chamber, forces the MR fluid to flow through the MR valve, due to the diaphragm's volumetric extensions and contractions, similar to that of a common compliance chamber's behavior.

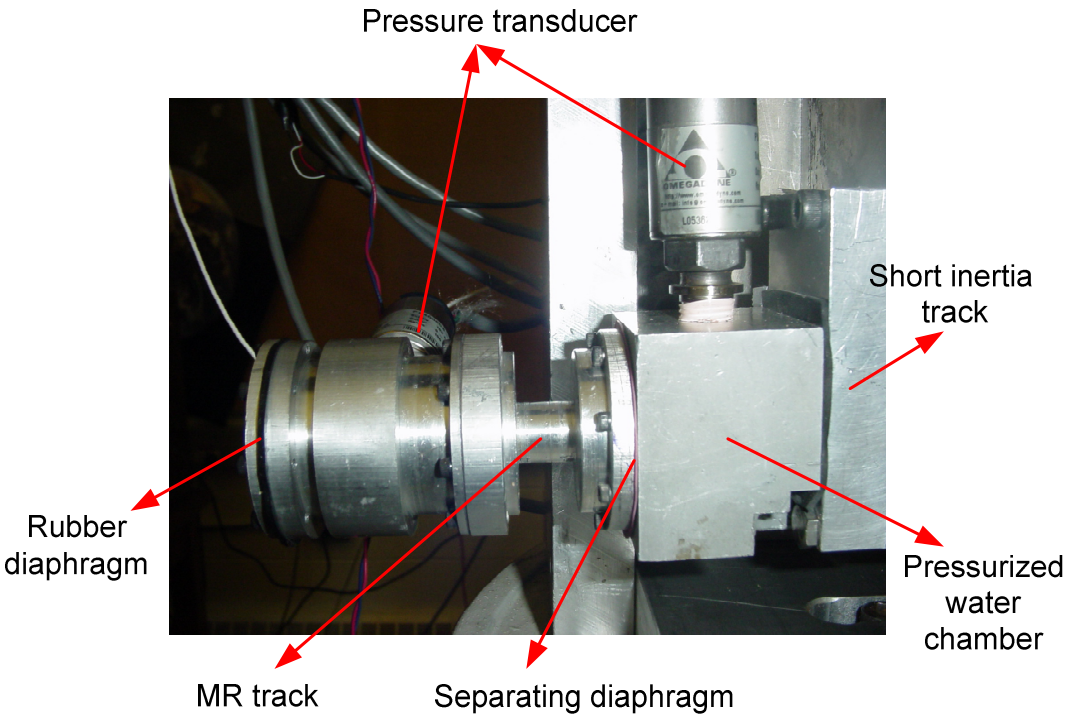

Figure 5-4: MR chamber different components

To produce the required controllable magnetic field, a solenoid coil is used. Here, the magnetic field density can be adjusted by varying the applied current. Two soft iron manufactured shoes are connected to the core of the solenoid coil to close the magnetic field and concentrate the intensity of the magnetic field on the MR track. To direct the magnetic field perpendicular to the MR fluid flow direction, the gap between the arms is designed as a circle to enclose the MR track. An iron core is placed inside the MR track

to direct the field perpendicular to the flow direction. The solenoid coil and a schematic view of the MR valve are apparent in Figure 5-5.

In addition, a FEMLAB simulation is performed to verify the direction of the magnetic filed to the MR flow direction. The simulation results are depicted in Figure 5-6. In this model the MR flow is normal to the figure plane. The magnetic flow streamlines enter the iron core and leave it radial which is ideal for maximizing the damping force.

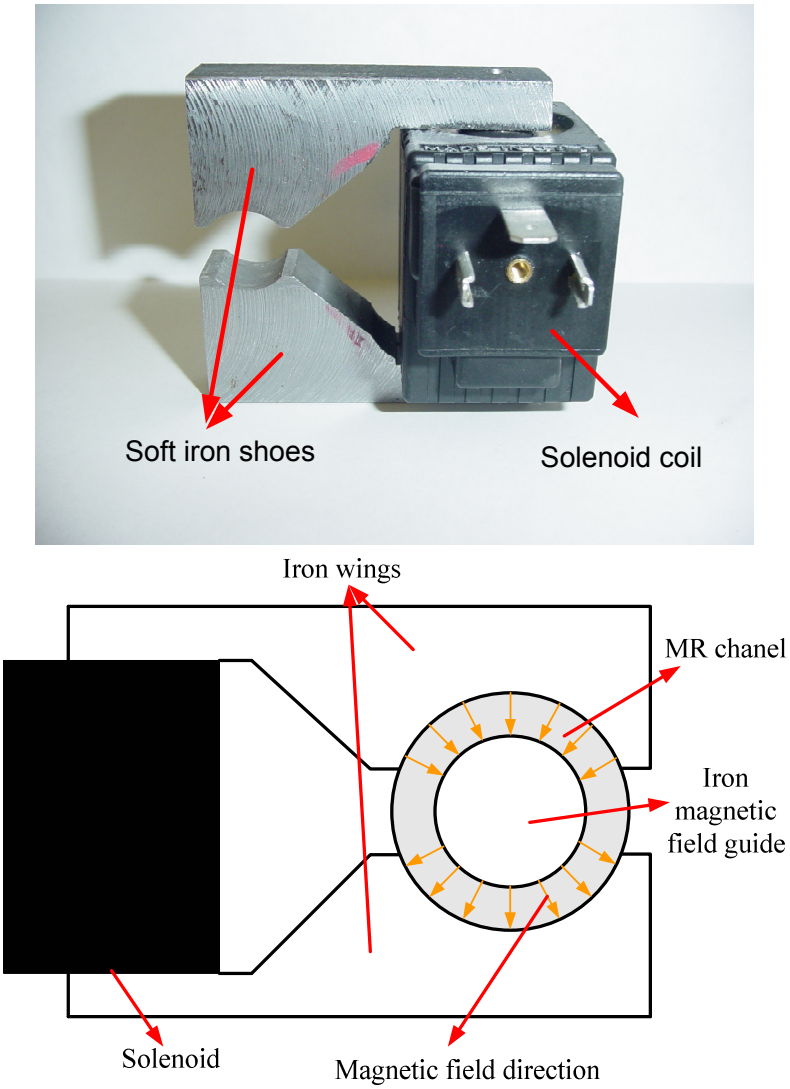

Figure 5-5: Adjustable magnet device (left) and the schematic view of the field direction in the MR inertia track (right)

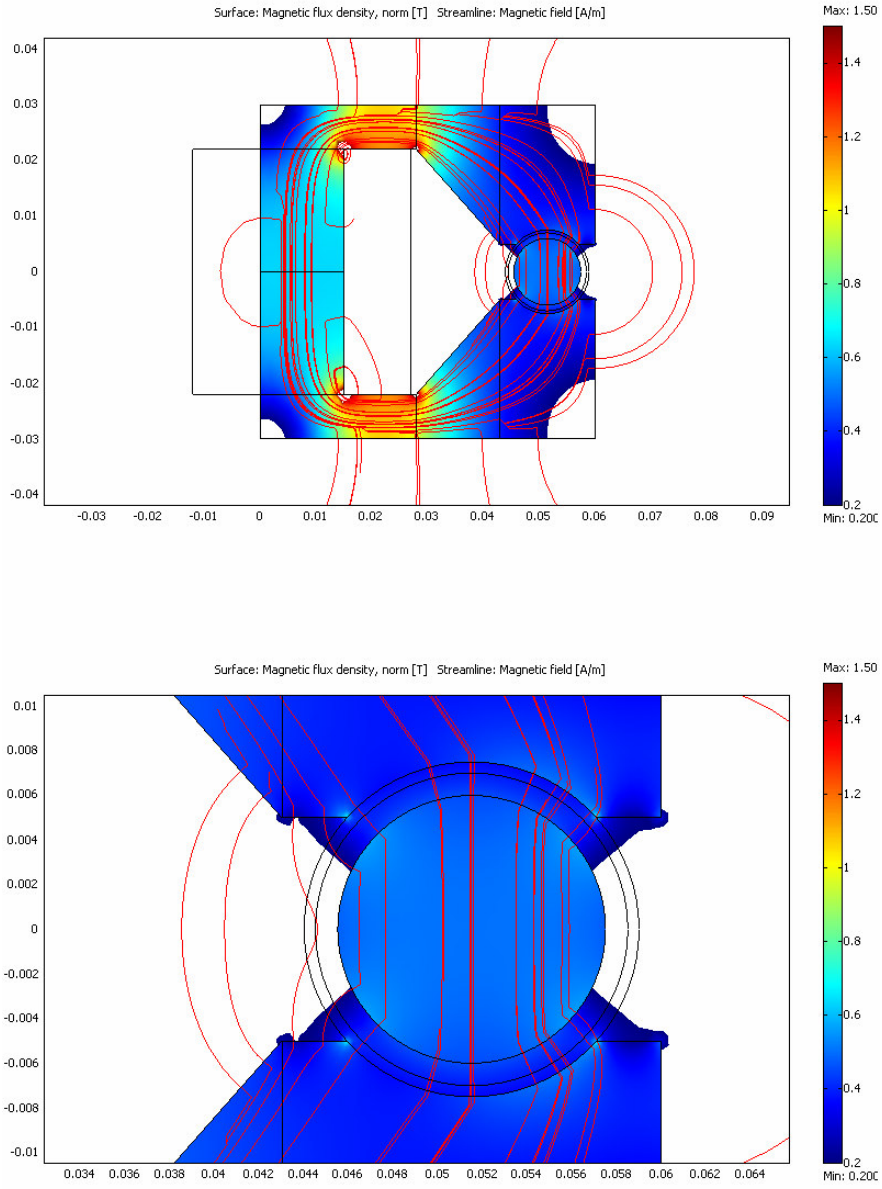

Figure 5-6: FEMLAB simulation of the MR track magnetic field

Similar to the schematic view of the hydraulic bushing in the Chapter 3, a schematic model of the MR semi-active hydraulic bushing is produced as shown in Figure 5-8. This model is used to offer a better understanding of the physical system to derive the required equations. Most of the components in this model are the same as the

one described in Section3.1. More components are added to represent the MR compliance chamber. In Figure 5-7, the separating diaphragm is modeled by compliance C_2. The pressure in the pressurized water chamber and in the MR chamber before and after the MR valve are denoted by P_2, P_3 and P_4 respectively. A_{MR} corresponds to the MR track cross-section area. Similar to the separating diaphragm, the rubber diaphragm covering the MR chamber is modeled by compliance C_3.

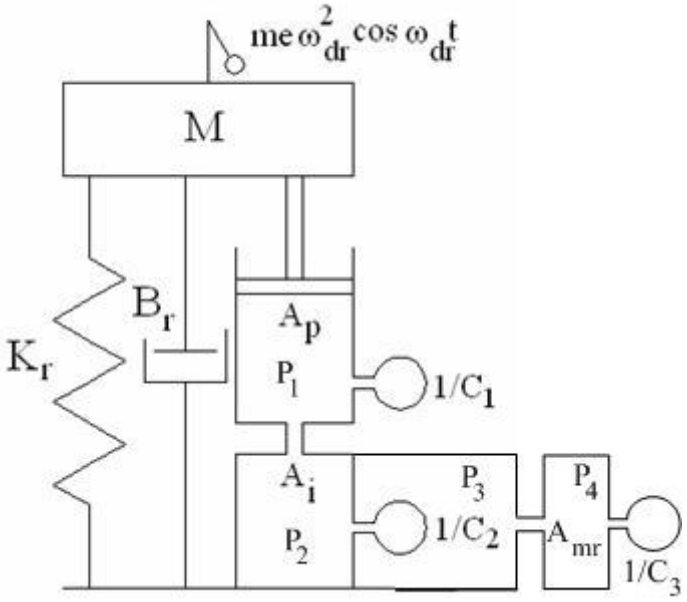

Figure 5-7: Schematic view of the semi-active bushing

Based on the schematic model in Figure 5-8, the governing equations of the new system are

$$C_1\dot{P}_1 = A_p\dot{X} - Q_i\,, \tag{5.2}$$

$$C_2(\dot{P}_2 - \dot{P}_3) = Q_i\,, \tag{5.3}$$

$$P_1 - P_2 = I_i\dot{Q}_i + R_iQ_i\,, \tag{5.4}$$

$$C_3\dot{P}_4 = Q_i\,, \tag{5.5}$$

and

$$P_3 - P_4 = I_{MR}\dot{Q}_i + R_{MR}Q_i \ . \qquad (5.6)$$

Some of these differential equations are similar to those of the conventional hydraulic bushing. That is because the main features of the hydraulic bushing system, such as the pumping chamber and short inertia track are the same as those in the semi-active and hydraulic systems. Equations (5.2) to (5.6) are solved by using the Laplace transform. The final results are summarized as

$$P_1 = \frac{A_p}{C_1}\frac{Is^2 + Rs + 1/C_2 + 1/C_3}{Is^2 + Rs + 1/C_1 + 1/C_2 + 1/C_3}, \qquad (5.7)$$

$$P_2 = \frac{A_p}{C_1}\frac{I_{MR}s^2 + R_{MR}s + 1/C_2 + 1/C_3}{Is^2 + Rs + 1/C_1 + 1/C_2 + 1/C_3}, \qquad (5.8)$$

$$P_3 = \frac{A_p}{C_1}\frac{I_{MR}s^2 + R_{MR}s + 1/C_3}{Is^2 + Rs + 1/C_1 + 1/C_2 + 1/C_3}, \qquad (5.9)$$

and

$$P_4 = \frac{A_p}{C_1C_3}\frac{1}{Is^2 + Rs + 1/C_1 + 1/C_2 + 1/C_3}. \qquad (5.10)$$

where

$$I = I_i + I_{MR}$$

and

$$R = R_i + R_{MR}$$

In the experimental test setup illustrated in Figure 5-8, the rubber bushing is inside the aluminum case, and the internal inertia track is blocked by silicon. The compliance chamber in the previous chapter is used here again to connects the pumping chamber to the MR chamber via the short inertia track. The compliant diaphragm of the compliance chamber acts as a separating flexible diaphragm. The pressurized water from

the pumping chamber activates the separating diaphragm, causing the MR fluid to move through the MR track. Various sensors are involved in this test setup to measure different important variables. A Sensotec Model 41, 1000 lb precision pancake load cell is used to measure the transmitted force by the hydraulic bushing. For the displacement, a SpaceAge Control, string potentiometer, Model 173, is employed. Three OMEGADYNE pressure transducers model PX4000C6 are utilized to monitor the pressure at key locations in the semi-active bushing assembly.

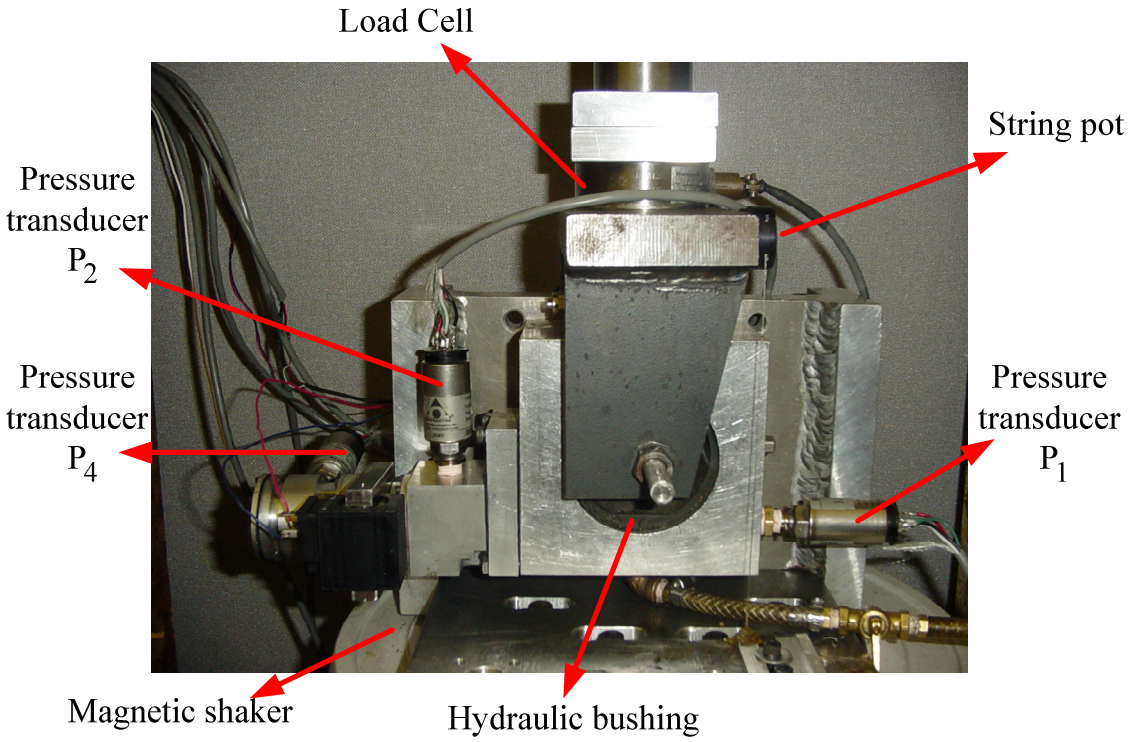

Figure 5-8: Semi-Active bushing test bed

In the experiments, a flexible thin rubber is selected for the separating diaphragm and for the rubber diaphragm in the MR chamber, a low compliant material is chosen. Therefore, the compliance of the separating diaphragm can be neglected; that is, the separating diaphragm is not applying much resistance to the expansions and contractions. Practically this means that P_2 and P_3 should be identical. Moreover, the length of the MR

track is longer than the short inertia track, since the MR should be made thinner and longer to increase the resistance. As a result, P_1 and P_2 should have similar pressure transmissibility curves, as illustrated in Figure 5-9. The experimental results show that the first notch occurs at 44 *Hz*: this is the natural frequency of the numerator in (5.7) and (5.8) which, approximately, is

$$\omega_{n1} = \sqrt{1/\ IC_3}$$

As it was discussed in Section 3.1, after this frequency the bushing passes through a transient phase from a soft to a stiff isolator. According to the experimental results, this transition is completed at 47 *Hz*. This frequency is the natural frequency of the denominator in (5.7) and (5.8) which, approximately, is

$$\omega_{n1} = \sqrt{1/\ IC_1}$$

From (5.7) and (5.8), the low and high pressure regions are approximated by A_p/C_3 and A_p/C_1 , respectively.

Similar to the second order transfer functions, the frequency response phase shift is 180°. Contrarily, if the second order transfer function is in the denominator, a -180° phase shift is expected. In (5.7) and (5.8), the second order terms exist in both the numerator and denominator. Therefore, since the two notch frequencies are close, the 180° and -180° phase shift can not be completed. Consequently, a phase bump is expected. In fact, the phase rises to 180° but is canceled by the negative phase shift produced by the second order transfer function in the denominator. The phase shift of the pressure transmissibility is depicted in Figure 5-9, and proves the validity of the pressure equations in (5.7) and (5.8).

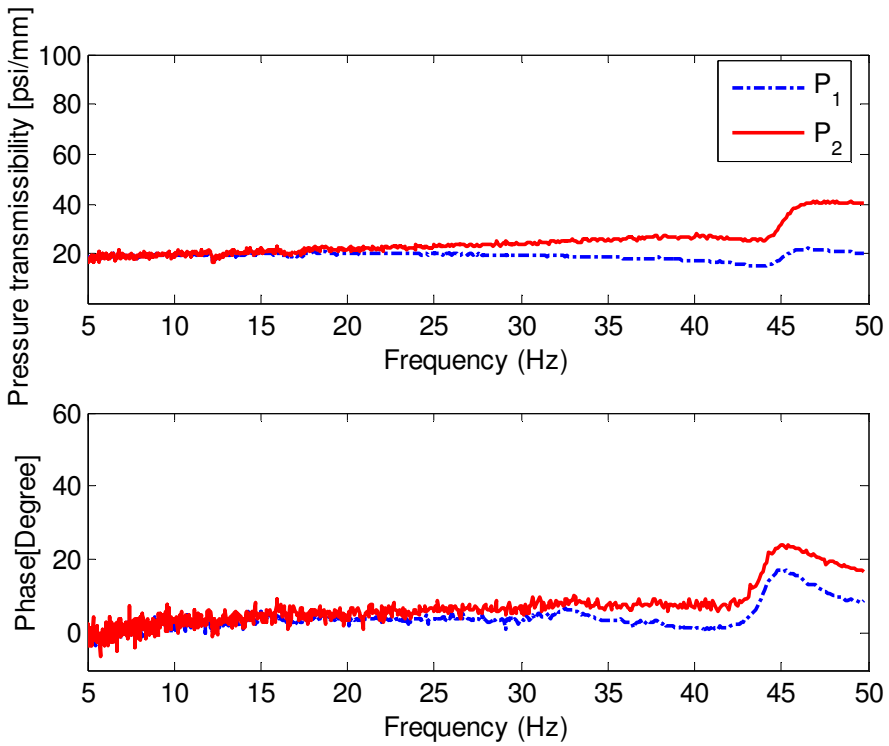

Figure 5-9: Pressure response of the pumping and the pressurized water chambers

The pressure response curve inside the MR compliance chamber P_4 is different than that of P_1 and P_2, because, (5.10) is not similar to (5.7) to (5.9). According to (5.10), the pressure should drop at the denominator notch frequency. In addition, the phase response should exhibit only a -180° shift. The MR chamber frequency response is presented in Figure 5-10. Despite what anticipated by (5.10), the pressure phase response demonstrates a -150° phase shift. Moreover, although the pressure amplitude drops at the beginning, it starts increasing again at 49 *Hz* which contradicts the anticipated response.

These contradictions can be explained by investigating the vibration of the MR compliance chamber. To measure that, an accelerometer is attached to compliance chamber. The phase difference between the MR chamber and the bushing case acceleration is shown in Figure 5-11. This experiment demonstrates an unexpected resonance in the MR compliance chamber. In fact, this vibration exists because the MR

chamber is long, and as a result, acts like a cantilever beam. In deriving the semi-active bushing equations, it is assumed that the MR compliance chamber remains stationary with respect to the aluminum block. The experimental results reveal that this assumption is violated. According to the experimental results the natural frequency of the MR chamber is between 40-45 *Hz*. This frequency region is the same as that of the notch frequency in (5.10) . As a result, the MR chamber pressure response does not fully agree with that of the mathematical model.

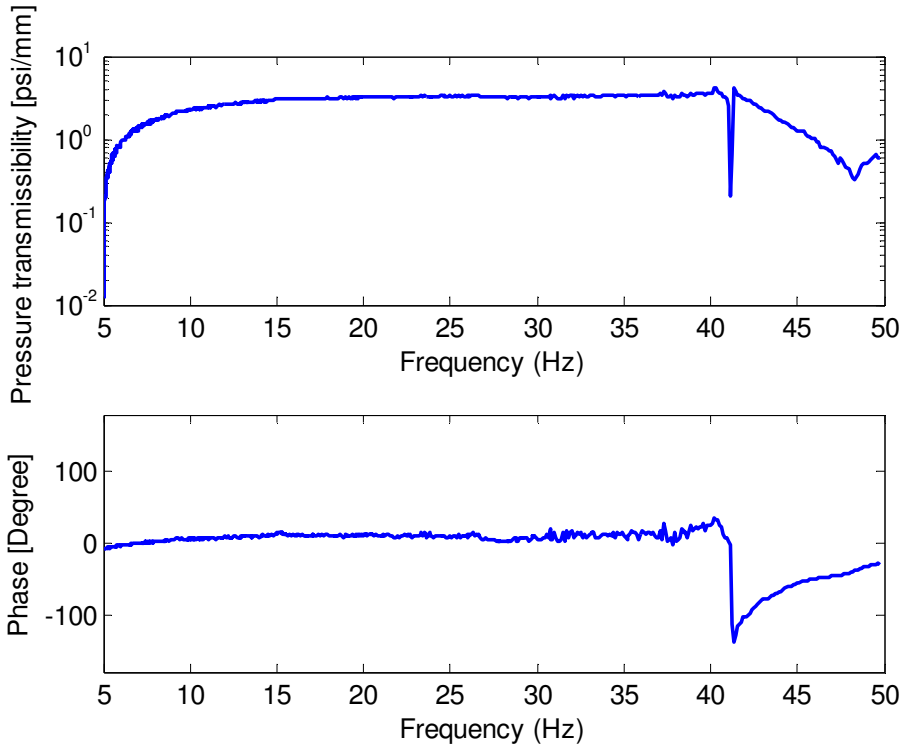

Figure 5-10: MR chamber pressure response

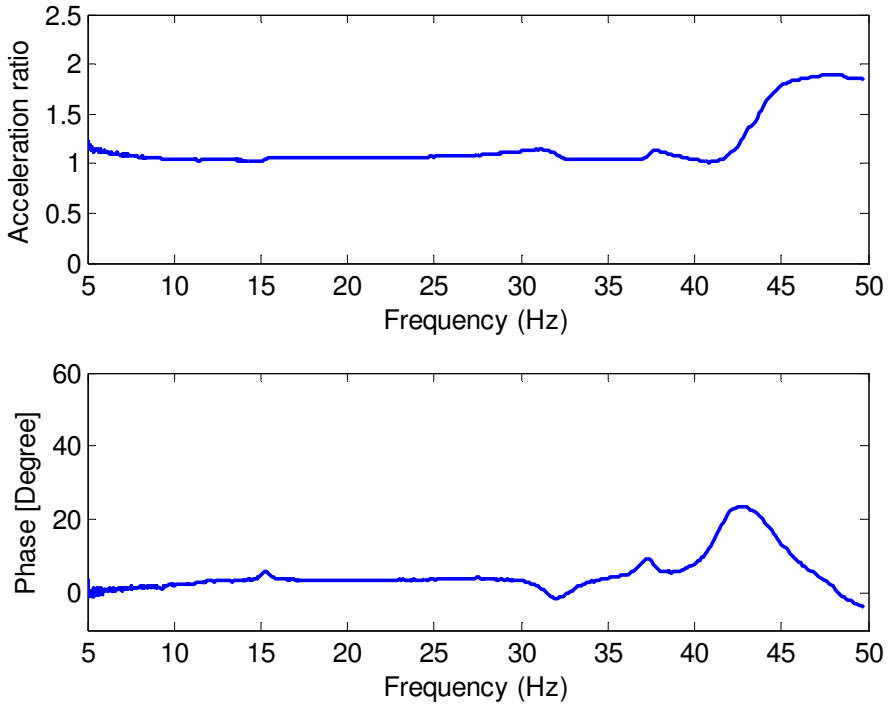

Figure 5-11: Vibration analysis of the MR chamber attachment

5.3 Damping Effect on Dynamic Stiffness response

The pressure transfer functions for the different chambers of a semi-active bushing are given in the previous section. The transmitted force can still be calculated by (3.7). The only difference is the pressure transfer function in the passive and the semi-active bushings. Therefore, the dynamic stiffness equation can then be found by substituting (5.7) into (3.7)

$$K_{dyn} = K_r + B_r s + \frac{A_p^2}{C_1} \frac{Is^2 + Rs + 1/C_2 + 1/C_3}{Is^2 + Rs + 1/C_1 + 1/C_2 + 1/C_3}. \qquad (5.11)$$

For (5.11) and (3.9), the transfer functions are similar. Therefore, the experimental dynamic stiffness curves of the semi-active system should exhibit the same pattern; that is, a soft and a stiff region.

The dynamic stiffness response of the semi-active bushing is first obtained for the inactive MR valve (no current state). The experimental results are depicted in Figure 5-12. As expected, the dynamic stiffness curve is similar to the one shown in Figure 4-17 for the small inertia track. The semi-active bushing is then tested for several current inputs. At I=0.5 *amp*, the MR track is saturated. The experimental results show the peak of the dynamic stiffness response decreases from 450 to 360 N/mm as a result of the damping produced by the MR valve. A lower peak can also be observed from the phase response, where the phase bump is also reduced from 70° to 53°.

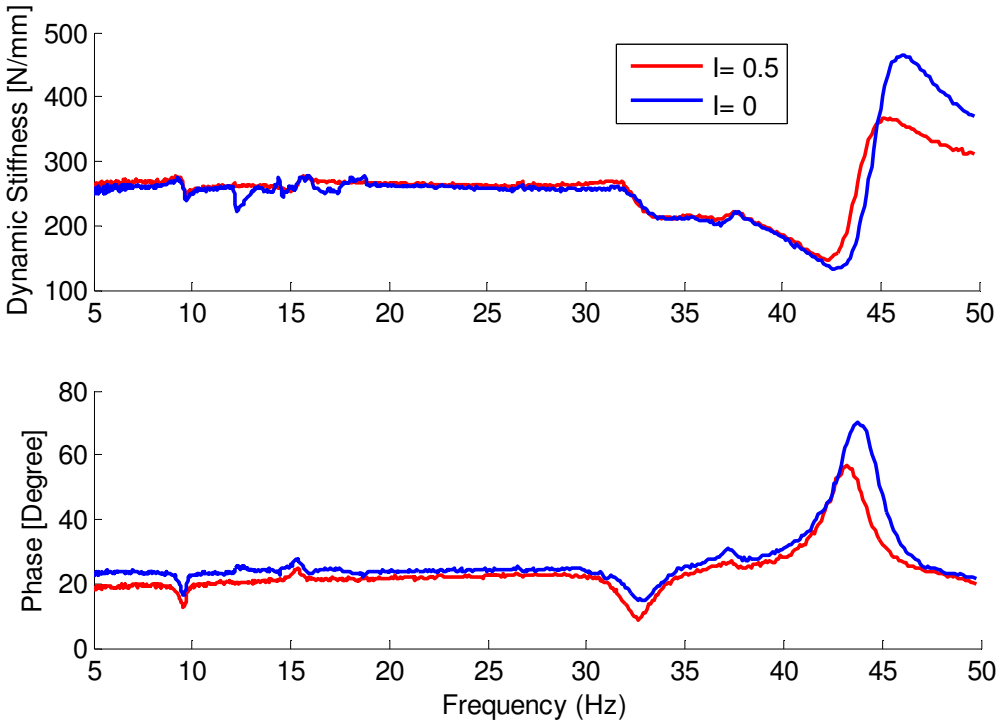

Figure 5-12: Effect of the MR valve on the dynamic stiffness response of the semi-active bushing

In addition, a curve fitting process is performed to quantify the damping produced by the MR valve. For the MR valve no current case, R=0.0041 N-s/mm^5 demonstrates the best fit whereas the best fit occurs for the MR valve full current case at, R=0.0061 N-

s/mm^5. It is interesting that the inertia track size is 0.0003 N-s^2/mm^5 for the semi-active bushing. The experimental results prove that the damping and stiffness of the hydraulic bushing can be controlled by the short inertia track and the MR valve units. This semi-active isolation solution is also economical since it requires no change in the hydraulic bushing design. Moreover the amount of MR fluid needed for this bushing is reduced significantly. More research is needed to improve the quality and placement of the component of this semi-active bushing.

5.4 Summary

In the previous chapter, a short inertia track is utilized by attaching an external compliance chamber to the bushing case. Although the dynamic stiffness response of the bushing exhibits the required extension of the soft region to higher frequencies, due to the short inertia track size, the required damping is not met. An additional MR chamber is introduced for achieving the damping specifications. The innovative feature of this MR chamber is the low MR fluid requirement which makes the solution a cost effective approach. The pressure frequency response at each critical location of the assembly is measured. The responses are in agreement with the mathematical model of the assembly. Finally the dynamic stiffness response of the assembly is measured for the MR valve in no current and full current cases. It is concluded that the newly designed MR valve can produce the required damping by varying the eclectic current.

Chapter 6: Active Chamber Design

The design of a semi-active bushing, based on the VDE isolation requirements, is completed. In the semi-active bushing, the soft isolation requirement for the cylinder deactivation mode is achieved by extending the low dynamic stiffness region of the existing Cooper Standard hydraulic bushing to high frequencies. This shift of the low dynamic stiffness region to high frequencies is accomplished by introducing the additional short inertia track. The lack of damping, due to the shortness of this track, is compensated by attaching an MR valve to the short inertia track unit.

In this chapter, the design of an active compliance chamber is discussed. The goal of this design is to change the pressure response in the pumping chamber. Controlling the pumping chamber pressure is essential because from (3.1) and (3.9) it has a direct relation to the transmitted force and consequently to the dynamic stiffness. Unlike most of the other active counterparts, this design relies on the short inertia track approach developed in Chapter 4. The main contribution of this new active chamber is to compensate for the lack of damping in the short inertia track at the notch frequencies and. to alter damping and stiffness at other frequencies of interest. The last feature ultimately makes the hydraulic bushing independent of the long internal inertia track.

6.1 Active Chamber

As stated above the goal of the new active chamber design is to control the pressure of the pumping chamber. The relation between the pumping chamber pressure and the hydraulic bushing displacement is given in (3.5). This equation is dynamic which means that the active device should be able to provide a frequency dependent pressure

pattern. Thus, the coefficients of the pressure response can be manipulated, and resulting the desired transfer functions.

There are various methods of generating frequency dependent pressure patterns. However, the methods are not generally compatible to the engine environment. The size limitations, besides the power consumption considerations and small frequency ranges of the application, are the restrictive issues for the common active pressure devices. In this chapter, a novel magnetic actuator is designed and utilized to produce the required frequency dependent pressure inside a compliance chamber.

The newly devised magnetic actuator is composed of a permanent magnet and a solenoid coil. The permanent magnet is bonded to a thin rubber diaphragm. The rubber diaphragm also seals the chamber which is filled with water. The electric current in the solenoid coil produces a magnetic field in the direction of the permanent magnet's field. If the magnetic fields of both the solenoid coil and the permanent magnet have the same polarity, they repel each other. However, they are attracted if the polarity is reversed. The active compliance chamber assembly is illustrated in Figure 6-1.

There are several advantages for using this type of actuator to control the pressure in the chamber. Although the mathematical modelling of these actuators usually involves nonlinear terms, practically, these actuators are simple to adapt and easy to control. In this case, the size of the actuator is small which makes it suitable for installation on an existing hydraulic bushing. Moreover, the actuator's low power consumption is ideal for automobile applications and its electrical current feeding characteristic simplifies the controlling purposes.

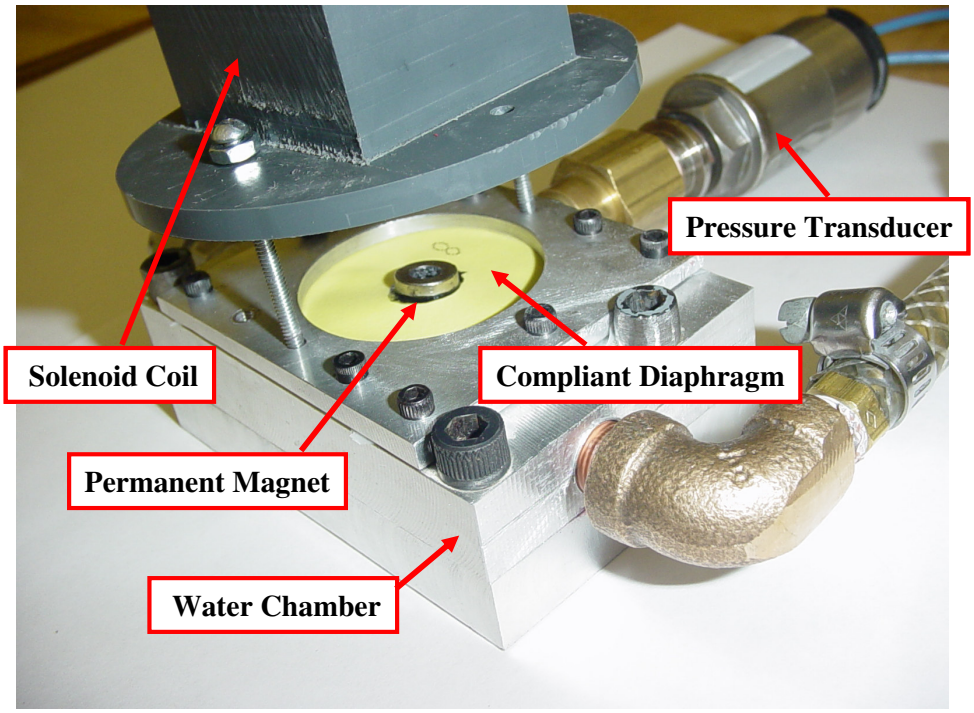

Figure 6-1: Pumping chamber assembly

The general shortcoming of the magnetic actuators is their limited displacement functionalities. This occurs, because the magnetic force is related to the inverse of the distance between the magnetic object and the magnetic field source. In most cases, the effective distance is limited to only a few centimetres. However, this problem does not affect the performance of this magnetic actuator because the amplitude of the vibrations produced by the engine are less than one centimetre, producing not a substantial volume change in the compliance chambers. This amplitude is even smaller for high frequencies (0.1-0.3 mm), where the magnetic actuator is effective. In fact the low displacement characteristic of the magnetic actuator does not affect the desired performance. A schematic view of the magnetic actuator is depicted in Figure 6-2.

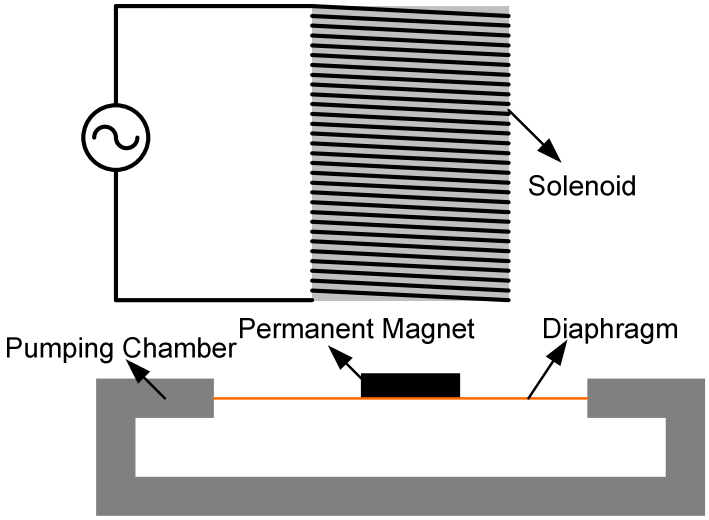

Figure 6-2: Schematic view of the active pumping chamber

Changing the current in the solenoid coil activates the permanent magnet. According to Shameli *et al*, (2006), the magnetic force on the permanent magnet is estimated by computing the following:

$$F = I(\beta + \alpha x), \qquad (6.1)$$

where α and β are constants which are functions of the geometry and the magnetization of the permanent magnet, x is the distance of the permanent magnet from the solenoid coil, and I is the applied current. Here, it is assumed that the effect of the magnetic object on the inductance of the coil is negligible. The lumped model of the active compliance chamber is illustrated in Figure 6-3.

The equation of motion for the permanent magnet is written as

$$M\ddot{x} = F - B\dot{x} - Kx - A_{ap}P_{ap}, \qquad (6.2)$$

Where M is the equivalent mass of the permanent magnet and the diaphragm, and B and K are the damping and stiffness of the elastic diaphragm, respectively. The continuity equation for the active pump is

$$A_{AP}\dot{x} + C_{AP}\dot{P}_{AP} = 0 \qquad (6.3)$$

and then

$$M\ddot{x} = F - B\dot{x} - Kx - A_{ap}^2 x / C_1. \qquad (6.4)$$

By substituting (6.1) in (6.4),

$$M\ddot{x} = \alpha I + \beta Ix - B\dot{x} - Kx - A_{ap}^2 x / C_1. \qquad (6.5)$$

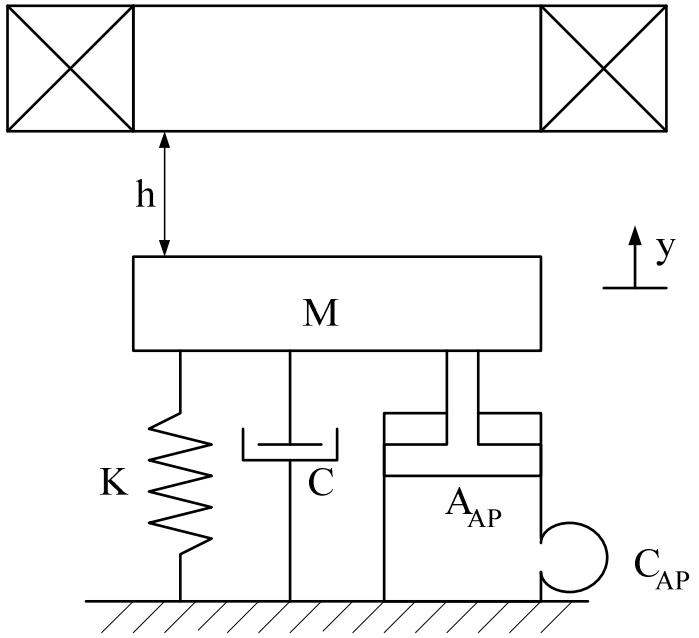

Figure 6-3: Lumped model of the active compliance chamber

The combination of (6.5) and (6.3) defines the frequency dependent pressure produced by the active chamber. The nonlinear terms in (6.5) make the analytical analysis of the dynamic performance of the actuator difficult. The linearization technique to solve (6.5) is described in the next section.

6.2 Linearization

The second term in (6.5), βIx, is a nonlinear term in the differential equation. This equation can be lineraized to enhance the numerical analysis. In this case, the small

displacement of the permanent magnet (in the order of 0.1-3 mm) makes linearization a realistic approach. In fact, (6.5) can be linearized about its equilibrium point. It is described in the following sections all the experiments are performed by sweep sine current input excitations. Therefore, the magnetic displacement also has the sine shape which is oscillating about the permanent magnet resting point .The permanent magnet displacement frequency is the same as that of the current signal frequency. The equilibrium point is defined as

$$I_0 = 0$$
$$x_0 = h$$
$$\dot{x}_0 = 0$$

Thus the state variable is

$$x = y_1$$
$$\frac{dy_1}{dt} = y_2$$
$$I = y_3$$

Then,

$$\frac{dy_2}{dt} = -\frac{B}{M} y_2 - \left(\frac{K}{M} + \frac{A_{ap}^2}{C_{ap} M} \right) y_1 + \frac{\alpha}{M} y_3 + \frac{\beta}{M} y_3 y_1 . \qquad (6.6)$$

Consequently, the linearized equation of motion of the permanent magnet is written as

$$M \Delta\ddot{x} + B \Delta\dot{x} + (K + A_{ap}^2 / C_{ap}) \Delta x = (\alpha + \beta h) I . \qquad (6.7)$$

6.3 Active Compliance Chamber Pressure Frequency Response

There are several techniques to find the frequency response of a dynamic system. Here, a sweep sine input is used. The amplitude of the output frequency response, which is the

active compliance chamber's pressure, is found by filtering the signal at the input excitation frequency. To find the analytical response of the system, let

$$y = r \sin \omega t$$

Then,

$$I_d = A \sin \omega t \ . \qquad (6.8)$$

For (6.8) the particular response of (6.7) is

$$\Delta x = X \cos(\omega t - \theta) \ , \qquad (6.9)$$

where

$$X = \frac{A(\alpha + \beta h)}{\sqrt{((K + A_{ap}^2)^2 - (M \omega)^2)^2 + (B \omega)^2}} \ , \qquad (6.10)$$

and

$$\theta = \frac{B \omega}{(K + A_{ap}^2 / C_{ap})^2 - (M \omega)^2} \ . \qquad (6.11)$$

At low frequencies, the permanent magnet displacement is approximated by

$$X_{ld} = \frac{A(\alpha + \beta h)}{(K + A_{ap}^2 / C_{ap})^2} \ . \qquad (6.12)$$

At higher frequencies it becomes

$$X_{hd} = \frac{A(\alpha + \beta h)}{(M \omega)^2} \ . \qquad (6.13)$$

The transition between the low and high frequency responses happens at

$$\omega_n = \sqrt{\frac{K + A_{ap}^2 / C_{ap}}{M}} \ . \qquad (6.14)$$

The peak value of the permanent magnet displacements depends on the damping of the diaphragm *B*. By substituting (6.12) into (6.3) ,

$$P_{apdl} = \frac{A(\alpha + \beta h)A_{ap}}{(K + A_{ap}^2 / C_{ap})^2 C_{ap}}, \qquad (6.15)$$

and

$$P_{apdh} = \frac{A(\alpha + \beta h)A_{ap}}{(M\omega)^2 C_{ap}}. \qquad (6.16)$$

Therefore, according to (6.15) at the frequencies below ω_n, the pressure frequency response should be a straight line.

To investigate the linearity of the active compliance chamber pressure response, an experiment is performed for the frequencies below 30 *Hz*. The displacement of a magnetic shaker LDS V722 is adopted as a reference signal to the solenoid coil. Dactron SpectraBook and Dactron Shaker Control software is used to command the sweep sine signal to the magnetic shaker. Also, a Dytran accelerometer, Model 3145AG LIVM, is also used as a feedback signal to the shaker controlling unit to maintain a constant sweeping amplitude. Additionally, the acceleration is amplified and then transferred to a computer by a data acquisition A/D card. The Simulink Matlab interface is utilized to calculate the shaker displacement from the shaker acceleration. The displacement output is amplified by a pulse width modulated amplifier (PWM) to produce currents, proportional to the shaker displacement. In all the experiments, the shaker controller unit maintained the displacement constant. The current signal, which is fed to the solenoid coil, for the different gains is depicted in Figure 6-4. It is noteworthy that the spikes at 8 and 21 *Hz* are the responses from the shaker frame. These disturbances can be considered as systematic errors, fed to the active compliance chamber.

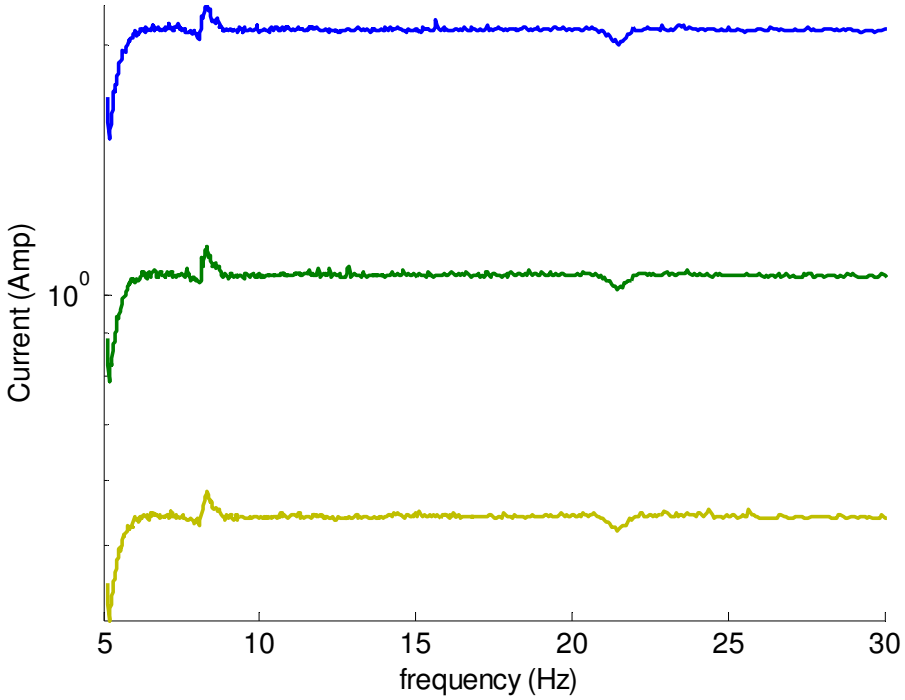

Figure 6-4: Current feeding to the solenoid coil proportional to the shaker displacement

A PX4000C6, OMEAGADYNE pressure transducer is employed to measure the pressure inside the chamber. Figure 6-5 exhibits the experimental results of the displacement proportional current feeding to the solenoid coil. From the experimental results, it is evident that the pressure frequency response follows the feeding current signal linearly. This observation matches the linearized low pressure equation,

$$log\ P_{lv} = L = cte$$

where

$$L = log\ \frac{A(\alpha + \beta h)A_{ap}}{(K + A_{ap}^2 / C_{ap})^2 C_{ap}}$$

It is concluded that increasing the current results in a larger displacement of the permanent magnet, and consequently a higher pressure inside the chamber.

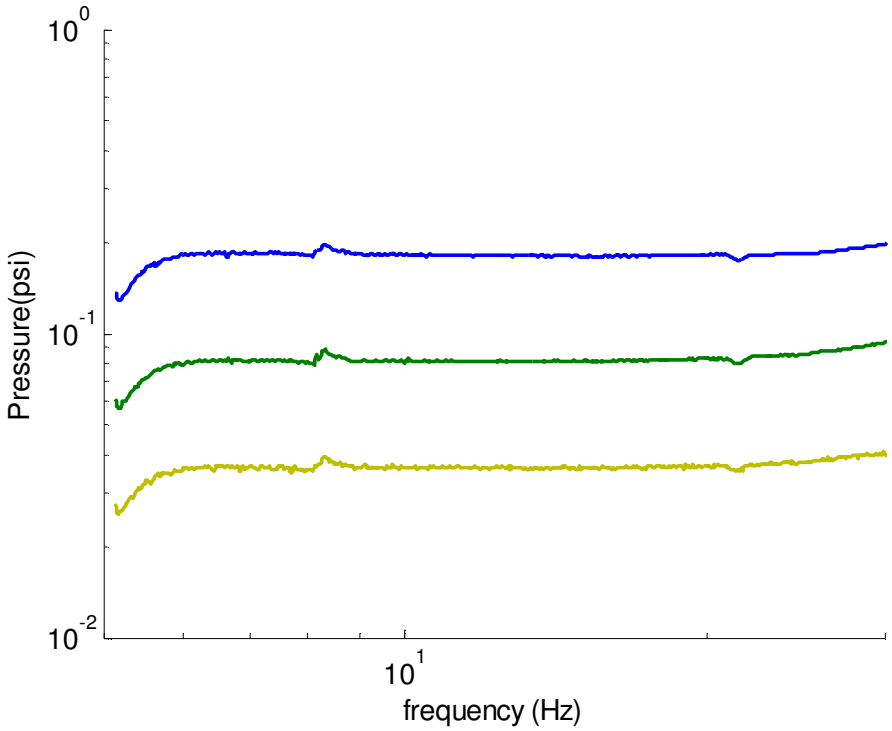

Figure 6-5: Active compliance chamber pressure frequency response for a constant amplitude current sweep

6.4 Other Preliminary Input Signals

In addition, the pressure frequency response of the active compliance chamber to other common displacement related sources of the magnetic shaker (such as velocity and acceleration) is investigated. First, the current signal, proportional to the shaker velocity becomes the commanding input signal. With the same sensor setting which satisfies the constant displacement, the velocity of the shaker is

$v = r\omega sin(\omega t)$

Then

$I_v = A\omega sin\,\omega t$, (6.17)

and

$$log\,|I_v| = log\,A + log\,\omega$$

Therefore, the current curve should be an inclined line with a *log A* offset. The current signal for this case and for different current gains is shown in Figure 6-6. This signal is produced by the integration of the amplified shaker acceleration signal.

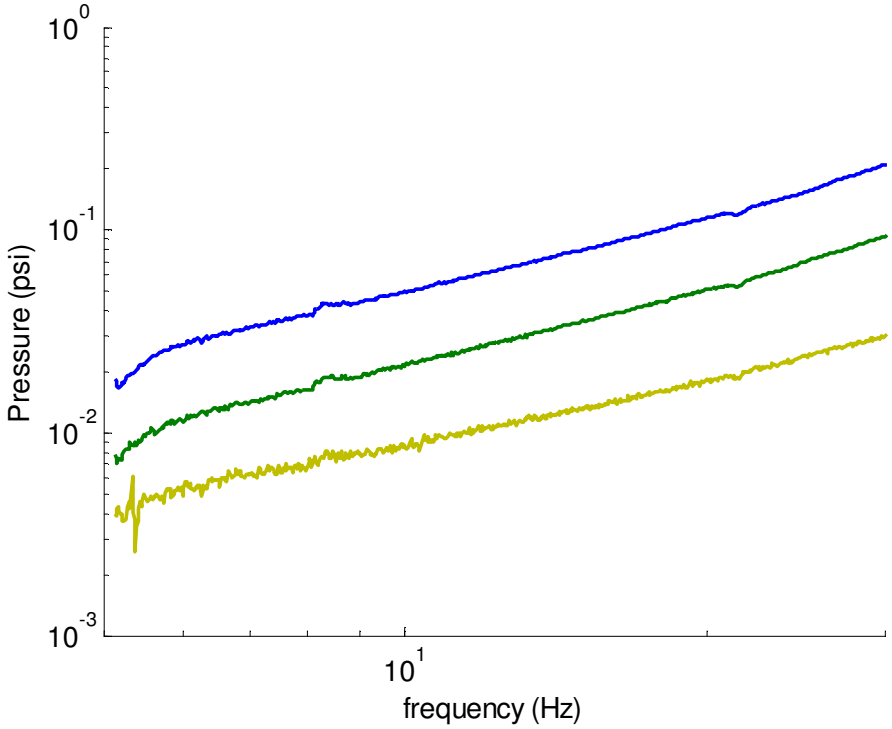

Figure 6-6: Current feeding to the solenoid coil proportional to the shaker velocity

The permanent magnet displacement response for this kind of current source is derived in the same way as that of the previous constant amplitude current case. Thus,

$$X_{lv} = \frac{A\omega(\alpha + \beta h)}{(K + A_{AP}^2 / C_{AP})^2}, \qquad (6.18)$$

and

$$X_{hv} = \frac{A(\alpha + \beta h)}{M^2 \omega}. \qquad (6.19)$$

By using (6.18), the low frequency pressure response is

$$P_{lv} = \frac{A\omega(\alpha + \beta h)A_{AP}}{(K + A_{AP}^2 / C_{AP})^2 C_{AP}}, \qquad (6.20)$$

Then

$$\log P_{lv} = L + \log \omega$$

Like the input current curves, the pressure frequency responses should be inclined lines with offset *L*. In practice, the current signal, proportional to the shaker velocity, is obtained by integrating the shaker acceleration signal. It is then amplified and fed to the solenoid actuator. The pressure frequency response for the velocity proportional current is shown in Figure 6-7. Similar to the displacement proportional current case, the pressure frequency response follows the input current signal linearly.

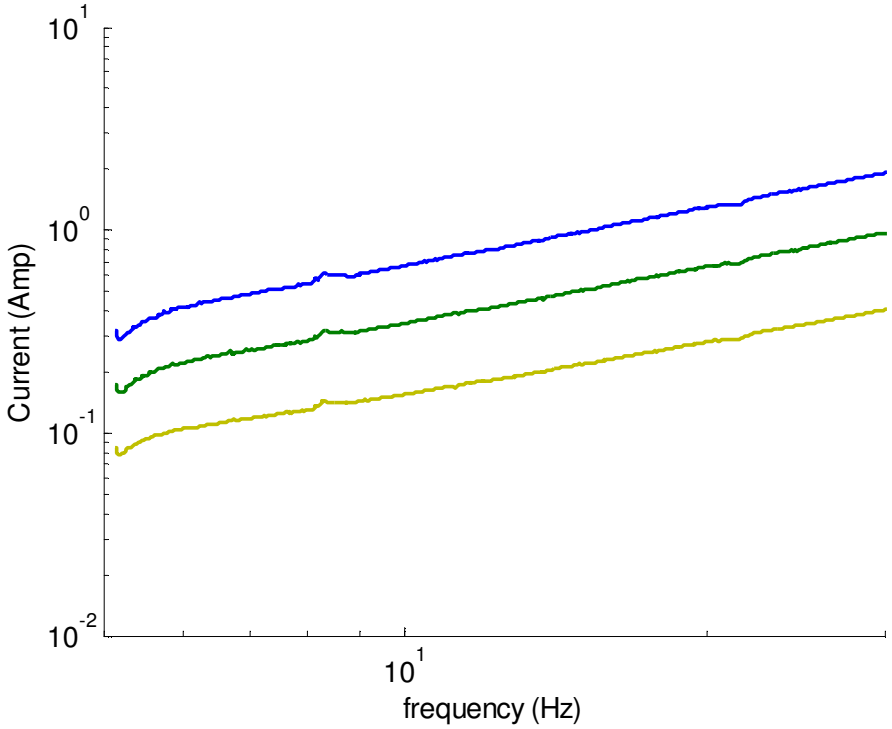

Figure 6-7: Pressure frequency response for a velocity proportional current sweep input

Next, the acceleration signal from the accelerometer is directly adopted as the input to the solenoid coil. Based on the constant amplitude displacement signal, the acceleration signal is

$a = r\omega^2 \sin \omega t$

Then

$$I_a = A\omega^2 \sin \omega t \ , \qquad (6.21)$$

and

$$\log |I_a| = \log A + 2\log \omega$$

Therefore, the acceleration proportional current is an inclined line with a slope twice as that of the velocity current. Figure 6-8 illustrates the current feeding signal to the solenoid coil for the different current gains.

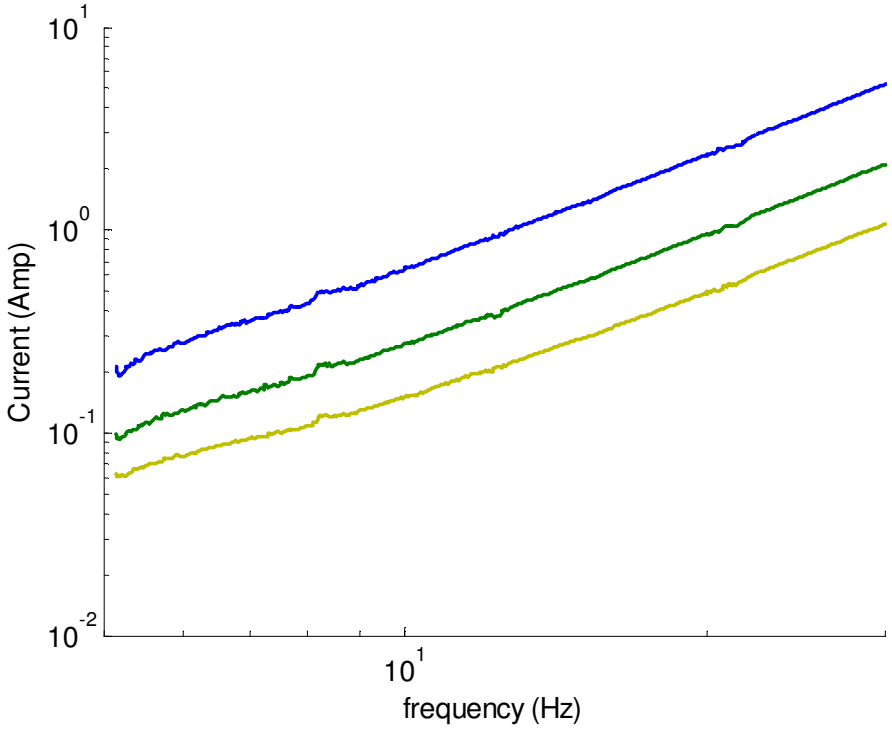

Figure 6-8: Current feeding to the solenoid coil proportional to the shaker acceleration

The linearized low frequency amplitudes of the permanent magnet and active chamber pressure are

$$X_{la} = \frac{A\omega^2(\alpha + \beta h)}{(K + A_{AP}^2 / C_{AP})^2}, \tag{6.22}$$

and

$$P_{lv} = \frac{A\omega^2(\alpha + \beta h)A_{AP}}{(K + A_{AP}^2 / C_{AP})^2 C_{AP}}. \tag{6.23}$$

Then

$$log\ P_{la} = L + 2\,log\ \omega$$

By comparing the velocity and acceleration proportional current feeding pressure responses, the acceleration should display a slope twice as large. The different response slopes of the two types of feeding are observed by comparing Figure 6-9 and Figure 6-7.

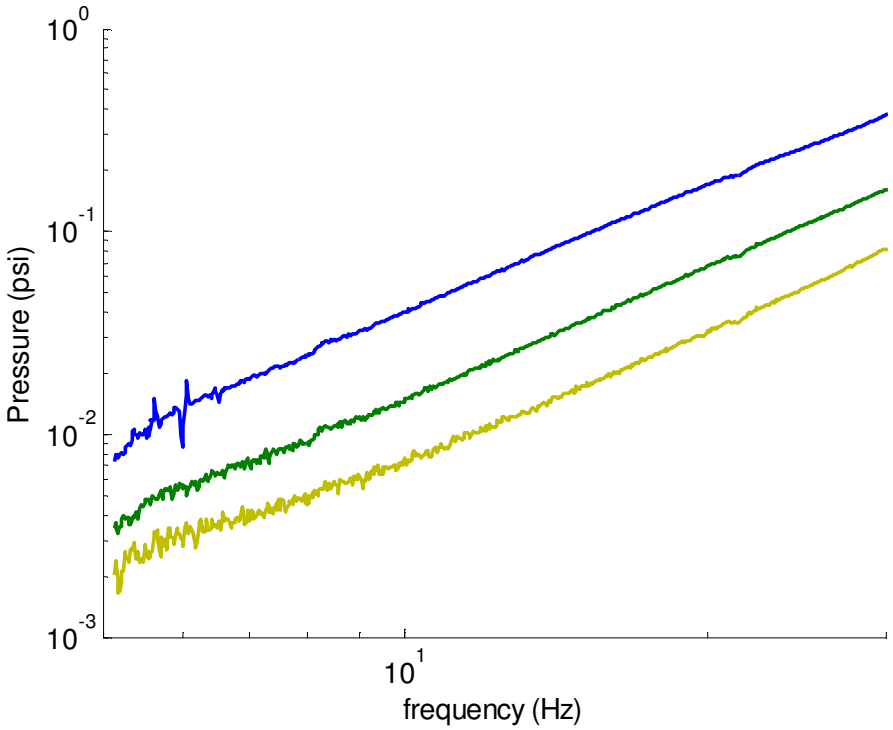

Figure 6-9: Pressure frequency response for an acceleration proportional current sweep input

6.5 Second Order Transfer Function Feedings

As described in the previous section, different pressure frequency responses are generated by the various current feeding sources. However, this reflects only a superficial capability of this active chamber. To explore the more interesting features of this active chamber, it should be pointed out that the displacement has a 90˚ and 180˚ phase shift with the velocity and the acceleration, respectively. A current proportional to each of these three input sources inherits the same properties. These phase shift characteristics are used to generate complex pressure frequency responses. To consider the phase shift characteristic of the different types of current inputs, the following transfer function is utilized to generate a complex pressure response

$$T_1 = \frac{1080}{0.3s^2 + 20s + 1080}. \qquad (6.24)$$

Eqation (6.24) has a quadratic transfer function in the denominator. The displacement, velocity, and acceleration components appear as the coefficients of this quadratic. The same as a conventional second order system, the asymptotic frequency response of (6.24) is a straight line at frequencies below 9.5 *Hz* (this frequency is the natural frequency of T_1) and an inclined line with a negative slope for higher frequencies. Figure 6-10 shows the pressure frequency response to a current source in (6.24). The response proves a close match to the transfer function.

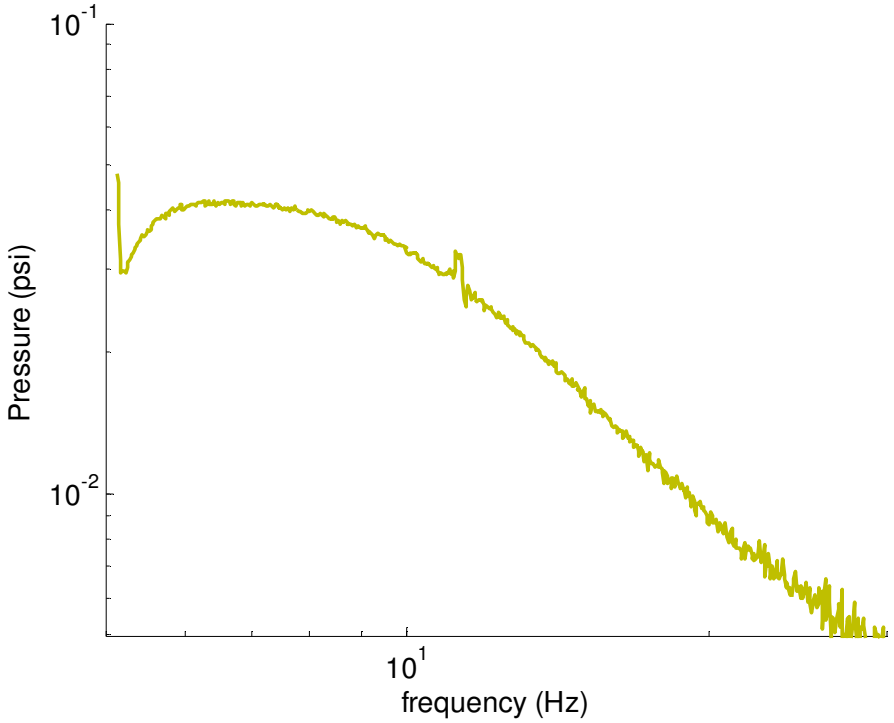

Figure 6-10: applied transfer function pressure response

Like the typical quadratic transfer function, the notch frequency of the response is a function of the square root of the ratio of the constant and s^2 coefficient for small damping ratios. Hence, increasing the constant shifts the notch frequency to higher values and a rise in the s^2 coefficient has the opposite effect. The following transfer function is used to confirm the effect of shifting the notch frequency of the applied current to higher frequencies on the pressure response.

$$T_2 = \frac{4000}{0.3s^2 + 40s + 4000} \qquad (6.25)$$

In this transfer function, the notch frequency of (6.25) is increased to 18.4 *Hz*. The pressure response to this transfer function is depicted in Figure 6-11. Compared to Figure 6-10, the constant amplitude region is now extended to higher frequencies. This

experiment proves that the notch in the pressure frequency response of the active compliance chamber can be easily shifted to any specified frequency.

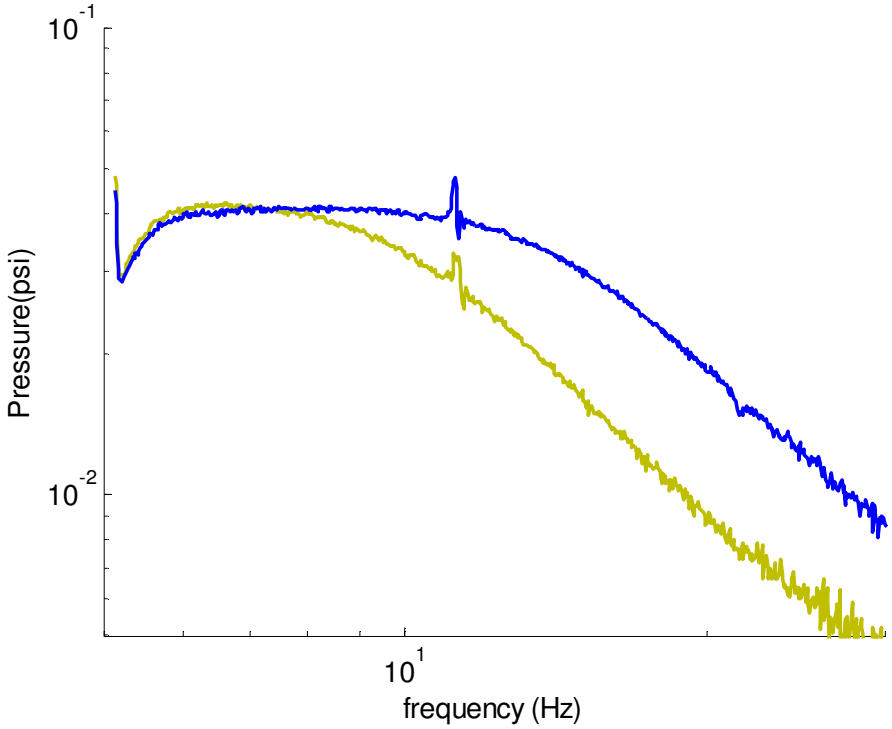

Figure 6-11: effect of the transfer function notch frequency variation on the pressure response

Another experiment is performed to investigate the effect of varying the velocity gain, *s* coefficient, on the pressure frequency response. To do so, the following transfer function is used:

$$T_3 = \frac{4000}{0.3s^2 + 30s + 4000}. \qquad (6.26)$$

Here, the coefficient of *s* (velocity gain) is changed from 40 to 30. The *s* term coefficient in (6.26) defines the damping in the system. The damping coefficient in a typical quadratic transfer function affects the notch amplitude of the frequency response, as observed in Figure 6-12.

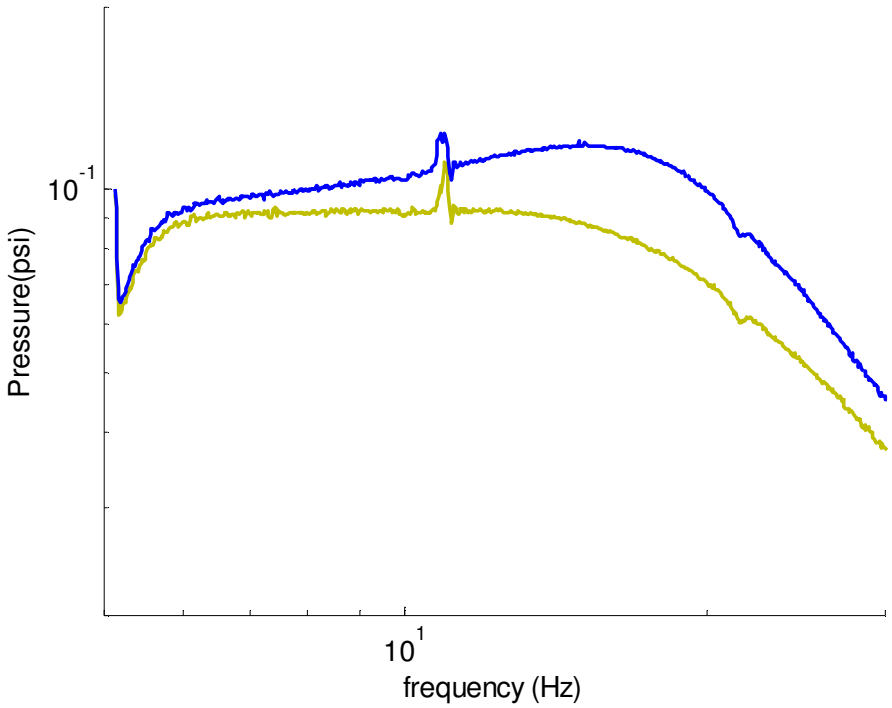

Figure 6-12: Effect of the transfer function resistance variation on the pressure response

6.6 Complex transfer functions effect

The pressure inside the active compliance chamber can also be controlled by means of a defined second order transfer function. In other words, the chamber pressure response is directly related to the applied current frequency pattern. Here, a current signal, similar to the pressure frequency response of the hydraulic bushing pumping chamber (quadratic functions in both the numerator and denominator), is used as an input transfer function, that is

$$T_4 = \frac{0.3s^2 + 2s + 1100}{0.3s^2 + 3s + 1200}. \qquad (6.27)$$

This transfer function has a quadratic function in both the numerator and denominator. According to the transfer function, the pressure frequency response is supposed to be a straight line at low frequencies. Since the notch frequency of the

numerator second order polynomial is smaller than that of the denominator one, the frequency response should gradually increase to that of the notch frequency of the numerator. The maximum amplitude, which depends on the coefficient of s in the denominator, happens at this notch frequency. Finally, at high frequencies, the pressure response continues as a constant. The pressure frequency response for (6.27) is portrayed in Figure 6-13.

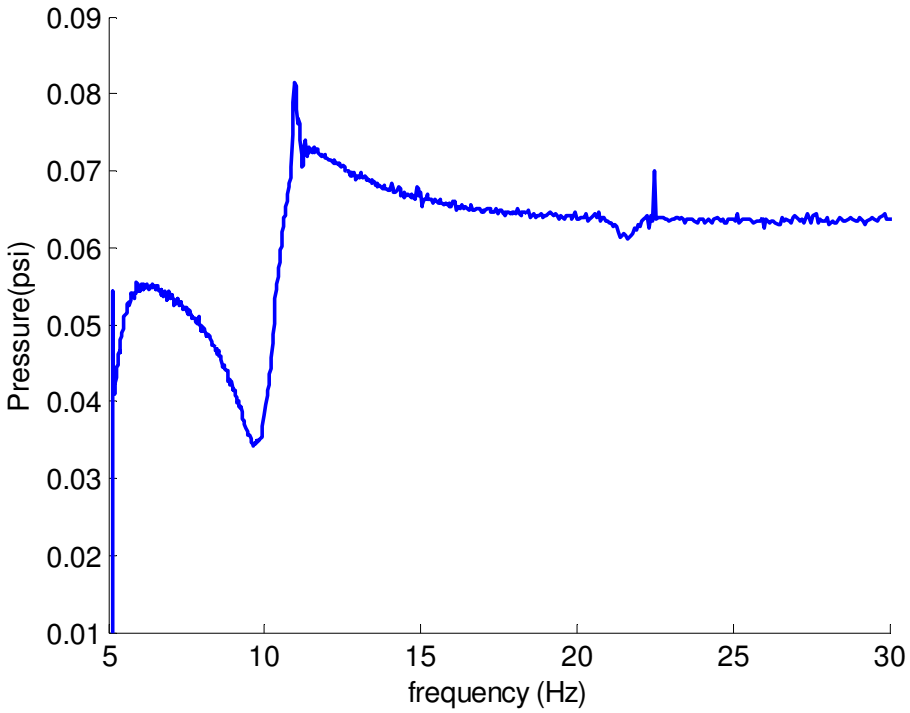

Figure 6-13: Active chamber pressure response to transfer function similar to P_1

The pressure frequency response in Figure 6-13 is qualitatively identical to the pressure frequency response of the pumping chamber of the hydraulic bushings. In fact, the notches in the dynamic stiffness curve exist as a result of the pressure frequency response of the pumping chamber. The adoption of the active compliance chamber and control of the pressure signature results in shifting the dynamic stiffness notches to higher frequencies. Therefore, the soft region of the dynamic stiffness response includes a high

frequency region which is the main goal of the isolator design for VDE systems. The notch frequency shifting of the pressure frequency response is illustrated in Figure 6-14 for different current transfer functions.

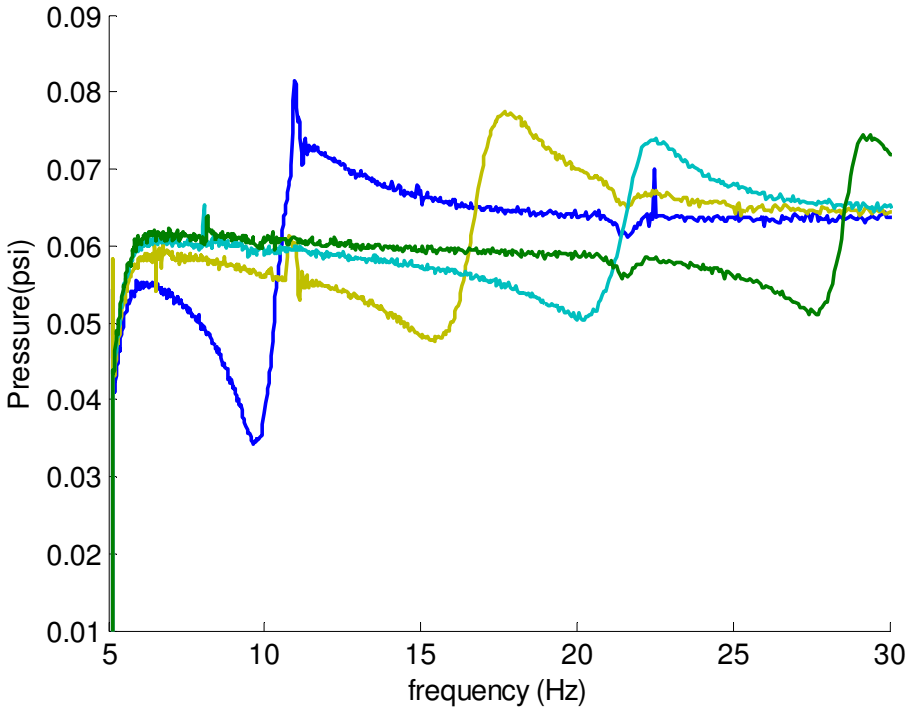

Figure 6-14: Pressure response frequency shift

The amplitude of the pressure response is controlled easily by varying the input current gain. Figure 6-15 displays the response for the same transfer function with different gains. In addition to the current gain, a proper selection of the elastomer diaphragm, in addition to the permanent magnet size and its magnetic property, can boost the response amplitude. The solenoid coil property and its size affect the forcing quality, and consequently, the pressure amplitude. Also, an optimum distance between the permanent magnet and the solenoid coil can also be found by a quantitative analysis and simulation of the magnetic force, the permanent magnet equation of motion, and considering the system nonlinearities.

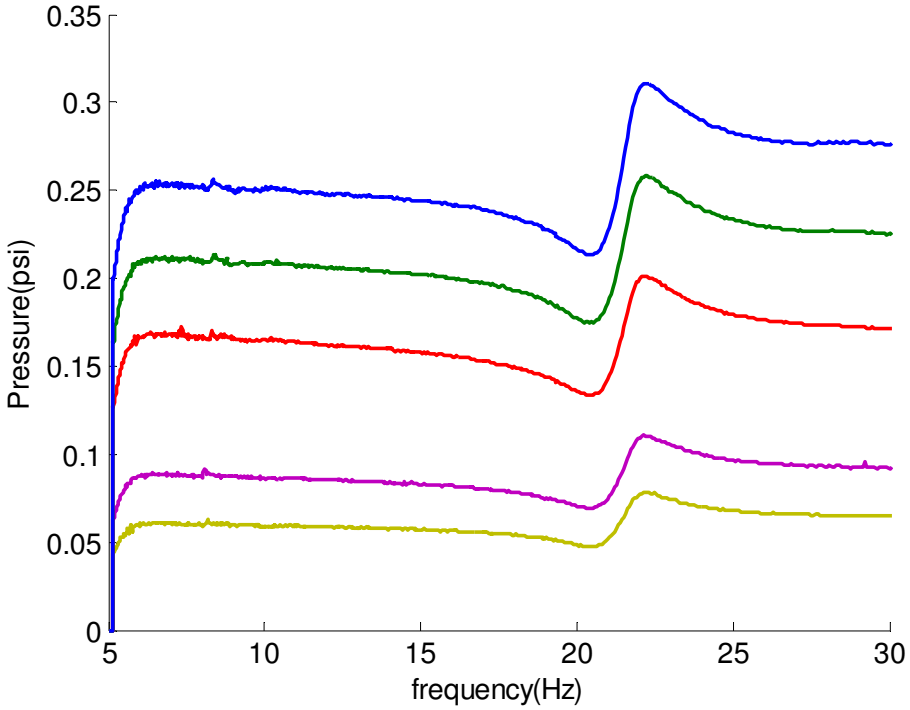

Figure 6-15: current gain effect on the pressure response amplitude

Finally, the peaks of the active chamber pressure frequency response are controlled by defining a proper velocity gain, s coefficient, in both the numerator and denominator. The following transfer functions are used to experimentally clarify that phenomenon,:

$$T_5 = \frac{0.3s^2 + 4s + 5000}{0.3s^2 + 4s + 5200} \qquad (6.28)$$

and

$$T_6 = \frac{0.3s^2 + 3s + 5000}{0.3s^2 + 3s + 5200}. \qquad (6.29)$$

From (6.28) and (6.29), the velocity gains in T_5 are higher than those in T_6. As a result, higher peaks are expected in the pressure response with the current transfer function of (6.29) . The experimental results are summarized in Figure 6-16.

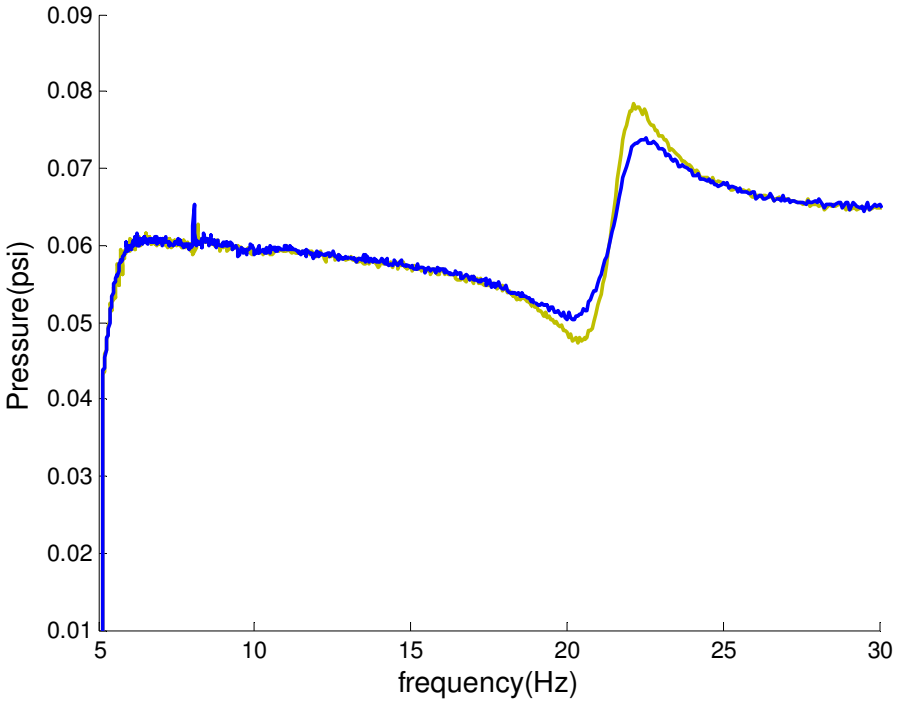

Figure 6-16: Effect of velocity coefficient on the pressure response notch frequencies amplitudes

6.7 Summary

In this chapter, a magnetic actuator is designed to produce the frequency dependent pressure response. This actuator consists of a permanent magnet and a solenoid coil. The equation of motion for the permanent magnet is derived and linearized at the equilibrium point. Also, a magnetic shaker serves to produce the feeding signal to the solenoid coil. The displacement, velocity, and acceleration sweep sine excite the magnetic actuator. It is shown that the pressure frequency response follows the input signal linearly. The amplitude and phase differences of the various current input sources are then employed to create the required pressure frequency response by producing the desired transfer function in the applied current to the solenoid coil. Additionally, it is shown that the notch frequencies of the pressure response can be shifted by changing the notch frequencies in the current transfer function. Then, the effect of the current gain on

the amplitude of the pressure response is studied. The velocity term coefficient is applied to control the peak amplitude at the notch frequencies. The active compliance chamber proves to be a versatile device for controlling the pressure in the frequency domain. The effect of this magnetic chamber on the pumping chamber pressure is investigated in the next chapter.

Chapter 7: Pumping Chamber Pressure Control

An active chamber is designed in Chapter 6 to control the pressure in the pumping chamber of the hydraulic bushing. The magnetic actuator (a combination of a solenoid coil and a permanent magnet) is employed to derive the active chamber. An electrical current based on the displacement, velocity, and acceleration of the bushing is the source of power for the solenoid coil. The experimental results of the pressure frequency response of the active chamber are in an excellent match to those of the feeding signal.

In this chapter the effect of the active chamber on the pumping chamber pressure response is scrutinized. The active chamber is connected to the hydraulic bushing. Similar to the procedure for the previous chapter, different current inputs are used, and the pressure frequency response of the pumping chamber is measured.

7.1 Active Hydraulic Bushing and the Mathematical Modeling

As discussed in Section 3.1, the rubber stiffness and damping in addition to the pressure inside the pumping chamber, significantly affect the dynamic stiffness performance of a hydraulic bushing. The rubber stiffness and damping are embedded features of the conventional hydraulic bushing and are designed according to the static load and torque considerations of the engine. As a result, a device which can actively control the pressure in the pumping chamber can also alter the dynamic stiffness characteristic, effectively. It is shown in the previous chapter that the newly designed active chamber can successfully change the pressure at any specified frequency.

This chamber is connected to the hydraulic bushing, as shown in Figure 7-1. A schematic model of the active hydraulic bushing assembly is given in Figure 7-2. In this

schematic view, the active chamber is represented by a reciprocal pump with an effective cross-section area Ap_2 which is different from the effective pumping area of the pumping chamber. The active pumping displacement is Y. Also, a compliance chamber is chosen to model the elastic characteristic of the active chamber diaphragm. It should be mentioned here that the internal inertia track of the hydraulic bushing is also blocked from the inside for this experiment. As a result, the only inertia track in the active hydraulic bushing assembly is the short inertia track, connecting the pumping chamber to the active chamber.

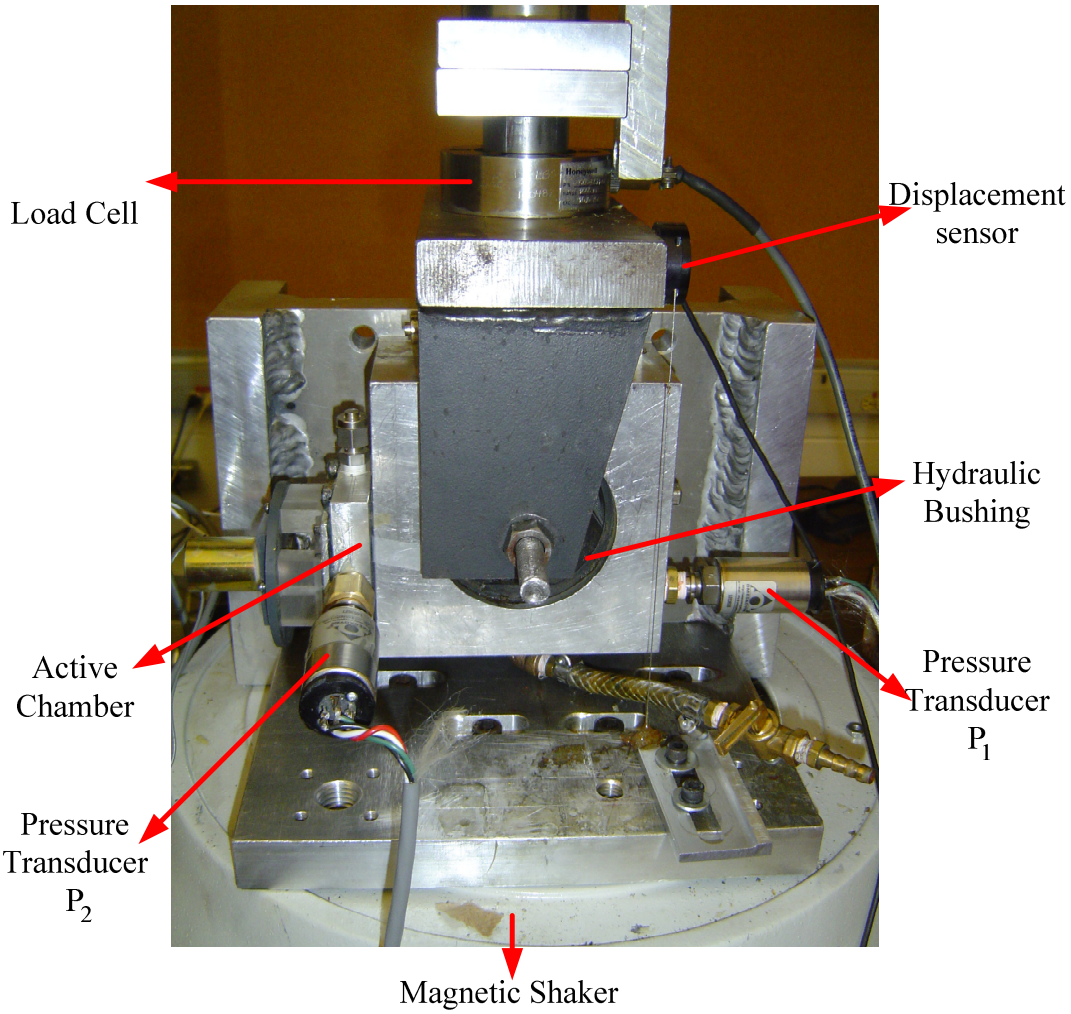

Figure 7-1: Active hydraulic bushing assembly testbed

The continuity equation for the active hydraulic bushing is the same as (3.1) and (3.3) ; however, (3.2) should be rearranged as

$$C_2\dot{P}_2 + A_{p2}\dot{Y} = Q_i \,. \qquad (7.1)$$

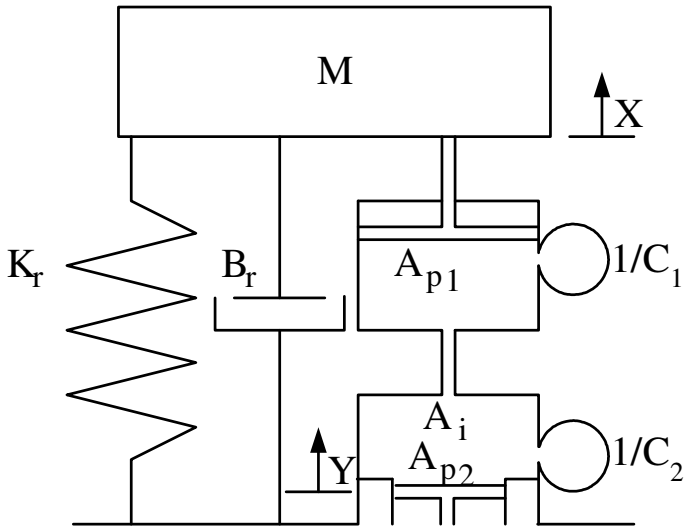

Figure 7-2: Active hydraulic bushing schematic view

By solving (3.1), (3.3) and (7.1) ,

$$P_1(s) = \frac{A_{p1}X(s)(I_iC_2s^2 + R_iC_2s + 1)}{C_1C_2(I_is^2 + R_is + C)} - \frac{A_{p2}Y(s)}{C_1C_2(I_is^2 + R_is + C)} \,, \qquad (7.2)$$

$$Q(s) = \frac{A_{p1}X(s)C_2s}{C_1C_2(I_is^2 + R_is + C)} + \frac{A_{p2}Y(s)C_1s}{C_1C_2(I_is^2 + R_is + C)}, \qquad (7.3)$$

and

$$P_2(s) = \frac{A_{p1}X(s)}{C_1C_2(I_is^2 + R_is + C)} - \frac{A_{p2}Y(s)(I_iC_1s^2 + R_iC_1s + 1)}{C_1C_2(I_is^2 + R_is + C)}. \qquad (7.4)$$

In reality, the active pump acts on the dynamic stiffness curve by producing a pressure difference according to the applied phase. Observing (7.2) , the contribution of the active pump in the pumping chamber pressure is

$$\frac{A_{p1}A_{p2}Y(s)}{C_1C_2X(s)} \frac{1}{I_is^2 + R_is + 1/C_1 + 1/C_2}. \qquad (7.5)$$

In the following sections, the mathematical model of the active hydraulic bushing is validated.

7.2 Pressure Frequency Response of the Pumping Chamber

To practically examine the performance of the active chamber, it is attached to the hydraulic bushing as exhibited in Figure 7-1. Similar to the passive hydraulic bushing compliance chamber, the active chamber pressure transfer function in (7.4) (activation signal $Y(s)= 0$) has a quadratic function in the denominator. A typical asymptotic frequency response of such transfer functions consist of a straight line, which turns into an inclined line at the transfer function notch frequency. In reality, the actual curve produces a peak at the break point. The amplitude of the peak depends on the resistance (first order term coefficient) in the quadratic function. The pressure response of the active chamber, when the input signal is zero is depicted in Figure 7-3. According to the experimental results the notch frequency, occurs at 62 *Hz*. The peak at the notch frequency is relatively high, because the short inertia track can not apply much resistance to the flow motion.

The phase response of the active chamber is also offered in Figure 7-3. Similar to the typical quadratic function in the denominator, the phase should be shifted from 0° to 180°. This transition takes place at different frequency ranges, depending on the damping factor. However, at the system notch frequency, the phase should be 90°. This experimental result validates the pressure transfer function of the active chamber. Since the ultimate goal is to control the pressure inside the pumping chamber, the focus of the following experiment is on the pressure frequency response of the pumping chamber.

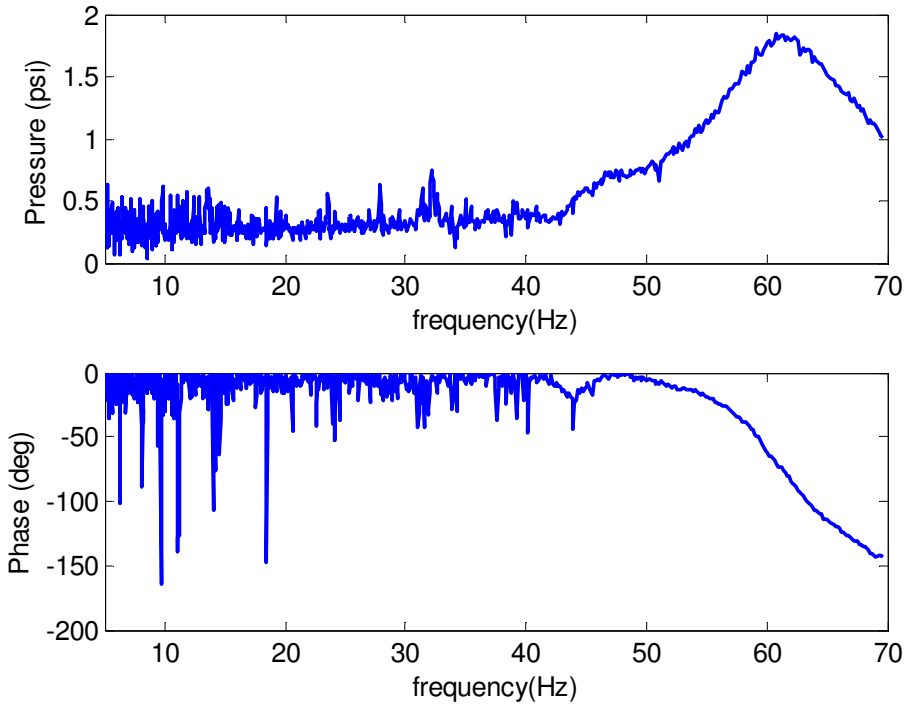

Figure 7-3: Active chamber pressure frequency response

The pumping chamber's pressure transfer function of the assembly in (7.2) has two terms. The first term consists of quadratic functions in both the numerator and denominator, whereas the second term has only a quadratic function in the denominator. Since all the coefficients in the first term of the pressure transfer function of the assembly belong to the original hydraulic bushing; the term is called the hydraulic pressure term. The effect of the active pulses on the bushing assembly is denoted by the permanent magnet displacement transfer function *Y(s)* in the second term of the pressure transfer function.

The hydraulic term of (7.2) has a quadratic function in both the numerator and denominator. Thus, the pressure frequency response of the original hydraulic bushing (without the active component) should have two notch frequencies at the natural frequencies of the quadratic functions of the hydraulic term. The natural frequency of the

quadratic function of the numerator is less than the one in the denominator ($C_1 << C_2$). Consequently, the pressure frequency response asymptote should be a straight line at the beginning, an inclined line at the numerator notch frequency, and finally, a straight line at the denominator notch frequency. The high frequency pressure response is a straight line due to the fact that the positive and negative slopes at the numerator and denominator cancel each other out at the denominator (second) notch frequency. The pressure frequency response of the active hydraulic bushing assembly is plotted in Figure 7-4. This experimental analysis is performed for the no current case to the active component. As a result, the active term in (7.2) is zero.

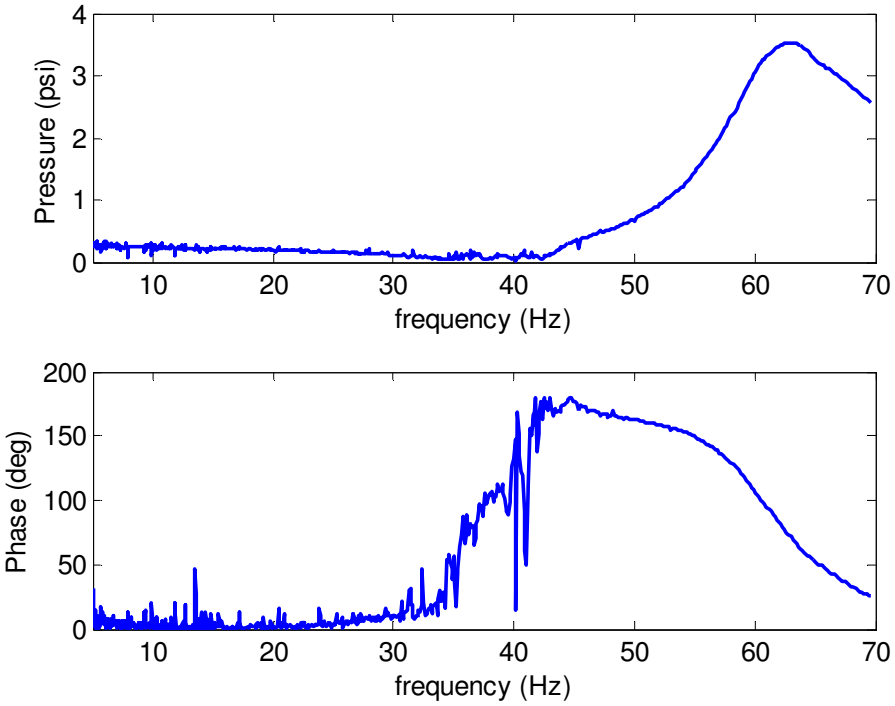

Figure 7-4: Pumping chamber pressure frequency response

According to the experimental results the notch frequencies occur at 37 *Hz* and 62 *Hz*. The peak, associated with the frequency response at the notch frequencies, is the result of the resistive force produced by the inertia track. This resistive force appears as

the coefficient of the first order terms in the quadratic functions, *R*. It is noteworthy that the higher resistive force lowers the peak amplitude.

Moreover quadratic functions have phase shifts with the hydraulic bushing displacement. For the quadratic function in the numerator, which happens earlier, the phase shift asymptote is 180˚. The start and completion of the actual phase shift curve depends on the damping coefficient of the quadratic function. However, the phase shift at the notch frequency is 90˚ for all the damping coefficients. The same occurs for the quadratic term phase shift in the denominator with the negative values. The phase response of the pressure frequency response is also depicted in Figure 7-4. This response also matches the mathematical model in (7.2). Although some noises exist in the phase response at low frequencies, the phase shift of the pressure response to the bushing displacement is almost zero. The 90˚ phase shift takes place at 37 *Hz*, and the 180˚ completes approximately at 42 *Hz*. The phase shift which corresponds to the denominator quadratic function begins approximately at 50 *Hz*. The -90˚ phase shift occurs at 62 *Hz*. The phase shift returns to 0˚ the frequencies higher than 70 *Hz*. The wider frequency range for the denominator phase completion, which is due to the smaller amount of the damping, corresponds the high peak in the pressure frequency response. The experimental pressure response proves the validity of the hydraulic term in (7.2).

Different preliminary feeding signals such as the position, velocity, and acceleration of the shaker are adopted to check the conformity of the response with the input current, and also to validate the mathematical model of this active component; that is, the active term in (7.2).

First, the effect of the displacement feeding on the pressure frequency response of the hydraulic bushing is investigated. According to (7.2), if the two terms of the pumping chamber pressure transfer function is combined, the position feeding has an impact on the constant coefficient of the quadratic function in the numerator of the hydraulic term of the pressure frequency response. The first notch frequency is the natural frequency of the numerator of the hydraulic term. Therefore, by increasing the constant, the first notch frequency of the resultant system should move to the right (higher frequencies). The experimental result of the position feeding pressure response is illustrated in Figure 7-5. As expected, the notch frequency is increased from 37 *Hz* to 45 *Hz*.

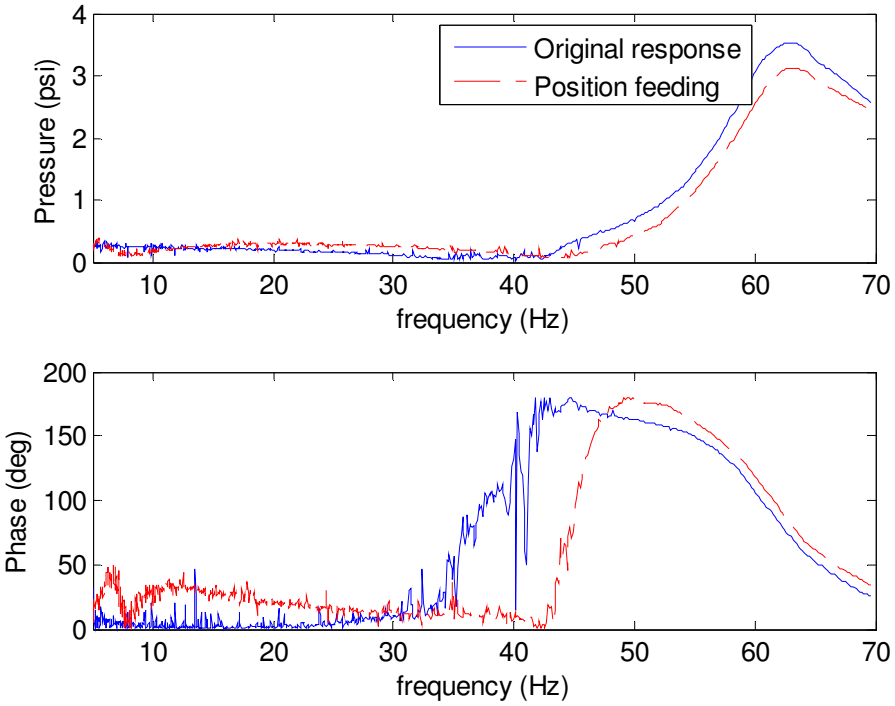

Figure 7-5: Position feeding effect on the pumping chamber pressure frequency response

The shift in the first notch frequency location is more apparent by observing the phase response in Figure 7-5. Although the position feeding has no direct effect on the resistive force of the inertia track, the position feeding contributes to the damping

coefficient. This can be explained by realizing that increasing the compliance corresponds to higher natural frequency, then with the same amount of the resistance a lower damping ratio is resulted. This phenomenon is observed by comparing the frequency range of the completion of the ascending portion of the phase responses. For the original response, this range is approximately 20 *Hz* and 5 *Hz* for the position feeding response. Eq(7.2) predicts no significant change in the pressure response related to the numerator quadratic function. This confirms to the experimental results, illustrated in Figure 7-5.

Unlike the position feeding, the velocity feeding affects the first order term in the quadratic function of the numerator of the hydraulic term. This occurs because the velocity signal is the first derivative of the position signal, and then the velocity signal Laplace transform appears with an "*s*" in the transfer function. In fact, the first order term in the quadratic transfer functions determines the damping coefficient. Therefore, the damping adjustments can be achieved by tuning this type of feeding. The pressure frequency response of the active bushing is depicted in Figure 7-6.

In the frequency responses of the quadratic functions, the damping coefficient indicates a significant effect at the natural frequencies where the resonance occurs. Since the velocity feeding alters only the damping coefficient in the numerator of the hydraulic term, most of the effect is observed at the first notch frequency; That is, 37 *Hz*. To highlight the effect, the pressure response is depicted from 0 to 1 *psi*. According to the experimental results, the velocity feeding response has a lower peak, compared to the original response of the hydraulic bushing. It should be noted that, as predicted by(7.2),

the velocity feeding does not significantly contribute to the shifting of any of the notch frequencies.

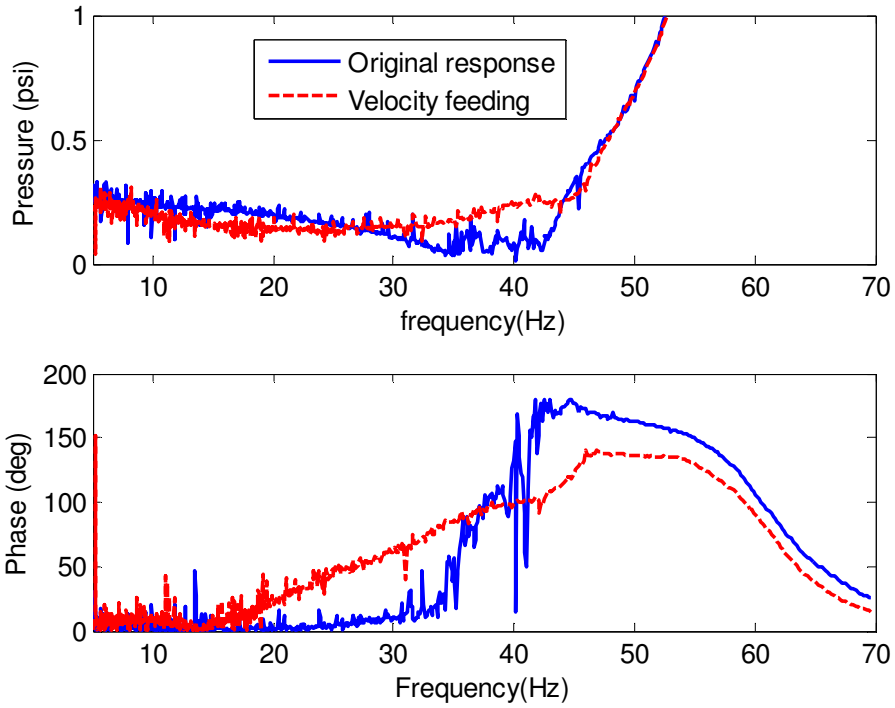

Figure 7-6: Velocity feeding effect on the pumping chamber pressure frequency response

The explanation of the effect of the velocity response on the active hydraulic bushing might be easier, if the phases of the velocity feeding and original responses are compared. According to the phase response of the velocity feeding, the phase shift starts earlier at 15 *Hz*. The early beginning of the phase shift reflects a typical effect of the higher damping coefficient. Like that of the original response, the 90° phase shift which corresponds to the first notch frequency happens at 37 *Hz*. this point can be identified by the intersection of the original and velocity feeding phase responses. Also, there is no significant change in the ascending portion of the phase response which is dominated by the quadratic function in the denominator of the hydraulic term.

The last test signal to validate the active term of the pressure transfer function is the acceleration feeding signal. It is the second derivative of the position signal. Therefore, in a quadratic transfer function, the acceleration feeding impacts on the second order coefficient. As a result, this type of input behaves in contrast to the position feeding; that is, increasing the acceleration feeding amplitude, decreases the natural frequency of quadratic function. The experimental results of the acceleration feeding are illustrated in Figure 7-7.

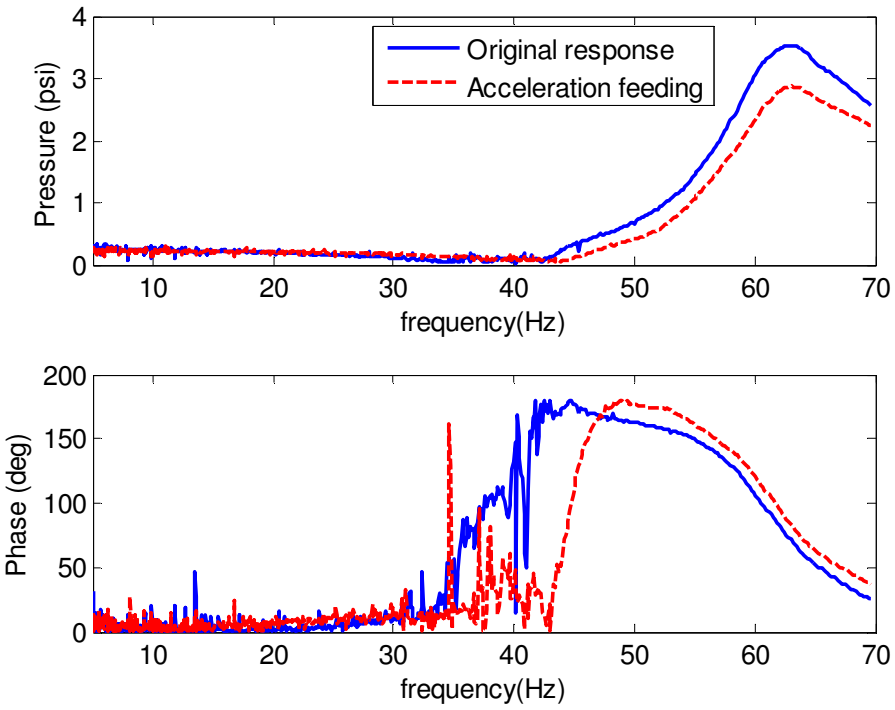

Figure 7-7: Acceleration feeding effect on the pumping chamber pressure frequency response

In this experiment, a negative acceleration signal is used. Therefore, based on (7.2), the first notch frequency should move to the right (higher frequencies). According to the experimental results, the first notch frequency is increased from 37 *Hz* to 44 *Hz*. As expected from(7.2), the second notch frequency location, as well as its corresponding frequency pattern, remaines untouched.

Accordingly, the phase response of the acceleration feeding confirms the prediction of (7.2). For the phase response in Figure 7-7, the 90° phase shift is moved from 37 *Hz* to 44 *Hz*. For the same reason described earlier in Section6.6, feeding experiment, the damping coefficient is affected by the acceleration feeding. Furthermore, this can also be identified in the phase response by comparing the frequency regions that the 180 ° phase shift completes in the original and acceleration feeding responses.

7.3 Complex Transfer Function Feeding

In the previous section, the validity of the mathematical model is confirmed by different experiments. Moreover, the significant capabilities of the active chamber are clarified. In fact, this versatile active chamber not only produces the required pressure differences, but also provides the phase shifts, based on the input signal type. As a result, different features of the original pressure response signature, such as the notch frequencies locations and the damping coefficients, are easily altered by adjusting the position, velocity, and acceleration signals to the solenoid coil. The frequency dependent feature of this active chamber can be used to create complex pressure frequency responses from the active hydraulic bushing assembly. As a beginning, the following transfer function is used to feed the electrical current to the solenoid coil:

$$Tf_1 = K_{amp} C_2 (3Is^2 - Rs - 1)\,. \qquad (7.6)$$

where K_{amp} is the amplification constant used for the input current. Tf_1 is composed of an acceleration signal which is three times of the inertia track size, the velocity and a negative position signal. This combination of signals and coefficients allows the first notch frequency to shift to the left (lower frequencies) according to the ultimate possible electrical current of the solenoid valve. The resultant quadratic function in the numerator

of the hydraulic term requires large second order coefficients and smaller first order coefficients and constants. Consequently, the natural frequency of the quadratic function in the numerator decreases. The experimental results are compared to the original response in Figure 7-8.

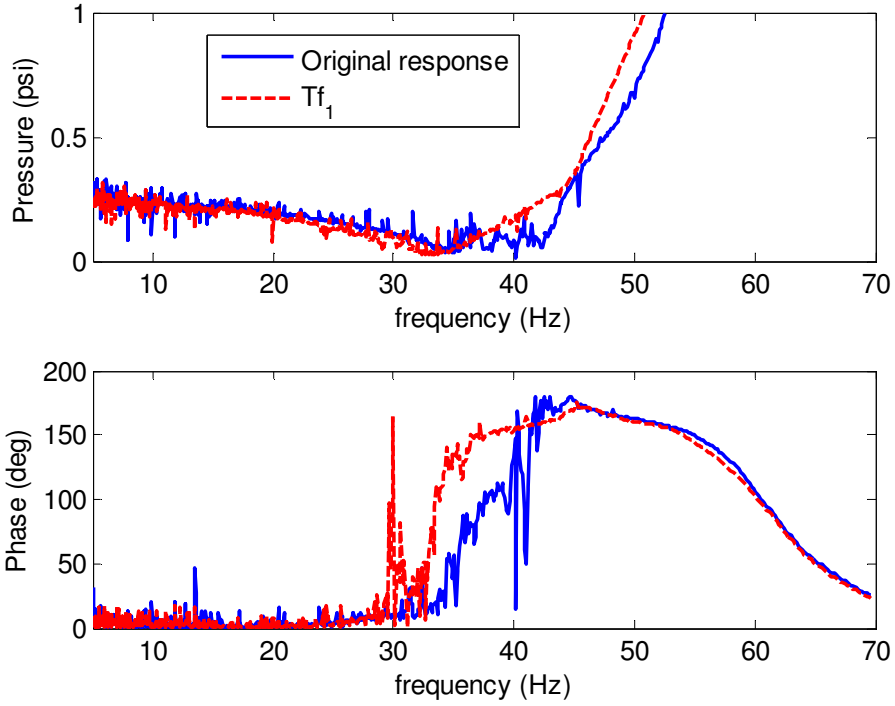

Figure 7-8: Pumping chamber pressure response subjected to Tf_1

To further clarify the effect of Tf_1, the pressure response is displayed in the 0-1 *psi* region. As expected, the notch frequency is moved from 37 *Hz* to 33 *Hz*. This frequency shift can be identified more clearly by observing the phase response. The 90˚ phase shift in the Tf_1 response occurs at 33 *Hz*. Another interesting feature of Tf_1 which can be understood from the phase response, is the reduction in the damping coefficient. The phase shift transition from 0˚ to 180˚ transpires in a small frequency region of 5 *Hz* (from 30 *Hz* to 35 *Hz*).

Also, the use of the active chamber affects the pressure frequency response in the frequencies, other than the region dominated by the two notch frequencies of the original response of the hydraulic bushing. This capability demonstrates its significant importance in cases, where complex pressure response patterns (finally affects the dynamic stiffness as well) are required. In the automobile application, this situation occurs at the resonance frequency of the engine (usually at 10-15 *Hz*), where high damping is required. Obviously, the passive hydraulic bushing can not deal with the VDE isolation problem and the engine resonance frequency at the same time. For example, the following transfer function is used to affect the pressure response in the 20-30 *Hz* region,

$$Tf_2 = \frac{0.6s^2 + 12s + 8000}{0.3s^2 + 10s + 10000}. \qquad (7.7)$$

This transfer function has two notch frequencies at 18 *Hz* and 29 *Hz*. The low frequency response of this function is 0.8, whereas the high frequency response is 2. The frequency response of Tf_2 is depicted in Figure 7-9.

Then, the electrical current is fed to the solenoid coil, based on the Tf_2. The pressure response of the active bushing affected by this input is compared to the response of the hydraulic bushing in Figure 7-10. If the two graphs are compared, two new notch frequencies are added to the existing notch frequencies of the hydraulic bushing at 25 *Hz* and 31*Hz*. These are not exactly the same as the notch frequencies of Tf_2. This is due to the hydraulic term of the pressure response of the assembly in (7.2), contributing to the location of the notch frequencies imposed by the active chamber.

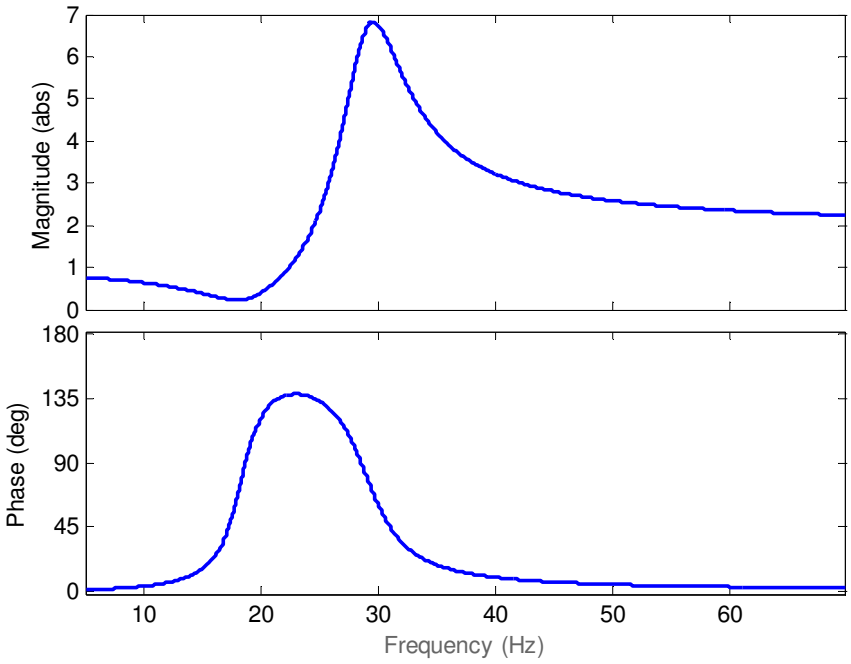

Figure 7-9: bode plot of Tf_2

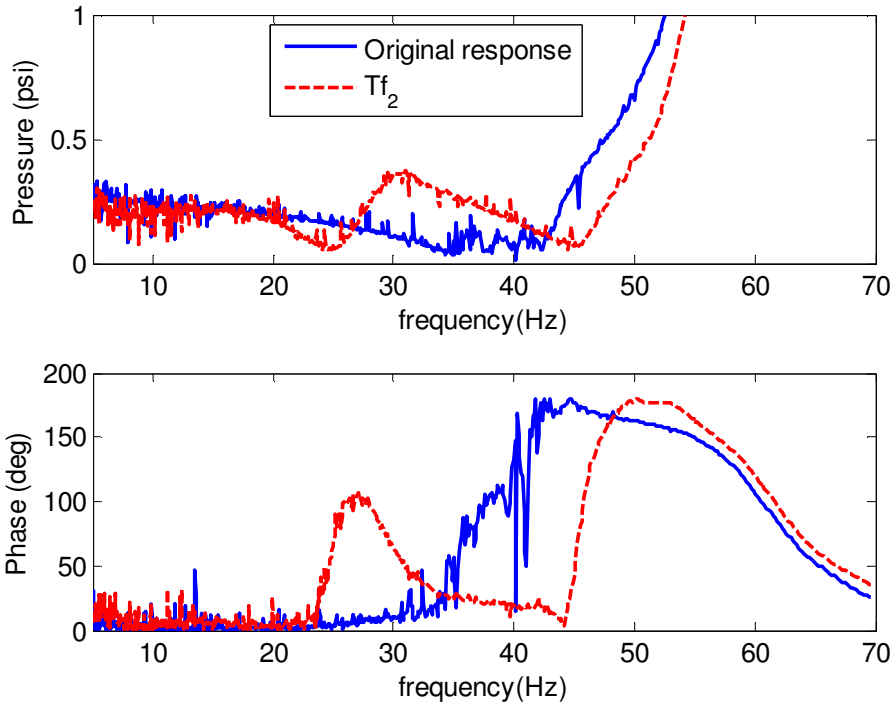

Figure 7-10: Pumping chamber pressure response subjected to Tf_2

The phase response of the Tf_2 feeding agrees with the pressure frequency response. According to the experimental results, the first notch frequency of the original response is also affected by Tf_2. To explain such a shift, it should be noted that the Tf_2 transfer function has a constant value for the frequencies below and above the frequency range, dominated by Tf_2's notch frequencies. This constant for the higher frequencies approaches 2. Thus, in the range of the frequencies of the original response, the active chamber functions as a position feeding signal.

The active chamber can also be fed in a way to create even more complex pressure responses. In fact, the feeding signals, based on the transfer functions, dictate the pressure response signature. To show this capability, the following transfer function, in addition to Tf_2, is adopted to shape the feeding signal:

$$Tf_3 = \frac{(0.6s^2 + 5s + 2000)}{(0.3s^2 + 5s + 3000)}. \qquad (7.8)$$

The notch frequencies of Tf_3 take place at 9 Hz and 16 Hz. According to Tf_3, the low and high frequency values of this transfer function should be 0.7 and 2, respectively. The Bode plot of Tf_3 is denoted in Figure 7-11.

The pressure response of the new set of feeding signals is exhibited in Figure 7-12. In the experimental results, the two new additional notches resulted from Tf_3 are easily identified. Similar to those of Tf_2, the new notch frequencies happen at 15 Hz and 19 Hz. As explained earlier in this section, this shift is a result of the other transfer functions contributions to the resultant active bushing pressure response. In reality, the notches produced by Tf_2 are also slightly affected by Tf_3. The shift in the original response notch frequencies occurs for the same reason as that explained for Tf_2. It should also be

noted that in addition to the notch frequency creation, the corresponding damping can be adjusted by varying the first order coefficient in the desired transfer function.

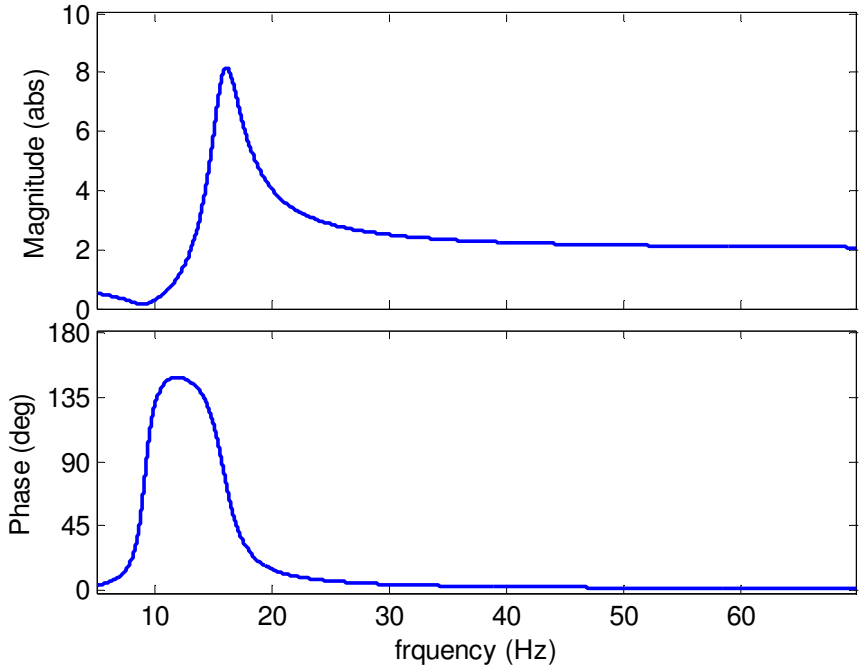

Figure 7-11: bode plot of Tf_3

7.4 Conclusions

The active chamber, which is designed in the previous chapter as an additional component to the existing hydraulic bushing, is tested in a practical situation. Also, the active hydraulic bushing assembly is modeled in this chapter. It is demonstrated that the pressure response of the assembly consists of the hydraulic term which inherits its dynamic behaviour from the existing hydraulic bushing. The other term of the pressure response is called the active term. The mathematical model is validated by elementary experiments. Different features of the original pressure response of the hydraulic bushing, such as the notch frequency location and damping coefficient are altered by the appropriate signal feeding to the active chamber. Moreover, the active chamber

successfully imposes the transfer functions of the input signal on the original pressure response of the hydraulic bushing. This capability is required, since the engine resonance requires more damping. The effect of this active chamber on the dynamic stiffness response is the subject of the next chapter.

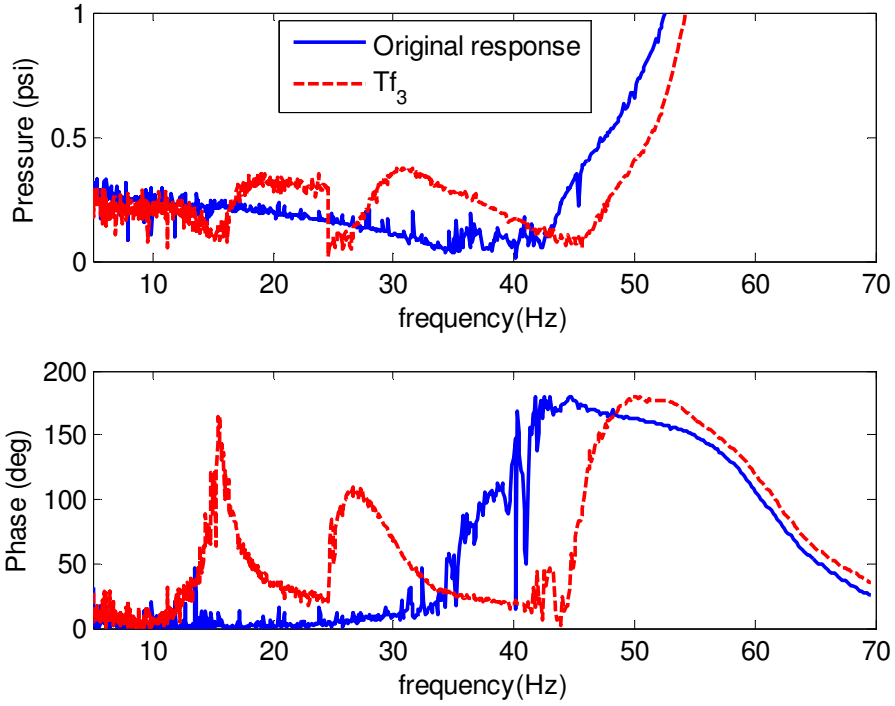

Figure 7-12: Pumping chamber pressure response subjected to Tf_2

Chapter 8: Active Hydraulic Bushing Dynamic Stiffness Response

The development of an active chamber for tuning the pressure of the pumping chamber is explained in Chapter 6. As a follow up, this active chamber is connected to the hydraulic bushing and shapes the active hydraulic bushing assembly. The active hydraulic bushing is tested in Chapter 7, where the experimental results demonstrate that the active chamber can affect all the essential performances of the dynamic response in the hydraulic bushing. This includes the notch frequency locations and damping coefficient. In addition, the active chamber can produce the required pressure responses at other frequencies rather than the notch frequencies.

In this chapter the active hydraulic bushing dynamic response is discussed. The literature background explains different experimental results are covered in Chapter 7. Thus, to avoid duplication, a brief discussion, based on the previous chapter, seems to be sufficient.

8.1 Modelling and System Identification

Before the experiments, it is essential to spend time and go over the mathematical model of the active hydraulic bushing. This model eventually helps us explaining the experimental results precisely. Here, the same schematic model in Figure 7-2 adopted and most of the required relations are developed in the previous chapters. The transmitted force from the isolator is given in (3.7). The K_r and B_r coefficients do not change in the active hydraulic bushing. The only variable which needs to be plugged into this formula

is the pumping chamber pressure. The appropriate relation for the active hydraulic bushing pumping pressure is given in(7.2). Thus, the transmitted force is

$$F_T(s) = (K_r + B_r s + A_{p1}(\frac{A_{p1}X(s)(I_i C_2 s^2 + R_i C_2 s + 1)}{C_1 C_2 (I_i s^2 + R_i s + C)} - \frac{A_{p2}Y(s)}{C_1 C_2 (I_i s^2 + R_i s + C)}))X(s) \quad (8.1)$$

and according to the dynamic stiffness detention,

$$K_{dyn} = K_r + B_r s + \frac{A_{p1}^2}{C_1}\frac{(I_i s^2 + R_i s + 1/C_2)}{I_i s^2 + R_i s + 1/C_1 + 1/C_2} - \frac{A_{p1}A_{p2}Y(s)}{C_1 C_2 X(s)}\frac{1}{I_i s^2 + R_i s + 1/C_1 + 1/C_2} \quad (8.2)$$

The experimental results of dynamic stiffness response are offered in Figure 8-1. It should be noted that this experiment is performed, when the input to the active chamber is set at zero. Similar to those of the conventional hydraulic bushing, the two notch frequencies are identified in the active bushing dynamic stiffness response. However, due to the short inertia track inside the active chamber, the notch frequencies are moved to higher frequencies. Moreover, the lack of damping is clear, where the peak in the second notch frequencies happens at about 800 *N/mm* (compared to 300 *N/mm* in conventional hydraulic bushings).

To find the coefficient in the dynamic stiffness (8.2), the same curve fitting process as those in Chapter 3 is applied here, as shown in Figure 8-1. The simulation is a perfect match to the experimental data. The different coefficients in the dynamic stiffness equation are tabulated in Table 8-1. Except the inertia track size and resistance, the other coefficients are the same as those in Table 3-1. For the active hydraulic bushing, the small inertia track size and resistance are the consequence of the short inertia track designed in the active chamber.

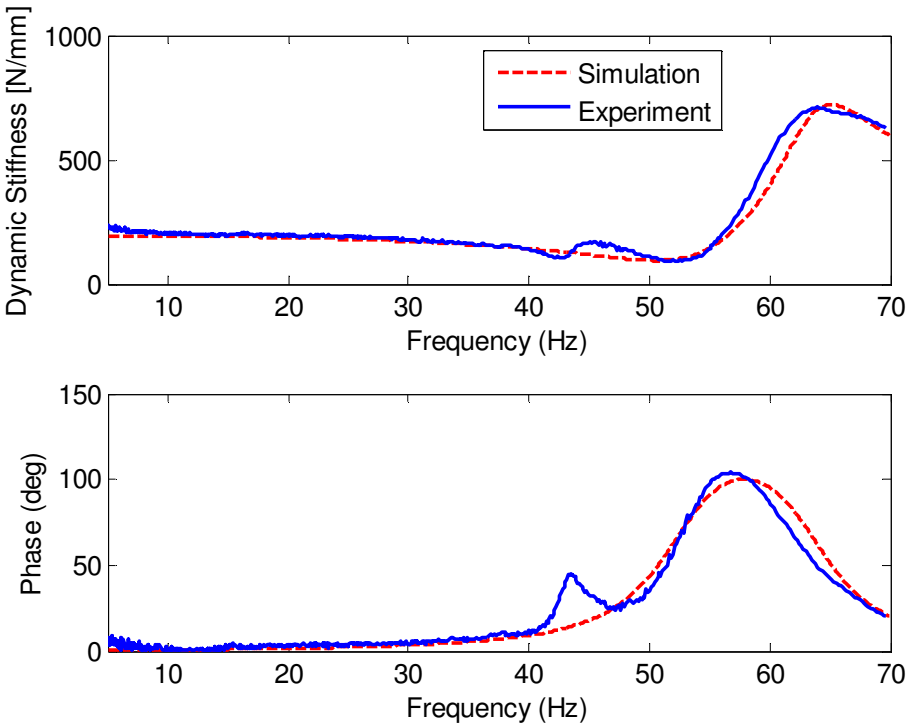

Figure 8-1: Dynamic stiffness response of the active hydraulic bushing and the fitted curve

Table 8-1: Nominal hydraulic bushing parameter values

Symbol	Value	Unit
A_p	14.7	mm^2
B_r	0.1398	N-s/mm
K_r	195.14	N/mm
C_1	2.3709	N/mm^5
C_2	300.99	N/mm^5
I_2	2.66e-006	$N\text{-}s^2/mm^5$
R_2	1.5e-004	$N\text{-}s/mm^5$

8.2 The Elementary Inputs

In Chapter 7, the pressure response of the pumping chamber is examined by varying the current input to the solenoid coil according to the displacement, velocity and

acceleration of the bushing. For a preliminary investigation, the same inputs are adopted in this section. For each current input source, a simulation is performed, according to the coefficients found by curve fitting. The simulation results are then compared to the original response to discuss the improvements.

First, the displacement input effect is investigated. Therefore in(8.2),

$$Y(s)/X(s) = K_{position} \ . \qquad (8.3)$$

By substituting (8.3) into (8.2),

$$K_{dyn} = K_r + B_r s + \frac{A_{p1}^2}{C_1} \frac{(I_i s^2 + R_i s + (1/C_2(1 - A_{p2} K_{position} / A_{p1}))}{I_i s^2 + R_i s + 1/C_1 + 1/C_2} \ . \qquad (8.4)$$

As a result, this kind of current input signal alters the constant in the denominator of the dynamic stiffness equation. In the conventional hydraulic bushing the numerator constant is related to the stiffness of the compliance chambers which defines the location of the first notch frequency of the hydraulic bushing. This implies that, by applying a current signal proportional to the bushing displacement, the material property of the compliance chamber is altered. This interpretation makes sense, since, by applying a current proportional to the displacement, the active chamber contributes to the dynamic volumetric capacity of the chamber which is determined by the compliance of the compliance chambers in the conventional hydraulic bushing. Hence, the magnetic pulses in the direction of the bushing displacement indicate a softer compliant material, whereas the opposite results in a stiffer one.

The simulation results of the original response and the response related to the position feeding are compared in Figure 8-2. Both the magnitude and phase simulation results show that the first notch frequency is shifted to higher frequencies. However, as it

is expected, the location of the second notch frequency (the natural frequency of the denominator) remaines untouched.

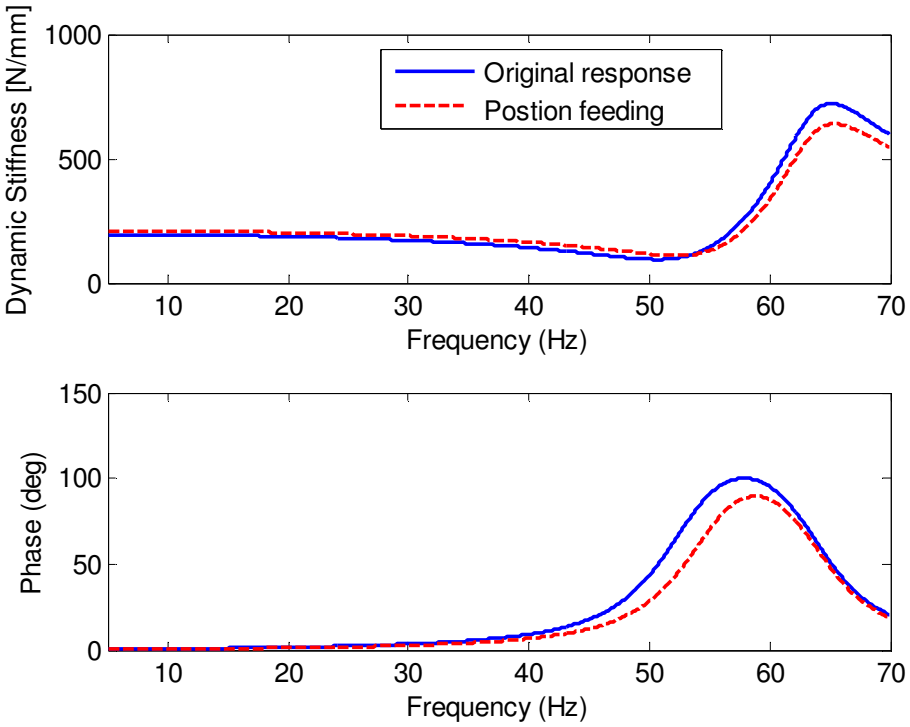

Figure 8-2: Dynamic stiffness response of the current proportional to the bushing position feeding (simulation)

The experimental results of the current signal, proportional to the bushing displacement, are shown in Figure 8-3. A positive electrical current signal is used for this experiment. According to the experimental results, the first notch frequency is moved from 51 *Hz* to 55 *Hz*. Similar to the simulation results, the second notch frequency at 63 *Hz* is untouched. The damping at the first notch frequency is slightly less than that of original response due to the increase of the first notch frequency.

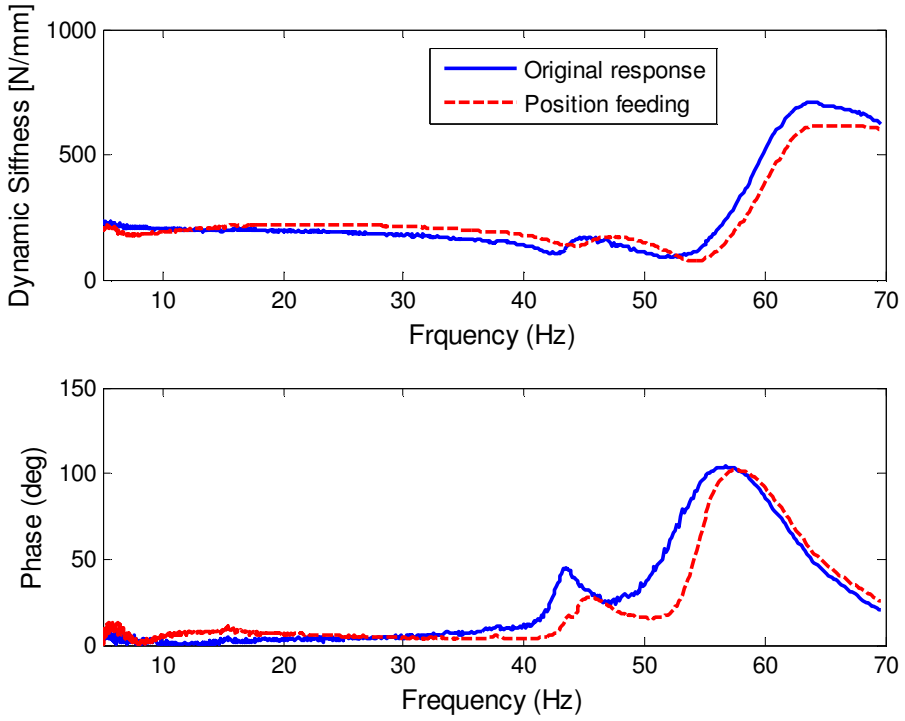

Figure 8-3: Dynamic stiffness response of the current proportional to the bushing position feeding (experiment)

In the second experiment, an electrical current proportional to the bushing velocity is fed to the solenoid coil. The transfer function of this type of current is

$$Y(s)/X(s) = s.K_{velocity} \,. \qquad (8.5)$$

Thus, the dynamic stiffness equation is

$$K_{dyn} = K_r + B_r s + \frac{A_{p1}^2}{C_1} \frac{(I_i s^2 + (R_i - A_{p2} K_{velocity} / A_{p1} C_2) s + 1/C_2)}{I_i s^2 + R_i s + 1/C_1 + 1/C_2} \,. \qquad (8.6)$$

From (8.6), the principal contribution of this type of current signal is to the damping at the first notch frequency. This signal behaves like the MR valve in Chapter 5. In other words, the velocity feeding is equivalent to altering the roughness of the existing short inertia track of the active chamber.

The simulation results of (8.6) is given in Figure 8-4. The dynamic stiffness simulation reveals a smaller peak at the first notch frequency. As expected, none of the

notch frequencies is relocated. Also, the phase responses agree with the theory. The phase shift begins at the earlier frequencies, demonstrating an increase in the damping ratio. It is interesting that the phase responses of the original and the one with the current proportional to the velocity are intersecting at the first notch frequency, whereas the second notch frequency phase responses are almost parallel. This results in an obvious change in the damping at the first notch frequency.

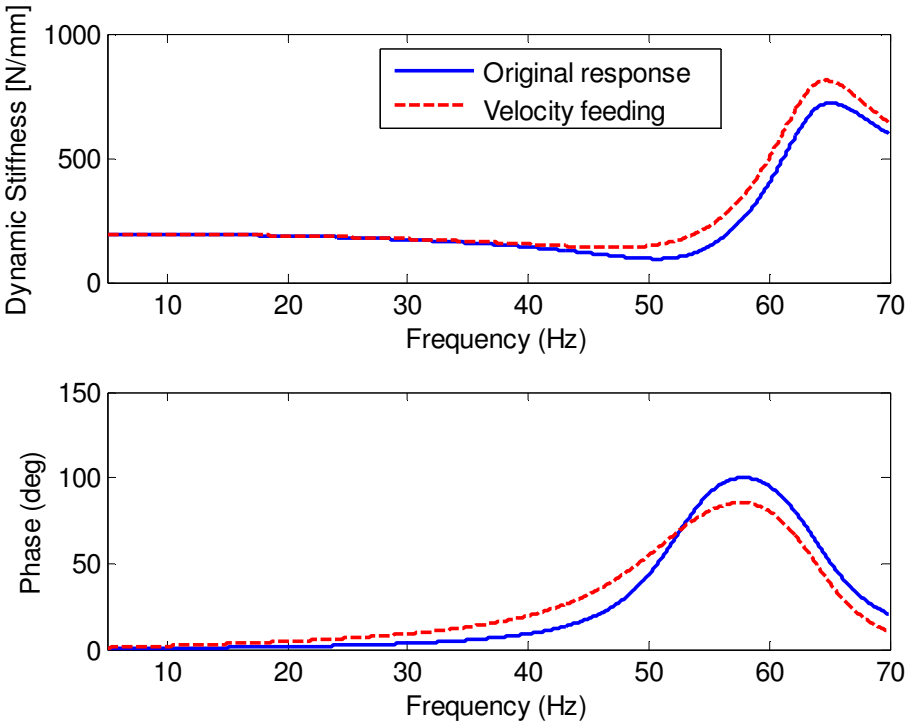

Figure 8-4: Dynamic stiffness response of the current proportional to the bushing velocity feeding (simulation)

Simulink Matlab software is used for producing a current signal proportional to the velocity. The experimental results are reflected in Figure 8-5. The peak of the dynamic stiffness response at 51 *Hz* is reduced from 100 *N/mm* (base is at 200 *N/mm*) to almost 10 *N/mm*. The notch frequency locations are the same for both cases. The phase response also agrees with the mathematical model.

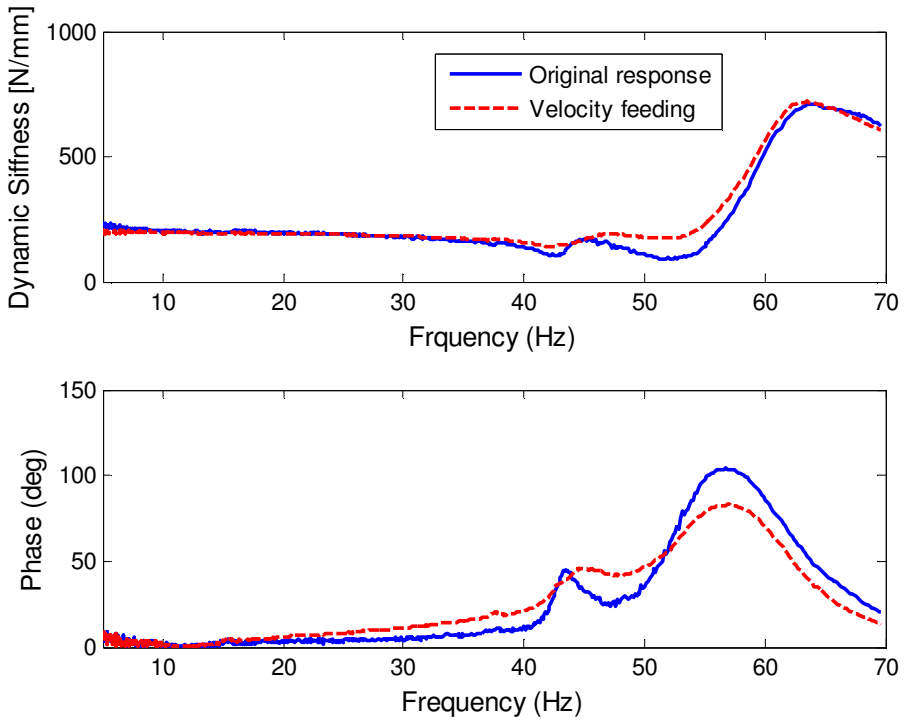

Figure 8-5: Dynamic stiffness response of the Current proportional to the bushing velocity feeding (experiment)

The last elementary current signal which is examined here is the one proportional to the bushing acceleration. The electrical current transfer function for this case is

$$Y(s)/X(s) = s^2.K_{acceleration} \ . \qquad (8.7)$$

By substituting (8.7) into (8.2), the dynamic stiffness transfer function is,

$$K_{dyn} = K_r + B_r s + \frac{A_{p1}^2}{C_1} \frac{((I_{ii} - A_{p2}K_{acceleration}/A_{p1}C_2)s^2 + Rs + 1/C_2)}{I_i s^2 + R_i s + 1/C_1 + 1/C_2} \ . \qquad (8.8)$$

The active chamber for this case affects the inertia track size, indicating that the inertia track size can dynamically be changed. In reality, the active chamber produces such an effect by creating a momentum in the fluid migrating from or to it. If the created momentum is in the direction of the one produced by the pumping chamber, a virtually shorter inertia track results. However, the momentum opposite to the direction of the pumping chamber acts in reverse. In general, the size of the inertia track contributes to

the location of the notch frequencies directly, and on the damping coefficient indirectly. The effect of the inertia track size on relocating the notch frequencies is similar to the effect of compliance. In other words, increasing the inertia track size decreases the natural frequency.

The simulation results of the current input proportional to the acceleration are provided in Figure 8-6, where a negative acceleration signal is employed. According to the simulation, the first notch frequency is moved to the right. As expected, the location of the second notch frequency is not changed.

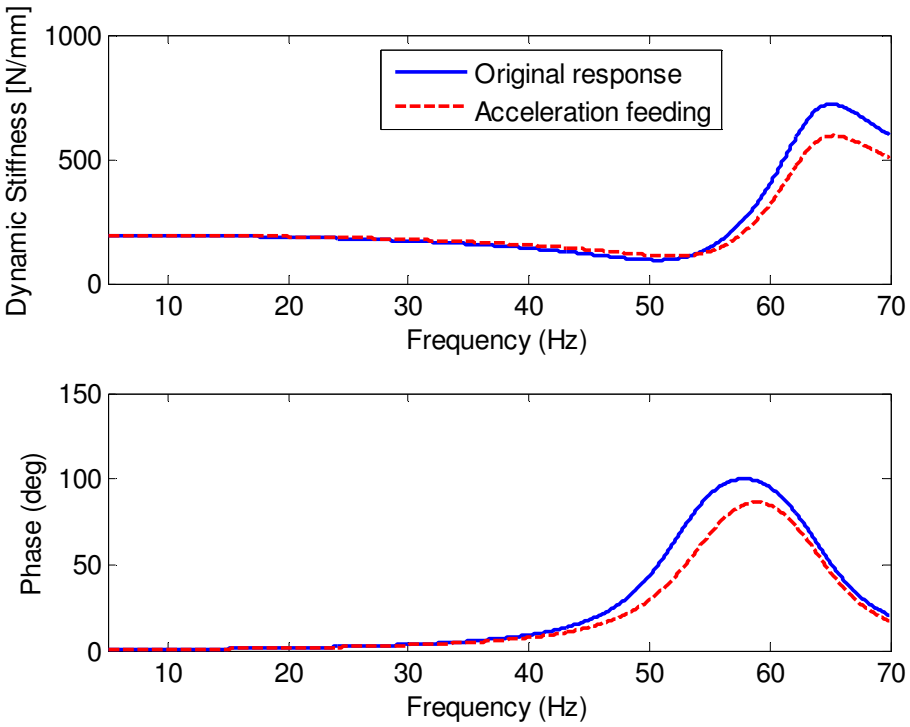

Figure 8-6: Dynamic stiffness response of the current proportional to the bushing acceleration feeding (simulation)

Figure 8-7 portrays the experimental results for this type of input. In this experiment, the location of the first notch frequency is changed from 51 *Hz* to 54 *Hz*. Although the damping changes at this notch frequency might not be visible, the phase response clarifies the change. In fact, the phase response of the original response has a

smaller slope compared to the other phase response which means that the damping is decreased.

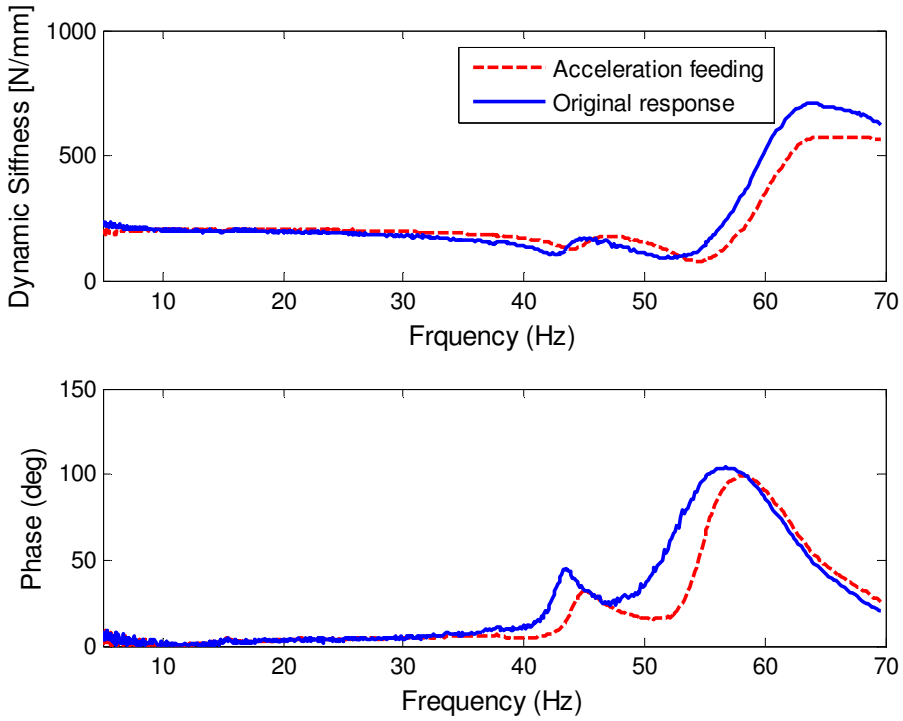

Figure 8-7: dynamic stiffness response of the current proportional to the bushing acceleration feeding (experiment)

8.3 Complex Transfer Function Feeding

Now that the effect of the elementary input signal on the dynamic stiffness response is observed, more complex transfer functions are used to demonstrate significant capabilities of the active hydraulic bushing system. The transfer functions here are the same as the ones in Section 7.3, where

$$Tf_1 = K_{amp} C_2 (3Is^2 - Rs - 1)$$

The first transfer function is Tf_1 in (7.6). So far, all the signals shift the first notch frequency to the right. As explained Section 7.3, Tf_1 moves the pumping chamber pressure to the left. It is expected that Tf_1 performs similarly to the dynamic stiffness

response. Three elementary signals are the components of Tf_1. Based on the coefficients of the different components and the preliminary studies in the previous section, the resultant transfer function should have a longer inertia track, more resistive force to the fluid motion, and less dynamic capacity. As a result, the final isolator is equivalent to the one with a smaller first notch frequency and higher damping.

The simulation results of the Tf_1 feeding are exhibited in Figure 8-8. According to the dynamic stiffness curves, the first notch frequency is moved to the left. As expected, the location of the second notch frequency remains untouched. From the phase response, it is concluded that the damping of the system is reduced. This occurs because the slope of the ascending part of the phase bump in the Tf_1 feeding case is smaller than that of the original response.

The experimental results of the Tf_1 feeding are also given in Figure 8-9, where the experimental results agree with the proposed mathematical model and simulations. In fact, the first notch frequency in the Tf_1 feeding is moved from 51 Hz to 49 Hz. Although this is not clear in the dynamic stiffness response, however it is evident in the phase response.

Similar to the pressure response of the pumping chamber, the feeding inputs can be set to affect the dynamic stiffness response in the frequencies other than the ones located in the two notch frequency regions. This feature gives the isolator the capability to handle more complex vibration disturbances.

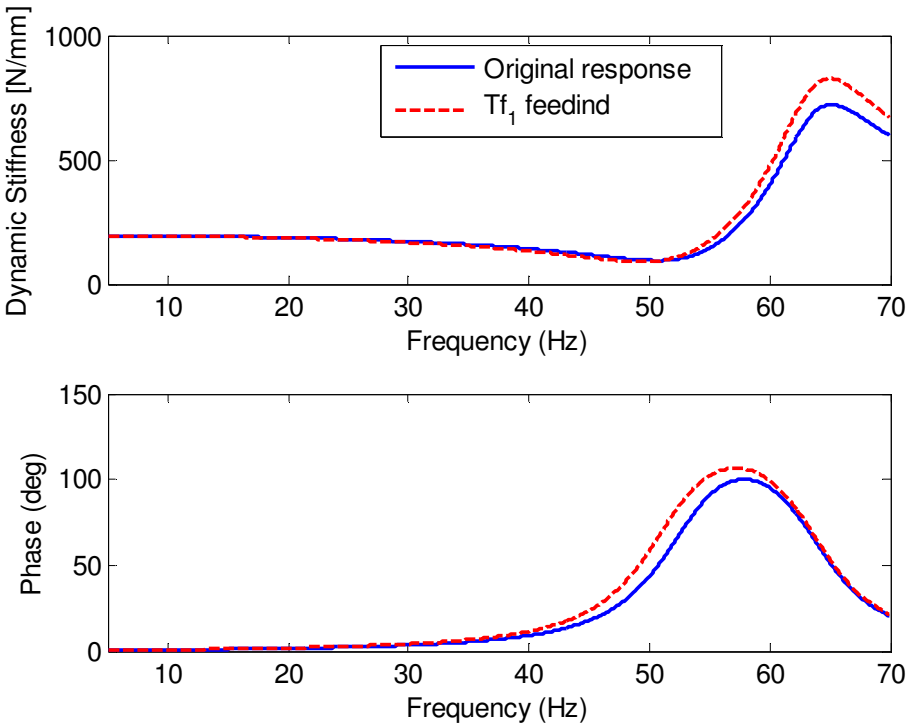

Figure 8-8: Dynamic Stiffness response subjected to Tf_1 (simulation)

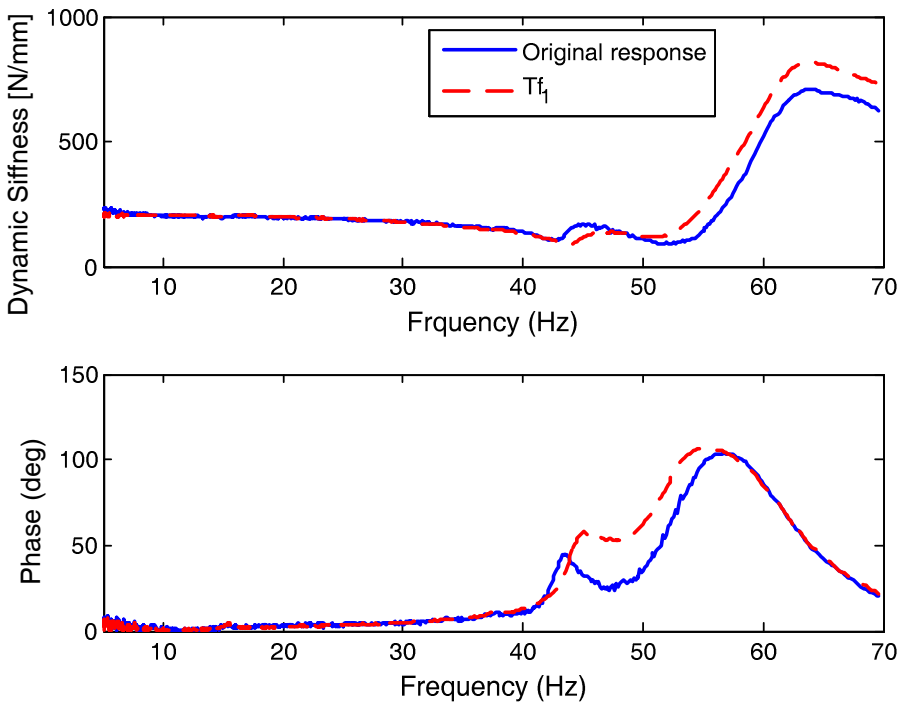

Figure 8-9: Dynamic Stiffness response subjected to Tf_1 (experimental)

To examine such a capability, the same Tf_2 in (7.7) is used. The Bode plot of Tf_2 is given in Figure 7-9. This transfer function has two notch frequencies at 18 *Hz* and 29 *Hz*. The dynamic stiffness simulation results are depicted in Figure 8-10. A new peak appears in the dynamic stiffness response of the system fed by Tf_2. This peak corresponds to a bump in the phase response. Obviously this peak is does not occur at the same frequency region as that of Tf_2. Back to the dynamic stiffness equation (8.2), It can be said that the different components of the equation together and form the final response. That is why the new peaks location are not exactly the same as the actual notch frequencies location of Tf_2. It is also noteworthy that the first notch frequency of the original response moves due to the Tf_2 interaction. In fact, amplifying the input signal magnifies the share of the Tf_2 in the dynamic stiffness transfer function and constrains the peaks close to the Tf_2 notch frequencies.

The experimental results in Figure 8-11 agrees with the simulation results. The notch frequencies of the new peaks are happening at 27 and 31 *Hz*. The reason that the second notch frequency of Tf_2 is almost preserved in the final dynamic stiffness response, is that, mathematically this peak belongs to the denominator of Tf_2, and as a result, remains unchanged in the resultant dynamic stiffness equation. The experimental results of the Tf_2 feeding signal indicates that by tuning the input transfer function parameters, the newly created peaks can be moved to any specified frequencies. The damping coefficients of the active hydraulic bushing at those frequencies can also be set by tuning the term s multiplier in the input signal transfer function. Moreover, even more complex dynamic stiffness responses are achievable by defining the appropriate transfer function for the input signal. To show this capability, the Tf_3 in (7.8) is combined with Tf_2.

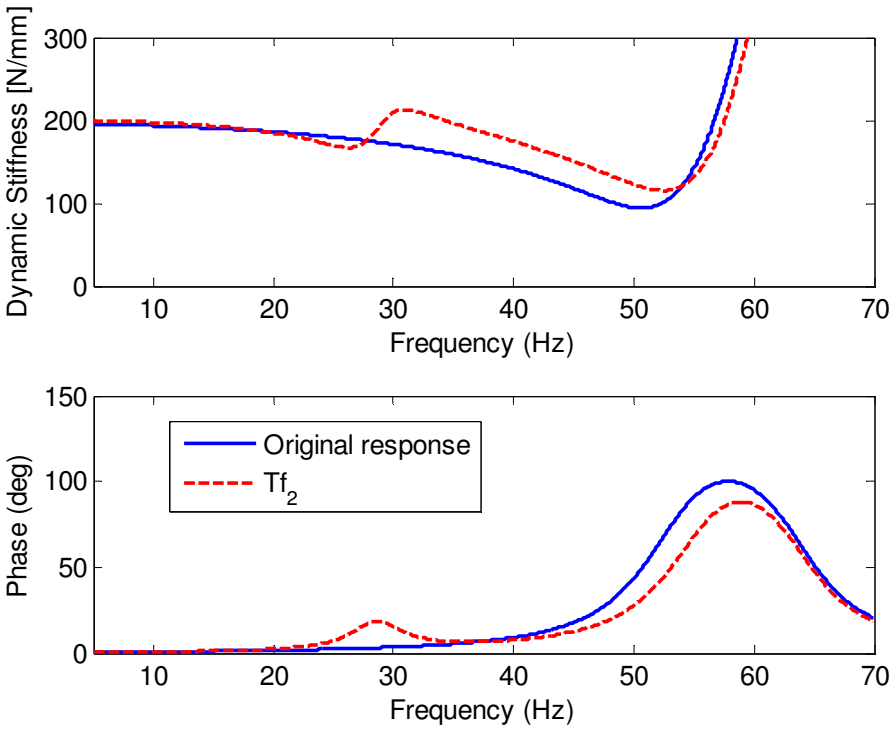

Figure 8-10: Dynamic Stiffness response subjected to Tf_1 (simulation)

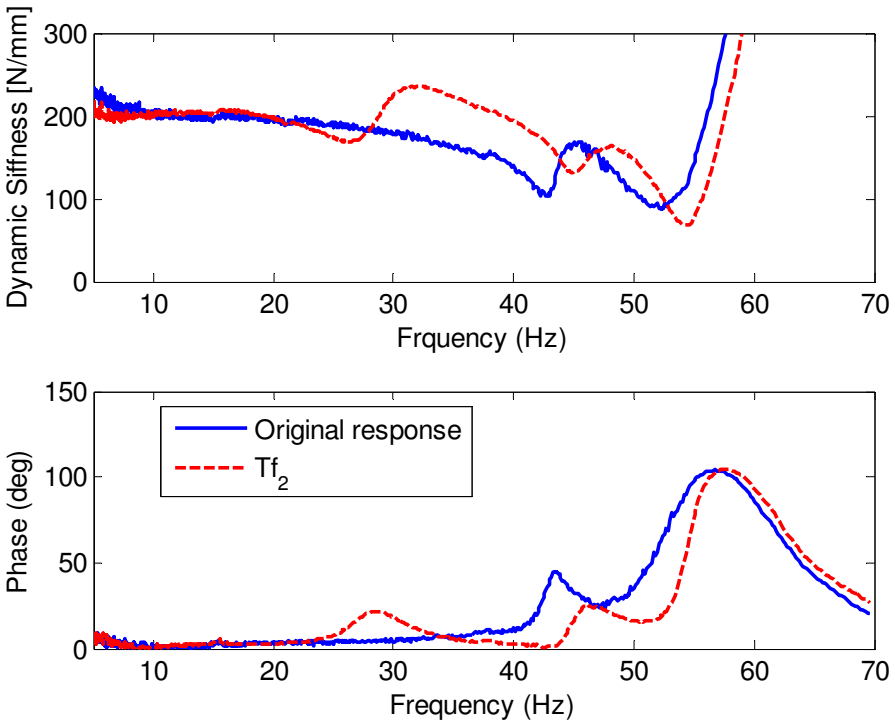

Figure 8-11: Dynamic Stiffness response subjected to Tf_2 (experimental)

The experimental results of this input signal are apparent in Figure 8-12. In the dynamic stiffness, two new notch frequencies appear at 16 and 19 *Hz*, demonstrating that the notch frequencies affect of the Tf_3 in the dynamic stiffness response. The new peaks do not occur at the notch frequencies of Tf_3 for the same reason as that explained for the Tf_2 case.

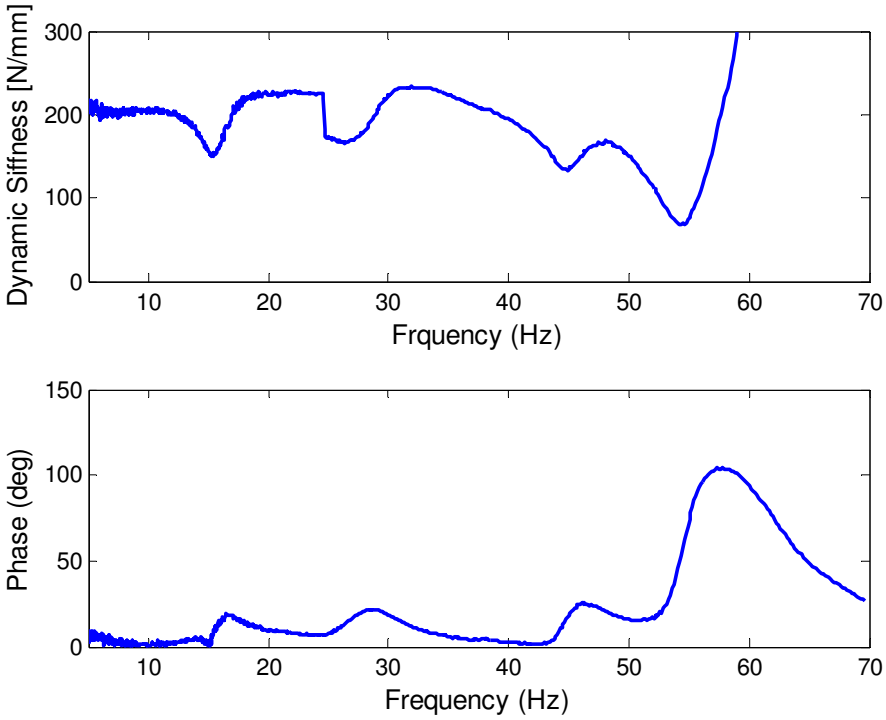

Figure 8-12: Dynamic Stiffness response subjected to Tf_3 and Tf_3 (experimental)

8.4 Summary

The dynamic performance of the active hydraulic bushing is discussed in this chapter. The mathematical model completely matches to the experimental results as that of the Chapter 7. The elementary input signals (proportional to the displacement, velocity, and acceleration) are investigated first. The mathematical model for each case is derived and some predictions are made based on the resultant dynamic stiffness equation. Then, the predictions are validated by the experimental results. It is proved that the

elementary input signals not only relocate the first notch frequency, but also satisfy the required damping at that frequency. More complex signals, derived from the combination of the elementary inputs, are fed to the active hydraulic bushing in the form of transfer functions. It is concluded that the active system can successfully produce a complex transfer function in any required frequency. Thus by the utilization of this active isolator, more complicated vibration patterns can be isolated from or to the engine.

Chapter 9: Design and Fabrication Difficulties

In addition to the design and assembling problems, the nature of the work imposes some other difficulties in preparing the prototype. The air entrapments and the MR-rubber compatibility are among these problems.

9.1 Air Entrapment

Any air bubble inside the bushing introduces another degree of freedom to the system by acting as additional compliance to the bushing dynamic stiffness response. It is because air is a compressible material. In addition, modeling such a compliance is so difficult, since the problem becomes highly nonlinear and function of various parameters such as the air bubble size, location and temperate.

To avoid such a problem the unassembled bushing components are submerged in a basin and then rubber component is press fitted inside the aluminum block. However, in practice even after repeating the process several times the air bubbles are still present, as shown in Figure 9-1. The reason for the air bubble existence in the system is the very narrow MR valve. Actually, the water (or MR fluid) can not provide enough buoyancy for the air entrapped in that valve to leave it.

The other method which is attempted later is to put the bushing the bushing assembly on the shaker. Although this additional remedy works, it was decided to put another hole on the bottom of the bushing and remove the air bubbles by applying a fluid force to make the bubbles leave the MR valve and other places they are entrapped in.

Figure 9-1: Air bubble problem of the prototyped semi-active bushing

9.2 MR- Rubber Compatibility

The other design problem is the rubber and MR fluid compatibility. In practice, the natural rubber swells in the presence of the MR fluid. This phenomenon is observed in the preliminary experiments. Figure 9-2 denotes the defected (right) bushing and a new bushing (left).

Figure 9-2: A healthy hydraulic bushing (left) and a defected bushing with the MR fluid (right)

Since the MR compatibility problem is not solved till the end of this investigation, the best way to deal with the problem is to include different coatings and study the weight increase in each case. In the experiment, the mass of four roughly similar pieces of rubber is measured after they were coated with a special barrier. The coated rubber specimens are submerged in the MR fluid for approximately two weeks, the mass is re-measured to identify which coatings prevent the absorption of the MR fluid. These results illustrate that a silicon coating is superior by only 15% increase of the mass, compared to the control specimen (marked CTRL) which is increased by 30%. Figure 9-3 shows the test specimen and the result of the experiment.

Coating	Orignal Mass (g)	Final Mass (g)	Percent Increase
Silicon	3.00	3.45	15%
CTRL	2.30	3.00	30%
Teflon	2.50	3.40	36%
Primer	2.55	3.16	24%

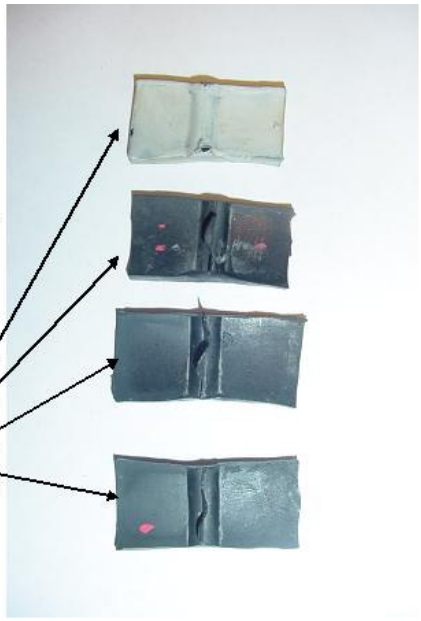

Figure 9-3: Test results of the different coatings for MR compatibility

As the experiment suggests the best choice for the coating is silicon. The other good thing about the silicon coating is that it is very flexible and doses not crack when it is subjected to deflection. Figure 9-4 displays bushing after it is coated.

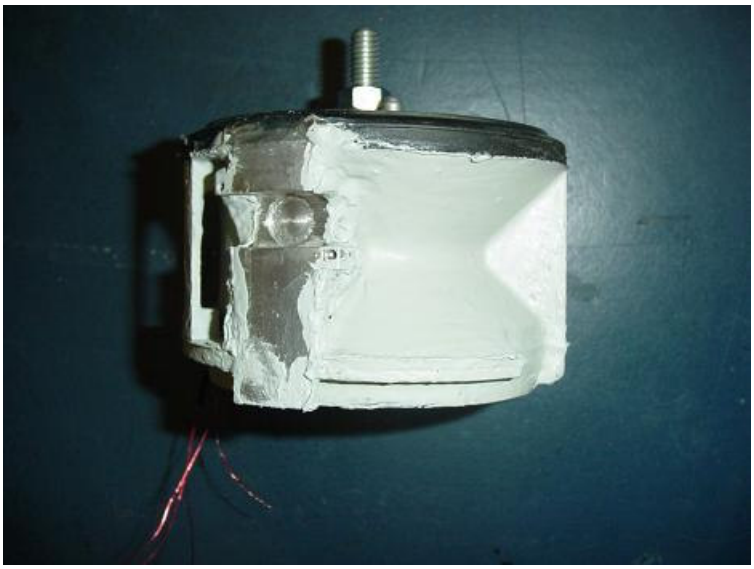

Figure 9-4: The coated Hydraulic bushing with silicon

Chapter 10: Conclusions and Future Work

The purpose of the investigation described in this thesis is to design an isolator for the VDE system. Semi-active or active engine bushings are required to meet the new performance requirements associated with cylinder deactivation engines. When the Engine Control Unit (ECU) changes the number of cylinders firing, the magnitude of the forcing changes. This new situation requires different bushing properties for better isolation. Also, the transient vibrations resulting from the torsional loading during the process of activation and deactivation cylinders need to be better controlled with this isolator. Actually, the VDE systems require a soft isolator for the cylinder deactivation mode. However for normal engine operation, the performance of the existing hydraulic bushings is sufficient. As a result, the goal of this research activity is to design a switchable engine bushing to deal with the normal and cylinder deactivation modes of the engine at the same engine bushing isolator.

In addition, the structure of a conventional hydraulic bushing is discussed in details in this thesis. The rubber property of the hydraulic bushing is a passive parameter. Here, the optimization methods facilitate the selection of the suitable property for the passive components. These optimization techniques need some cost functions, defined by the ideal performance required. Chapter 1 of the thesis deals with the optimization process to find the damping and stiffness of the ideal passive isolator. The force and displacement transmissibility are the cost functions and the RMS technique is applied in both the frequency and time domains. Base excitation, unbalanced forces, and harmonic forces are the cases studied in the optimization process in the frequency domain. For the

base excitation, the simulation results reveal the existence of an optimum damping ratio which minimizes the RMS of the acceleration. Similar to the base excitation, it is found that the harmonic and rotating unbalanced forcing each have an optimum damping ratio which minimizes the RMS of transmitted force. For the time optimization, the step, pulse, and harmonic inputs are used. Although the optimum values of damping are found for some cases to minimize the force and acceleration transmissibility, the results can not be generalized. It is recommended, though, that the RMS optimized parameters in the frequency domain are more reliable since they represent the average of the cost function response.

In addition to the passive rubber block, hydraulic components are the other important aspects of conventional hydraulic bushings. A mathematical model of the entire hydraulic bushing is given in Chapter 3. The dynamic stiffness equation, which is a key factor in designing the isolator, is derived. The hydraulic bushing dynamic stiffness transfer function is validated by performing experiments. The experimental results of the dynamic stiffness response reveal a soft region at low frequencies and a hard region at high frequencies. A conventional hydraulic bushing turns from a soft isolator to a hard one at its notch frequencies. It is evident from the mathematical model that a short inertia track extends the soft region to higher frequencies while a long one limits that frequency region.

Based on the knowledge provided by conventional hydraulic bushing investigations, a short inertia track is employed to extend the frequency region of the soft isolation. The mathematical model for such an isolator is derived in Chapter 4. An experimental test bed is constructed. An external compliance chamber is manufactured to

prove the short inertia track concept. As expected, the dynamic stiffness response of the hydraulic bushing with the short inertia track remains soft for the higher frequencies.

The problem associated with the short inertia track is the low resistance applied to the fluid motion. An MR valve is designed in Chapter 5 to satisfy this critical requirement. The advantage of using MR fluid to create the damping is its minimum interaction with the physical characteristics of the isolator. The design of this MR valve allows an ideal alignment of the iron particles. As a result, even a small electrical current is sufficient to produce the required damping.

The design of an alternative active bushing is also described in this thesis. In designing the active isolator the focus is on tuning the pumping chamber pressure response. Different aspects related to the fabrication and modeling of this active chamber is discussed in Chapter 6. The actuator of this active chamber is composed of a permanent magnet bonded to a flexible diaphragm and a solenoid coil. The equation of motion for the permanent magnet is derived and linearized. The dynamic performance of the active chamber is tested by applying elementary (proportional to the position, velocity and acceleration of the bushing) and complex (transfer functions) current inputs. The experimental analysis confirms that the pressure inside the chamber linearly follows the current input signal.

Chapter 7 deals with the pumping chamber pressure control. First, the active hydraulic bushing is mathematically modeled. The validity of the mathematical model is confirmed by testing the active hydraulic bushing for different elementary current inputs. Then, more complex current inputs are used to examine other capabilities of the active isolator.

The dynamic stiffness response of the active hydraulic bushing is a determined in Chapter 8. The mathematical model, derived in Chapter 7, is used again to find the dynamic stiffness transfer function. It is shown that the active isolator is successful at controlling the damping at the peaks of the dynamic stiffness response, and the shifting of the notch frequencies. The active hydraulic bushing is also able to create any dynamic stiffness response at specified frequencies by applying the appropriate transfer function to the input current. This feature renders the active bushing suitable for more general vibration applications than the engine isolator.

Some of the difficulties and concerns that caused delay in the project at some stages are listed in Chapter 9. The air bubbles entrapment and MR-rubber compatibility caused the majority of the problems.

The next phase of this project is commercialization of the semi-active and active hydraulic bushings. The semi-active and the active bushing parameters should be fine tuned through numerical and experimental studies. The design, fabrication, and performance of the final prototype should be improved to closely meet the required specifications. The active chamber and the MR valve should be miniaturized and placed inside the bushing assembly.

In the future a microprocessor and/or engine computer based control system should be designed and fabricated for the final practical application. Low-cost and practical sensors must be selected to provide feedback to the control system. A sensor minimization study should be conducted to ensure if available information such as engine throttle may provide enough information to eliminate the need for sensors altogether.

The prototypes should be tested for all standard tests (including quality assurance) required approving a commercial bushing. The dynamic test should be performed on an MTS 831 high frequency elastomer dynamic characterization test machine from 0 to 400Hz, 0 to 2mm displacement peak to peak with the preload from 700-2000N. Single axis durability testing should be performed on an MTS 810 elastomer durability test machine at 3Hz, rated preload, +/-3g, and for 1 million cycles. Triple axis simulation (RPC) testing should also be developed on an MTS 3-channel durability test system, based on road load data acquisition (RLDA) files from the target vehicle platform. Bushing target will be three parts tested to three lives, or six parts tested to one life. One life is typically approximately 100-130 hours of real-time testing (based on RLDA files that have been edited to remove non-damaging content).

Reference:

Ahmadian, M., & Ahn, Y.K. 1999. "Performance Analysis of Magneto-Rheological Mounts," *Journal of Intelligent Material Systems and Structures, 10, 248-256.*

Ahn, Y.K., Ahmadian, M., & Morishita, S. 1999, "On the Design and Development of a Magneto-Rheological Mount," *Vehicle System Dynamics, 32, 199-216.*

Anderson, E. H., & Houghton, B., 2001, "Active Vibration Isolation Workstation," *SPIE smart structure and materials, Paper 4332-23.*

Andrews, F. J. , 2002, " A Primer on Vibration Isolation," *Sound and Vibration, 36(1), 42-46.*

Ashley, S., 2004, "Firing on Half-Cylinders," *Scientific American, v 291, n 6, pp. 20-22.*

Baumal, A., McPhee, J., Calamai, P., 1998, "Application of Genetic Algorithms to the Optimization of an Active Vehicle Suspension Design," *Computer Methods in Applied Mechanics and Engineering, 163:87-94.*

Baudendistel, T.A., Tewani, S.G., Shores, J.M., Long, M.W., Longhouse, R.E., Namuduri, C.S., & Alexandridis, A.A. 2002, "Hydraulic Mount With Magnetorheological Fluid," *US Patent 0171186.*

Beranek, L. L., Ver, I. L., 1992, "Noise & Vibration Control Handbook," *John Wiley, New York.*

Bernuchon, M., 1984, "A New Generation of Engine Mounts," *SAE Paper #840259.*

Borcea, L., Bruno, O., 2001, "On the Magneto-Elastic Properties of Elastomer-Ferromagnet composites," *Journal of the Mechanics and Physics of Solids, vol. 49, n12, pp. 2877-299*

Calcaterra, P. C. and Schubert, D. W., "Active Vibration Isolation of Human Subjects from Severe Dynamic Enviorments," *ASME Paper 69-VIBR-65.*

Carlson, D.J., Chrzan, M.J., & James, F.O. 1994, "Magnetorheological Fluid Devices," *US Patent 5284330.*

Cavanaugh, R. D., 1996, "Air Suspension And Servo-Controlled Isolation Systems," *Shock and Vibration Handbook, (C. M. Harris and C.E Crede, editors), Vol 2, Ch 33, McGraw Hill.*

Chalasani, R.M., 1986 "Ride Performance Potential of Active Suspension System. Part I: Simplified Analysis Based on Quarter Car Models," *ASME Symposium on Simulation of Ground Vehicle and Transport Systems, ASME, Anaheim, CA.*

Choi, S.B., Song, H.J., Lee, H.H., Lim, S.C., & Kim, H.J., 2003, "Vibration Control of a Passenger Vehicle Featuring Magnetorheological Engine Mounts," *International Journal of Vehicle Design, 33(1-3), 2-16.*

Choi, S.B., Lee, H.H., Song, H.J., & Park, J.-S., 2002, "Vibration Control of a Passenger Car Using MR Engine Mounts," *Smart Structures and Material, 4701, 1-8.*

Clark, M. , 1985, "Hydraulic Engine Mount Isolation," *SAE Paper #851650.*

Colgate, J. E., Chang, C. T., Chiou, Y. C., Liu, W. K., Keer, L. M., 1995, "Modeling of a Hydraulic Engine Mount Focusing on Response to Sinusoidal and Composite Excitations," *Journal of Sound and Vibration 184, 503-528.*

Corcoran, P. E., Ticks, G. H., 1984, "Hydraulic Engine Mount Characteristics," *SAE Paper #840407.*

Crede, C. E., 1951, "Vibration and Shock Isolation," *John Wiley, New York.*

Crede, C. E., Cavanaugh, R. D., 1985, "Feasibility Study of an Active Vibration Isolator for a Helicopter Rotor," *WADC 58-183.*

Daley, S., Johnson, F.A., Pearson J.P., Dixon, R., 2004, "Active Vibration Control for Marine Applications," *IFAC Journal Control Engineering Practice (4), pp. 465–474.*

Daley, S., Johnson, F. A., 2004, "The "Smart Spring" Mounting System: A New Active Control Approach for Isolating Marine Machinery Vibration," *Proceedings of IFAC conference on control applications in marine systems (pp. 503–508). Ancona, Italy.*

Daley, S., 1998, "Algorithm Architecture for Sound and Vibration Control," *Institution of Measurement and Control Mini-symposium at UKACC Conference CONTROL'98, Swansea, Septembe.*

Daley, S., Hatonen, J., Owens, D.H., 2006, "Active Vibration Isolation in a "Smart Spring" Mount," *Control Engineering Practice, v 14, n 9, p 991-7*

Darbyshire , E.P., Kerry, C.J., 1997, "A Multi-Processor Computer Architecture for Active Control," *Control Engineering Practice 5 (10), pp. 1429–1434.*

Davis, L. C., 1999, "Model of Magnetorheological Elastomers," *Journal of Applied Physics, 85(6):3348-3351.*

Duclos, T. G., 1987, "An Externally Tuneable Hydraulic Mount Which Uses Electrorheological Fluid," *SAE paper # 870963*

Dyke, S. J., Spencer, Jr B. F., Sain, M. K., Carlson J. D., 1998, "An Experimental Study of MR Dampers for Seismic Protection," *Smart Materials and Structures,7:693-703.*

Dyke, S. J., Spencer, Jr. B. F., Sain, M. K., Carlson, J. D., 1996, " Modeling and Control of Magnetorheological Dampers for Seismic Response Reduction," *Smart Materials and Structures, 5:565-575.*

Esmailzadeh, E., 1978, "Optimization of Pneumatic Vibration Isolation System for Vehicle Suspension," *Transaction of the ASME Journal of Mechanical design 100, 500-506*

Flower, W. C., 1985, "Understanding Hydraulic Mounts for Improved Vehicle Noise, Vibration and Ride Qualities," *SAE Paper #850975.*

Geck, P. E., Patton, R. D., 1984, "Front Wheel Drive Engine Mount Optimization" *SAE Paper #840736.*

Gee-Clough, D., Walter, R. A., 1968, "An Improved Self Damped Pneumatic Isolator," *Journal of Sound and Vibration 8,364-376.*

Geisberger, A., 2000, "Hydraulic Engine Mount Modeling, Parameter Identification and Experimental Validation," *MASc. Thesis, University of Waterloo.*

Geisberger, A., Khajepour, A., Golnaraghi, F., 2002, "Non-linear Modelling of Hydraulic Mounts: Theory and Experiment," *Journal of Sound and Vibration, 249(2), 371-397.*

Ginder, M. E. Nichols, L. D., Elie, J. D., S. M. Clark, 2000, "Controllable-Stiffness Components Based on Magnetorheological Elastomers," *Smart Materials 2000: Smart Structures and integrated systems, Proceedings of SPIE 3985, pp.418-425.*

Golnaraghi, M.F., 1991, "Regulation of Flexible Structure Via Nonlinear coupling," *Dynamic and Control 1, 405-428.*

Golnaraghi, M.F., & Jazar, N. G., 2001, "Development and Analysis of a Simplified Nonlinear Model of a Hydraulic Engine Mount," *Journal of Vibration and Control, 7(4), 495-526.*

Gorodkin, S., Lukianovich, A., & Kordonski, W. 1998, "Magnetorheological Throttle Valve in Passive Damping Systems," *Journal of Intelligent Material Systems and Structures, 9.*

Hall, B. B., Tang, J. S., 1990, "Analysis of Active and Semi-active Vehicle Suspensions Fitted with a Pneumatic Self Energizing Level Device," *Journal of Automobile Engineering 204, 161-168.*

Hardie, C., Tait, H., Craig, S., Chase, J.G., Smith, B.W., & Harris, G. (2002). "Automated Tuning of an Engine Management Unit for an Automotive Engine," Journal *of Automobile Engineering, 216(10), 841-849.*

Hartono, S., Harley H., 1994, "Electro-Mechanical Analysis of an Active Engine Mount Incorporating Piezoelectric Stack Actuators," ASME, Aerospace Division (Publication) AD, v 45, Adaptive Structures and Composite Materials: Analysis and Application, 1994, p 211-218

Harpavat, G., 1974, "Magnetostatic Forces on a Chain of Spherical Beads in a Uniform Magnetic Field" IEEE Trans. Magn. 10, 919–22

Hillis, A.J., Harrison, A.J.L., Stoten, D.P., 2005, "A Comparison of Two Adaptive Algorithms for the Control of Active Engine Mounts" *Journal of Sound and Vibration, v 286, n 1-2, p 37-54*

Hong, S.R., Choi, S.B., Jung, W.J., Ham, I.B., Kim, D.K., 2001, "Vibration of an ER Mount Subjected to High Static Loads," *Journal of Sound and Vibration, 242(4), 740-748.*

Inman, D. J., 2001, "Engineering Vibration," *Princeton Hall, New Jersey*

Jacobs, S. D., Kordonski, W. I., Prokhorov, I. V., Golini, D., Gorodkin, G. R., and Strafford, T. D., 1998. "Magnetorheological Fluid Composition." U.S. Patent 5,804,095.

Jackson, M.D., Jones, P., 1976, "Deactivating Compressor-Engine Cylinders Saves Fuel," *Oil and Gas Journal, 74(31), pp. 130-133.*

Johnson, F.A., Swinbanks, M.A., 1996, "Electromagnetic Control of Machinery Rafts," *Journal of Defence Science 1 (4), pp. 493–497.*

Jolly, M. R., Bender J. W., Carlson J. D., 1999, "Properties and Application of Commercial Magnetorheological Fluids," *Journal of Intelligent Material Systems and Structures, 10: 5-13.*

Jolly, M. R., Carlson, J. D., Munoz, B.C., 1996, "A Model of the Behavior of Magnetorheological materials," *Smart Materials and Structures, 7(6):613-622.*

Kamper, J. D., Ayre, R. S., 1971, “Optimum Damping and Stiffness in a Nonlinear Four-Degree-of-Freedom System Subject to a Shock Load,” *J.Appl.Mech. 38, pp.135-142.*

Karnopp, D. C., Corsby, M, J., 1974, “System for Controlling the Transmission of Energy Between Spaced Members,” *U.S. Patent No. 3,807,678.*

Kim, G., Singh, R. ,1993, “Nonlinear Analysis of Automotive Hydraulic Engine Mount,” *Journal of Dynamic Systems, Measurement and Control, Transactions of the ASME, 115(3), 482-487.*

Kosuke, S., Tatsuhide, S., 2006, “Development of Simulation Model for Active Control Engine Mount,” Review of Automotive Engineering, v 27, n 1, p 155-157.

Kuzhir, P., Bossis, G., Bashtovoi, V. 2003, “Effect of the Orientation of the Magnetic Field on the Flow of a Magnetorheological Fluid. I. Plane channel,” *Journal of Rheology, 47(6), 1373-1384.*

Kuzhir, P., Bossis, G., Bashtovoi, V., & Volkova, O. 2003, “Effect of the orientation of the magnetic field on the flow of magnetorheological fluid. II. Cylindrical channel,” *Journal of Rheology, 47(6), 1385-1398*

Leatherwood, J. D., Dixon, G. V., 1968, "Active Vibration Isolation for Flexible Payloads,” *IES Proceedings 407-413.*

Lin, Y., Luo, W., & Zhang, Y.M., 1990, “New Method for the Optimization of a Vibration Isolation System,” *Journal of Vibration, Acoustics, Stress, and Reliability in Design, 112,(3), 413-416.*

Little, E., Kashani, R., 1995, “Adaptive-Passive and Active Hydraulic Engine Mounts, Advanced Automotive Technologies, “ *ASME, DSC-Vol.56/DE-Vol.86, pp.135-140.*

Matsuoka, H., Mikasa, T., Nemoto, H., Gehm, R. (Ed.) 2004, "Bringing Down the Noise." *Automotive Engineering International, 112(9), 83-87.*

Makhult, M., 1977, "Machine Support Design Based on Vibration Calculus," *Akademia Kiado, Budapest.*

McDonald, A. M., Elliott, S. J., Stokes, M. A., 1991, "Active Noise and Vibration Control Within the Automobile," *Proceedings of the international symposium on active control of sound and vibration (pp. 147–156). Acoustical Society of Japan.*

Muller, M., Weltin, U., Law, D., Roberts, M. M., Siebler, T. W., 1994, "Engine Mounts and NVH," *Automotive Engineering, 102(7), 19-23.*

Nakaji, Y., Satoh, S., Kimura, T., Hamabe, T., Akatsu, Y., Kawazoe, H., 1999, "Development of an Active Control Engine Mount System," *Vehicle Dynamic Systems, 32, pp.185-198.*

Nakhaie Jazar, G., Golnaraghi, M.F., 2002, "Nonlinear Modeling, Experimental Verification, and Theoretical Analysis of a Hydraulic Engine Mount*," Journal of Vibration and Control, 8: 87-116.*.

Nakhaie Jazar, G., Narimani, A., Golnaraghi, M.F., Swanson, D.A., 2003, "Practical Frequency and Time Optimal Design of Passive Linear Vibration Isolation Mounts," *Vehicle System Dynamics, 39(6): 437-466.*

Narimani, A., Golnaraghi, M.F. and Nakhaei Jazar, G., 2004, "Sensitivity Analysis of the Frequency Response of a Piecewise Linear System in a Frequency Island," *Journal of Vibration and Control, 10, pp.175-198*

Narimani, A., 2004, "Development of Linear and Nonlinear Isolation Techniques for passive and Semi-Active Application" *(Ph.D. Dissertation). Waterloo, ON, CA: University of Waterloo.*

Nayfeh, T.A., Emaci, E., & Vakakis, A.F. ,1997, " Application of Nonlinear Localization to the Optimization of a Vibration Isolation System," *AIAA Journal, 35(8), 1378-1386.*

Oueini, S. , Chin, C.M, Nayfeh, A.H., 1999, "Dynamics of a Cubic Nonlinear Vibration Absorber," *Nonlinear Dynamics, 20: 283-295.*

Peel, D. J., Stanway, R., and Bullough, W. A., 1996, "Dynamic Modelling of an ER Vibration Damper for Vehicle Suspension Applications," *Journal of Smart Mater. Struct., no. 5, 591-606.*

Pintado, P. and Benitez, F. G., 1990, "Optimization of Vehicle Suspension I: Time domain," *Vehicle System Dynamics, 19:273-288.*

Rabinow, J., 1948, "The Magnetic Fluid Clutch*." AIEE Transactions, Vol. 67, pp. 1308–1315.*

Rao, S. S., 2004, "Mechanical vibrations (4th ed.)." *Upper Saddle River, N.J.: Pearson Prentice Hall.*

Royston, T.J., Singh, R., 1996, "Optimization of Passive and Active Nonlinear Vibration Mounting Systems Based on Vibratory Power Transmission," *Journal of Sound and Vibration, 194(3), pp. 295-316*

Sakamoto, K., Sakai, T., 2006, "Development of Simulation Model for Active Control Engine Mount," *Automotive Engineering, v 27, n 1, p 155-157*

Serrand, M., Elliott, S. J., 2000, "Multi Channel Feedback Control for the Isolation of Base-Excited Vibration," *Journal of Sound and Vibration 234,681-704.*

Shiga, Y. Fujimoto, M. Hirose, Tokai Hei, 1993, *Japanese Patent 5-25315, Feb. 2, 1993.*

Shtarkmen, E.M., 1993, "Vehicle Engine Mount," *US Patent 5176368.*

Shoureshi, R., Graf, P. L., Houston, T. L., 1986, "Adaptive Hydraulic Engine Mounts," *SAE Paper # 860549*

Schubert, D. W., Ruzicka, J. E., 1969, "Theoretical and Experimental Investigation of Electro Hydraulic Isolation Systems," *Journal of Engineering of Industry, trans. ASME 91,981-990*

Shameli , E. , Khamesee, M.B., Huissoon, J.P, 2006 ,"Nonlinear Controller Design for a Magnetic Levitation Device," Proceedings of ASME/JSME Joint Conference on Micromechatronics for Information and Precision Equipment (MIPE 2006)

Singh, R., Kim, G., Ravindra, P.V., 1992, "Linear Analysis of Automotive Hydro-Mechanical Mount with Emphasis on Decouple Characteristics," *Journal of Sound and Vibrations, 158(2): 219-243.*

Smith, R.E., and Lum, E. L. S., 1968," Linear Optimal Theory Applied to Active Structural Bending Control," *Journal of Aircraft, AIAA 5,475-479.*

Smollen, L. E., Marshall, P., Gabel, R., 1962, "A Servo Controlled Rotor Vibration Isolation System for Reduction of Helicopter Vibration," *IAS Paper No.62-34, Institute of Aerospace Science.*

Spasojevic, D., Irvine, T. F., Afgan, N., 1974, "The Effect of a Magnetic Field on the Rheodynamic Behaviour of Ferromagnetic Suspensions," *Int. J. Multiphase Flow ,1:607-622*

Stein, G. J., 1995, "Result of Investigation of an Electro Pneumatic Active Vibration Control System for a Driver's Seat," *Proc Instn Mech Engrs 209, 227-234.*

Stothers, I., 2002, "Active Control in Aircraft," *IMechE mini-symposium at UKACC conference CONTROL 2002, Sheffield, 10–12.*

Sun, L., 2002, "Optimum Design of 'Road-Friendly' Vehicle Suspension Systems Subjected to Rough Pavement Surface," *Applied Mathematical Modelling, 26: 635-652.*

Sumali, H., Cudeny, H.H., 1994, "An Active Engine Mount with a Piezoelectric Stacked Actuator, American Institute of Aeronautics and Astronautics," *AIAA, 1466-CP, pp. 1233-1241,*

Sumali, H., Cudney, H. H., 1994, "Electro-Mechanical Analysis of an Active Engine Mount Incorporating Piezoelectric Stack Actuators" *ASME, Aerospace Division (Publication) AD, v 45, Adaptive Structures and Composite Materials: Analysis and Application, p 211-21.*

Swanson, D. A., Miller, L. R., 1993, "Design and Effectiveness Evaluation of an Active Vibration Isolation System for a Commercial Jet Aircraft," *AIAA Paper No. 93-1145. Presented at the AIAA aerospace design conference. Irvine, California.*

Tamboli, J. A., Joshi, S. G., 1999, "Optimal Design of a Passive Suspension System of a Vehicle Subjected to Actual Random Road Excitations," *Journal of Sound and Vibration, 219(2):193-205.*

Tuer, K. L., Golnaraghi, M. F., Wang, D., 1994, "Development of a Generalized Active Vibration Suspension Strategy for a Cantilever Beam Using Internal Resonance," *Nonlinear Dynamics 5, 131-151.*

Ushijima, T., Takano, K. and Kojima, H., 1988, "High Performance Hybrid Mount for Improving Vehicle Noise and Vibration," *SAE paper #880073*

Vakakis, A.F., McFarland, D. M., Bergman, L., Manevitch, L., Gendelman, O., 2003, "Passive Vibration Control Through Nonlinear Energy Pumping," *Proceedings of the ASME Design Engineering Technical Conference (pp. 1883-1888), 5. Chicago, IL: American Society of Mechanical Engineers.*

Williams, E.W., Rigby, S.G., Sproston, J.L., Stanway, R., 1993, "Electrorheological fluids applied to an automotive engine mount," *Journal of Non-Newtonian Fluid Mechanics, 47, 221-238.*

Winberg, M., Johansson, J., Lago, T. 2000, "Control approaches for active noise and vibration control in a Naval application" *Proceedings seventh international congress on sound and vibration. Garmisch-Partenkirchen, Germany*.

Winslow, W. M., 1949, "Induced Fibration of Suspensions." *Journal of Applied Physics, Vol. 20, pp. 1137–1140.*

Yoshiharu, N., Shigeki, S., Takeshi, K., Tsutomu, H., Akatsu, Yousuke, A., Hiroshi, K, 1999, "Development of an Active Control engine Mount system," *Vehicle System Dynamics, v 32, n 2, Aug, 1999, p 185-198.*

Yu, Y., Peelamedu, S. M., Naganathan, N. G., Dukkipati R.V., 2001, "Automotive Vehicle Engine Mounting Systems: A Survey" *Trans. ASME, Journal of Dynamic System, Measurement, and Control, 123, 186-194.*

Yu, Y., Naganathan, N. G., and Dukkipati R.V., 2001, "A Literature Review of Automotive Vehicle Engine Mounting System" *Journal of Mechanism and Machine Theory, 36, 123-142.*